A Framework for Comparing Geomechanical Models of InSAR-measured Surface Deformation
by

Neil Edward James de Laplante
B.A.Sc., Geological Engineering (2008)
University of Waterloo

Submitted the the Department of Earth, Atmospheric and Planetary Sciences
in Partial Fulfillment of the Requirements for the Degree of
Master of Science in Geophysics

at the

Massachusetts Institute of Technology

September 2011

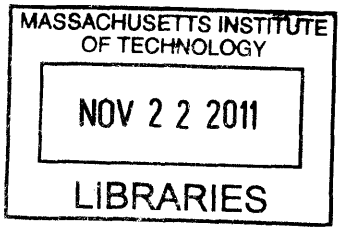

ARCHIVES

Signature of Author .
Department of Earth, Atmospheric and Planetary Sciences
July 29, 2011

Certified by .....
Bradford H. Hager
Cecil and Ida Green Professor of Earth Sciences
Thesis Supervisor

Accepted by .....
Maria T. Zuber
E.A. Griswold Professor of Geophysics
Head of the Department

A Framework for Comparing Geomechanical Models of InSAR-measured Surface Deformation

by

Neil Edward James de Laplante

Submitted the the Department of Earth, Atmospheric and Planetary Sciences
in Partial Fulfillment of the Requirements for the Degree of
Master of Science in Geophysics

ABSTRACT

High-quality Interferometric Synthetic Aperture Radar (InSAR) surface deformation data for field sites around the world has become widely available over the past decade. Geomechanical models based on InSAR data occur frequently in the literature but few methods of systematically optimizing or comparing them are presented. This work discusses parameterization errors for simplified models of strike-slip, normal, thrust and reservoir-style faulting with the aim of identifying tests or characteristics that can differentiate between error types uniquely. Fault dip errors, slip errors and depth errors are modelled using a simple homogeneous elastic half-space earth model. Simple difference maps prove to be a powerful tool for identifying error types and parameter sensitivity, with gradient maps and gradient difference maps useful for distinguishing between similar cases. The fault dip proves to be more indicative of error resolving capability than the faulting regime; errors on intermediately dipping faults are very difficult to differentiate. More detailed modelling of compound errors, complex geomechanical properties and noisy data is proposed. The use of the tests as the starting point for an artificially intelligent modelling package is briefly discussed.

ACKNOWLEDGEMENTS

There are many people to whom I am grateful for the important roles, large and small, that they have played in my road to this point. Rather than attempt an exhaustive listing and risk offending through negligence, I trust that any reader knows their value to my journey and will accept my sincerest thanks.

Except for Kate. You're the best, dear.

Contents

List of Figures

List of Tables

Chapter 1

Introduction

In recent years there has been an explosion of high-precision geodetic surface deformation monitoring data from Global Positioning System (GPS) stations and Synthetic Aperture Radar (SAR) satellites. The increasing ease of access to the data and its increasingly broad coverage of sites of diverse geological and geophysical interest has provoked a concordant boom in geodetic modelling of surface deformation. Indeed, certain sites are the subject of multiple competing models from different research groups using completely different methodologies (eg. the In-Salah CO_2 sequestration project in Algeria; Rutqvist, 2009 [13], Vasco, 2010 [23], Morris, 2011 [7]).

Despite the monotonically increasing number of competing models, few concerted attempts have been made to compare and evaluate them objectively against the ground-truth observed deformation. Optimizing a single model is a difficult process subject to many discretionary judgements

including the choice of parameter space, the computational techniques employed and the modeller's biases regarding the site's deformation history. The diversity of models is both expected and vital because the problem is inherently non-unique and remains relatively poorly constrained despite the new data.

The goal of this research is to break the geodetic modelling problem into its smallest component units and establish a set of criteria for distinguishing different types of parameter errors. A suite of simple models is presented covering four major fault types: strike-slip, normal, thrust and reservoir-style faulting. The effect of known errors in the fault depth, dip and slip distance on the resulting surface deformation is tested for each fault type. The goal of these tests is to identify ways that parameter variations in models of the same site can be precisely compared. However, this study stops short of formulating any formal ranking or optimization criteria.

A simple homogeneous elastic half-space earth model is used so that the Okada (1985 [8]) analytical solutions for deformation apply. The initial models were generated using the Coulomb 3.2 software package of the United States Geological Survey (USGS) (Toda, 2010 [22]). Difference maps, deformation histograms and gradient maps are used to distinguish between the error types based solely on their computed deformation patterns.

The methodology for the models and the comparison tests are described in detail in Chapter 2. The resulting tests, discussed in Chapter 3

could be used for optimization of existing models, to compare rival models of the same site or as the basis for an artificially intelligent modelling package. These prospective applications and some of the difficulties that will be faced using the tests with real data and more complex models are discussed in Chapter 4. The MatLab code used to process the Coulomb 3.2 results and generate all of the figures is included in an appendix.

Chapter 2

Methodology

The work presented here has two purposes: to develop a suite of surface displacement models for different parameterization errors and geological scenarios and to investigate simple tests that can identify different types of errors in the model parameter space. This discussion of the methodology is divided into two parts covering the geodetic models and the statistical testing techniques.

2.1 Geodetic Modelling

The results presented in Section 3 are simple geomechanical models of the surface deformation that results from earthquakes. A simple homogeneous elastic half-space earth model has been used in combination with the analytic Okada (1985 [8]) solutions for surface deformation and the

Coulomb 3.2 software package (Toda, 2010 [22]) to test the impact of different types of parameterization errors as compared to the reference model. In a case with real data, the reference model would be replaced by the InSAR interferogram of the field site. The following sections discuss the geodetic models in more detail.

2.1.1 Coulomb 3.2 Modelling Software

Coulomb 3.2 is a MatLab software package created at the USGS and Woods Hole Oceanographic Institute (Lin and Stein, 2004, [6]; Toda et. al, 2005, [20]). Coulomb 3.2 has a well-developed graphical user interface, but all of the source code is accessible to the user. Its primary purpose is to calculate static stress transfers due to large earthquakes according to an implementation of the Coulomb Failure Criterion utilizing source and receiver faults. Coulomb 3.2 is very strong graphically and the majority of the figures in the results section were created either in Coulomb 3.2, by modifying the Coulomb 3.2 source code, or by reprocessing the raw Coulomb 3.2 output.

Coulomb 3.2 can calculate "static displacements, strains, and stresses at any depth caused by fault slip, magmatic intrusion or dike expansion/contraction", as well as, "static displacements (on a surface or at GPS stations), strains, and stresses caused by fault slip, magmatic intrusion or dike expansion." (Toda, 2010 [22]). The USGS makes Coulomb 3.2 freely available for non-commercial research and it remains under active

development. This project does not use the stress transfer modelling capabilities of Coulomb 3.2, but makes extensive use of its 3-D implementation of the Okada 1985 solutions [8] for displacements in a half-space.

The package and method's weakness, its inability to process heterogeneous earth models, is minimized for this project because Coulomb 3.2 is used to generate model suites to compare to each other rather than in an attempt to make the most accurate possible model of a given reservoir or earthquake. Self-consistency in the model suite is more important because the models are theoretical cases only. The goal of the work presented in this document is not to produce the best model possible but instead to develop methods for ranking and optimizing different models of the same site.

Coulomb 3.2 calculates three dimensional surface deformations for all models. Since processed InSAR data is usually only one dimensional, the post-processing routines in this study simply ignore the X and Y displacement information. When using real InSAR data the picture is more complicated since the one dimensional line-of-sight InSAR deformation observed includes vertical and lateral, predominantly easterly, components (see Section 2.1.3). Coulomb 3.2 can also calculate three dimensional GPS deformation vectors. This capability has not been used in this study but could be a useful extension for future modelling.

Surface deformation models produced in Coulomb 3.2 are particularly oversimplified in a reservoir scenario, where fluid flow is more important

and the heterogeneous coupled hydromechanical capabilities of Finite Element Methods (FEM) packages excel. However, the limitations of the Coulomb models for reservoirs is perhaps a blessing in disguise for this project because it minimizes the risks posed by overly aggressive parameterization and discretization.

2.1.2 The Okada Solutions for Surface Displacement

Dislocation theory, a technique for calculating the stresses due to internal displacements in a medium, was introduced to seismology by Steketee (1958, [19]) and Rongved and Frasier (1958, [12]). The theory was first formulated by the crystallographer Volterra (1905) to explain the stresses resulting from the termination of a plane of atoms in the middle of a crystal structure or from a helical crystallographic disruption. Frank and Read coined the term dislocation theory in 1950 [2] while proposing a model for dislocations under shear stress.

Many contributions to the calculation of surface deformations using dislocations for special cases and source types followed over the next 25 years, but gaps and computational challenges were plentiful. Okada (1985 [8]) published a seminal paper which corrected errors, eliminated singularities and reformulated all of the prior work for point sources and compressive faulting into closed form analytical solutions for displacement, strain and tilt. At the time, accurate measurements of surface displacement were very limited so the homogeneous earth assumption made by Okada

was not troubling because the models were still more precise than the geodetic data.

Further to correcting and expanding prior work on point sources, Okada developed new solutions for tensile faulting and finite rectangular sources. These solutions and a subsequent analytic formulation for internal deformation (Okada, 1992 [9]) are two of the most widely-cited works in geophysics. The equations Okada presents in these two papers form the basis of the Coulomb 3.2 software; in fact, Okada's own MatLab code forms the core of Coulomb 3.2. The work presented here uses only a small part of the power of Okada's solutions to solve for the vertical surface displacement.

2.1.3 Interferometric Synthetic Aperture Radar (InSAR)

Interferometric Synthetic Aperture Radar (InSAR) is a satellite-based technology for measuring surface deformation. A low Earth-orbiting Synthetic Aperture Radar (SAR) satellite in a polar orbit bounces radar waves off of the surface and records the amplitude, phase and time of the reflected signal. Since the satellites utilize near-polar orbits they have much lower sensitivity to deformation in their direction of travel (north-south) than to vertical or east-west trending deformation. The line-of-sight deformation that interferograms show is a combination of vertical and lateral (primarily east-west) deformation. The line-of-sight deformation can

only be decomposed into vector components if measurements over the site have been obtained from two or more look angles.

Calculating surface displacement from SAR data requires high-accuracy repeated orbits over the same location to measure phase shifts to determine the displacement by interferometry. Interferograms are constructed from two SAR images by subtracting the phase of the images pixel-by-pixel. Combining SAR images from different platforms into interferograms is not possible because of the orbital differences between the satellites, but processed interferograms from different platforms can be compared. Most existing monitoring or tectonics projects focus on data from a single platform (Rodriguez, 1992, [11]).

There are a number of deployed and functional space-borne radar platforms including the Canadian Space Agency's RADARSAT-1 and RADARSAT-2, the European Space Agency's Envisat and the Japanese Space Agency's JERS-1 satellites. These platforms employ C-Band sensors with wavelengths from 40-80mm, except for the L-band (150-300mm) JERS-1 mission. Future missions are planned to expand the InSAR data suite into the X (25-40mm) and L (150-300mm) bands to expand the sensitivity and resolution available from the SAR satellite suite.

Compared to GPS data, InSAR deformation measurements are less accurate, centimetre-scale rather than millimetre-scale, and are discrete in time. The lowest repeat time possible for InSAR data from a single platform at present is approximately one month, so coseismic observations

are impossible. The two technologies work well in tandem to establish a deformation data set that is continuous and well-resolved in both space and time(Segall 2010, [15]).

A major advantage of GPS data is that it is three dimensional, with higher accuracy laterally than vertically. Deriving three-dimensional deformation from interferograms is an active area of research (eg. Gray, 2011 [5]). The model evaluation techniques discussed later will scale easily to the three dimensional case but are presented only in terms of vertical (z) deformation for simplicity, ignoring that real InSAR data measures line-of-sight deformation instead of vertical. To compare models and real InSAR data the modelled vector deformation fields must be converted into line-of-sight changes using the basic orbital parameters of the SAR satellite in question (eg. Vasco, 2010 [23], Rutqvist, 2009 [13]).

2.2 Statistical Tests

A primary goal of this project is to identify simple statistical checks that assess the relative value of different geologic or geophysical models of the same InSAR-measured surface deformation. Model comparisons in most published literature are very qualitative and the geodetic modelling community stands to benefit from a coherent way to rank its results given the inherent non-uniqueness of solutions at each site.

The ensemble of tests proposed could also serve as the basis for an

automated model optimizer at a later date. The increasing availability of InSAR data and rise of CO_2 sequestration projects that require verification combine to make model evaluation a particularly timely topic. The tests discussed here and the unique deformation patterns identified in Chapter 3 should also apply to much more complicated models. This discussion's intent is to identify baseline parameter changes in geodetic response through a broadly adaptable reductionist approach.

2.2.1 Difference Maps

Difference maps are the simplest first order error evaluation tool. Difference maps are generated by subtracting the modelled deformation from the interferogram, i.e.

$$Diff = InSAR - Model$$

Difference maps are only occasionally published (eg. Wicks, 1998 [24]), but are a very useful tool for identifying errors. The difference maps presented later on are calculated using element-wise subtraction in MatLab.

2.2.2 Gradient Maps

Gradient maps show the first spatial derivative of a model's surface deformation. The plots presented in Chapter 3 use arrows to indicate the gradient direction at a point, underlain by contours of the gradient magnitude. The gradient is calculated created using MatLab's *gradient()*

function, which returns the numerical gradients dF/dx and dF/dy in separate matrices of the same size as the input matrix. The gradient maps reveal greater detail in the deformation structure and are very useful for distinguishing between parameter errors with similar surface expressions. Gradient difference plots are generated by subtracting the dF/dx and dF/dy matrices of the two models being compared prior to calculating the directions and magnitudes for the plot.

Chapter 3

Results and Interpretation

Four important types of faulting are considered in this section: Strike-slip, Normal, Thrust and Reservoir-type (compound). There are six model parameters potentially subject to error and optimization for each category: strike, dip, fault depth, fault location, fault dimension and slip. The following four sections first introduce the surface deformation caused by a reference model of known geologic provenance. The reference model is treated as a black box "interferogram", and the effect of systematically varying one of the modelling parameters is presented in each sub-section. The models are tested to identify characteristics indicative of specific error types as uniquely as possible.

The following sections assume that the type of faulting and fault dimensions will always be known a priori by a modeller, whether human or artificial intelligence-driven, since earthquake moment tensors and basic

geologic observations are normally available for faults that are subject to scrutiny by InSAR. For simplicity the models use constant slip over the fault area, but real earthquakes and most detailed fault models have variable slip. This simplification should only change the deformation patterns that a modelled earthquake generates and should not affect the comparison between models or to the "interferogram" reference models. All of the models are constructed on square grids at reservoir scale with a 100m grid cell size unless otherwise noted for simplicity and comparison purposes. However, the Okada solutions are non-dimensional and the solutions scale arbitrarily.

Images of the same type in the same section use the colour bar of the reference image of that type, eg. all raw z-displacement plots use the "interferogram" colour bar, but all gradient plots use the colour bar for the gradient of the interferogram. The models are relatively simple, but the error identification techniques described should be effective on complex models because Okada-based deformation models are relatively superposable. Complex models are made by adding many simple components and can be decomposed into end-member faulting components for calculation and evaluation.

3.1 Strike-Slip Faulting

Strike-slip faulting is very common in tectonic settings, particularly at transverse plate boundaries. The best-known examples of strike-slip faults are the San Andreas Fault in California (eg. Segall, 1985, [14]) and the Anatolian Fault in Turkey (eg. Stein et al., 1997, [18], Delouis, 2002, [1]). The ground deformation patterns seen after strike-slip earthquakes were thoroughly discussed by Stein et al., 1994 [17]. This paper also introduced the Coulomb 1.0 software package whose latest version (3.2) was used to generate all of the models presented in this chapter.

Characteristic surface deformation for strike-slip faults is upwards beyond the end of the fault in the direction of slip on both sides, and downwards in the direction that the observer's side has moved away from. For example, in a North-South striking, right-lateral fault, lobes of positive surface deformation would be seen in the Northwest and Southeast. Strike slip faulting is often complex and multi-segmented, with local fault conditions influencing the extent of rupture and surface deformation.

The reference model consists of a two-segment, vertical strike-slip fault, with the southern segment trending due North-South and the northern segment striking at N20E. Cases 1 and 2 show the deformation due to faults shallower and deeper than the reference model. Cases 3 and 3a see the faults dipping slightly from the vertical while Cases 4 and 5 see too much and too little slip. The effects of displacing the fault in the X and

Y directions are considered in cases 6 and 7.

The fault parameters for all of the cases are summarized in Table 3.1. Coulomb 3.2 has a singularity for faults dipping at 90 degrees (Toda, 2010, [22]) so dips of 89.9 degrees are used to approximate vertical faults. The fault model for the reference case and the calculation grid (100m spacing) are shown in Figure 3.1. All subsequent models in this section were created by modifying single parameters in the reference model, which is treated as if it were an interferogram collected over a field site. The basic model statistics for each case are summarized in Table 3.2.

Table 3.1: Strike-slip Fault Model Parameters

Case	X start (km)	Y start (km)	X end (km)	Y end (km)	Right-lat Slip (m)	Reverse Slip (m)	Dip (deg)	Fault Top (km)	Fault Bottom (km)
ref	7.5	5.5	7.5	7.5	0.05	0	89.9	1.5	3.0
ref	7.5	7.5	8.25	9.5	0.03	0.01	89.9	1.5	3.0
1	7.5	5.5	7.5	7.5	0.05	0	89.9	0.5	2.0
1	7.5	7.5	8.25	9.5	0.03	0.01	89.9	0.5	2.0
2	7.5	5.5	7.5	7.5	0.05	0	89.9	2.5	4.0
2	7.5	7.5	8.25	9.5	0.03	0.01	89.9	2.5	4.0
3	7.5	5.5	7.5	7.5	0.05	0	80	1.5	3.0
3	7.5	7.5	8.25	9.5	0.03	0.01	80	1.5	3.0
4	7.5	5.5	7.5	7.5	0.05	0	70	1.5	3.0
4	7.5	7.5	8.25	9.5	0.03	0.01	70	1.5	3.0
5	7.5	5.5	7.5	7.5	0.075	0	89.9	1.5	3.0
5	7.5	7.5	8.25	9.5	0.05	0.01	89.9	1.5	3.0
6	7.5	5.5	7.5	7.5	0.035	0	89.9	1.5	3.0
6	7.5	7.5	8.25	9.5	0.02	0.01	89.9	1.5	3.0
7	7.0	5.5	7.0	7.5	0.05	0	89.9	1.5	3.0
7	7.0	7.5	7.25	9.5	0.03	0.01	89.9	1.5	3.0
8	7.5	6.0	7.5	8.0	0.05	0	89.9	1.5	3.0
8	7.5	8.0	8.25	10.0	0.03	0.01	89.9	1.5	3.0

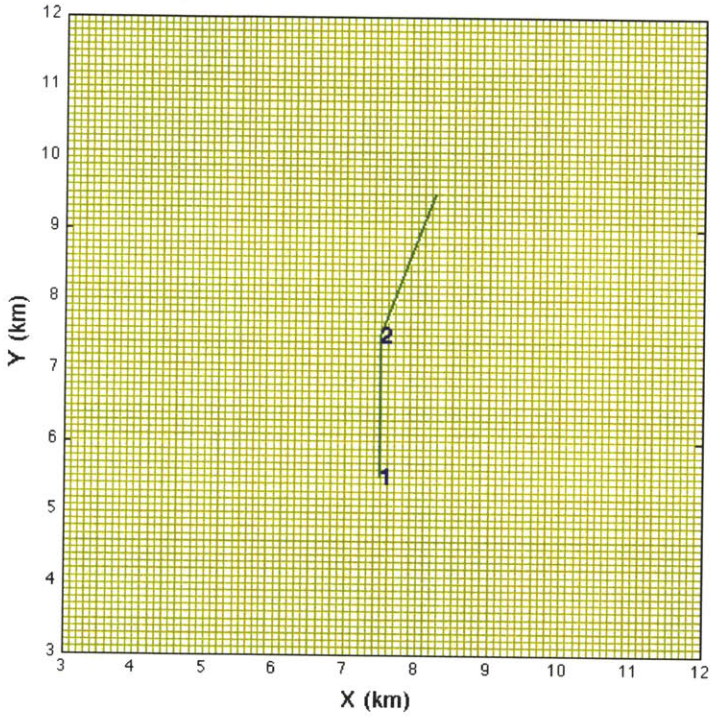

Figure 3.1: Strike slip reference faults and calculation grid

Table 3.2: Strike-slip Fault Model Statistics

Case	Average Displacement (mm)	Standard Deviation (mm)	Maximum (mm)	Minimum (mm)
Ref	0.10	0.51	1.39	-1.02
1	0.17	0.60	2.79	-2.27
2	0.06	0.38	0.80	-0.64
3	0.11	0.58	1.94	-1.31
3a	0.13	0.74	2.61	-1.63
4	0.10	0.78	2.09	-1.66
5	0.10	0.37	0.99	-0.70
6	0.10	0.51	1.27	-1.07
7	0.10	0.51	1.39	-1.02

3.1.1 Errors in Fault Depth

Fault depth model errors are both common and easy to identify. For equal faults with equal slip, the surface deformation due to a deep fault will have lower amplitude and broader lateral extent than the reference model. A shallow fault model will exhibit higher deformation and more sharply defined edges than the reference model. Figure 3.2 shows the deformation plots for the reference model, Case 1 (shallow) and Case 2 (deep). Figure 3.3 shows the differences between the reference model and Cases 1 and 2.

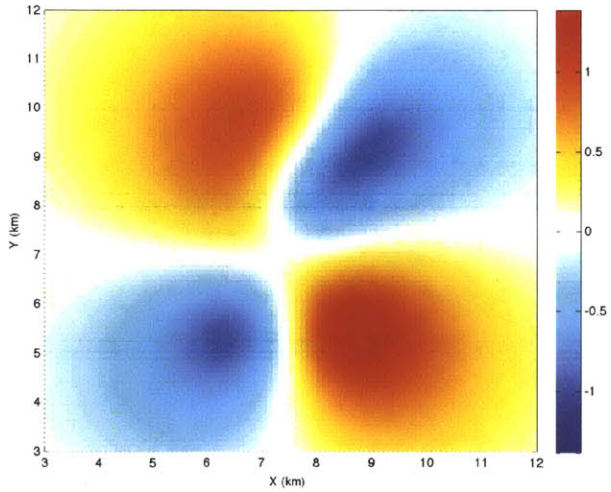

(a) Reference Model

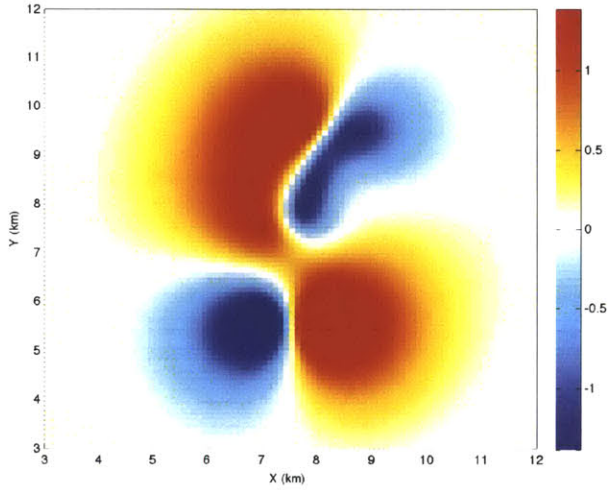

(b) Case 1 (shallow)

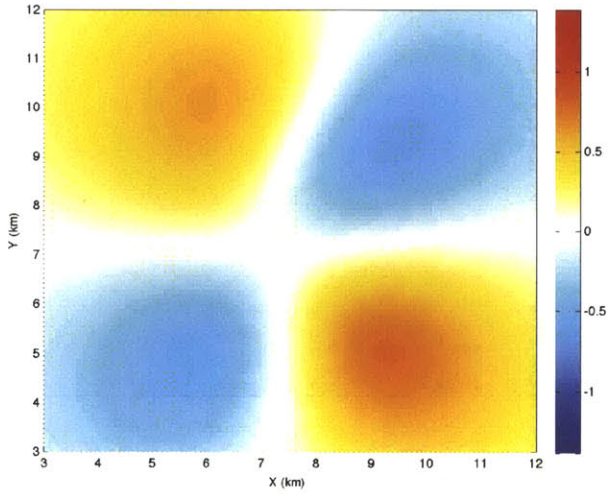

(c) Case 2 (deep)

Figure 3.2: Strike-slip: Vertical Displacements (mm)

Errors in fault depth are relatively easy to see from difference maps, either systematically too high or too low, or from the simple image statistics. Case 3 is 1 km shallower and Case 4 is 1 km deeper than the reference fault. Histogram plots of the data show the differences nicely (Figure 3.4).

The shallow fault shows broader tails and lower shoulders in the histogram, and the deeper fault is tightly peaked about zero deformation. The locations of the peak deformation do not change and the changes in the distribution are reasonably symmetric. The shallow fault has more instances of zero deformation than the reference model and the deep model has fewer, reflecting the change in lateral extent. Fault depth is also frequently subject to useful constraint by seismic data, although less so than many other parameters. Geodetic modelling alone can uniquely identify fault depth errors.

An error in slip dimension is most likely to be confused for a depth error. This is particularly plausible for strike-slip faults since deformation symmetry is maintained with slip errors. For dipping faults, in contrast, a change in slip results in a significant change in the symmetry of the lateral distribution of deformation and the location of deformation peaks. This will be discussed further in section 3.1.3.

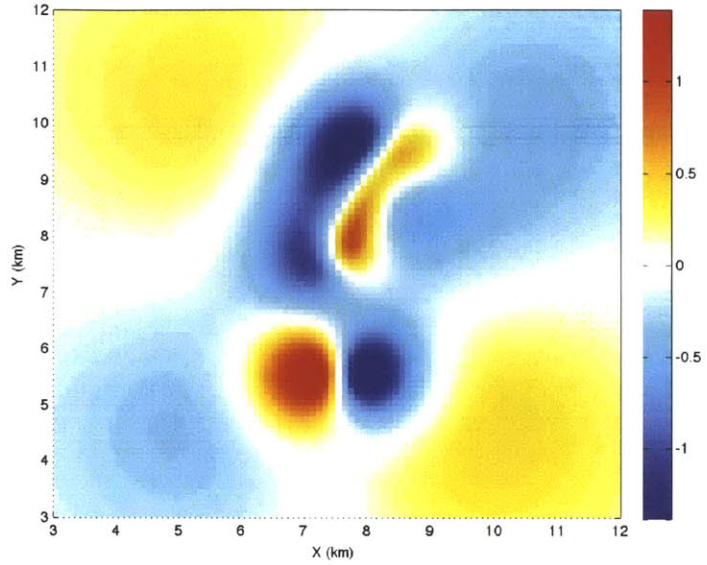

(a) Case 1 (shallow)

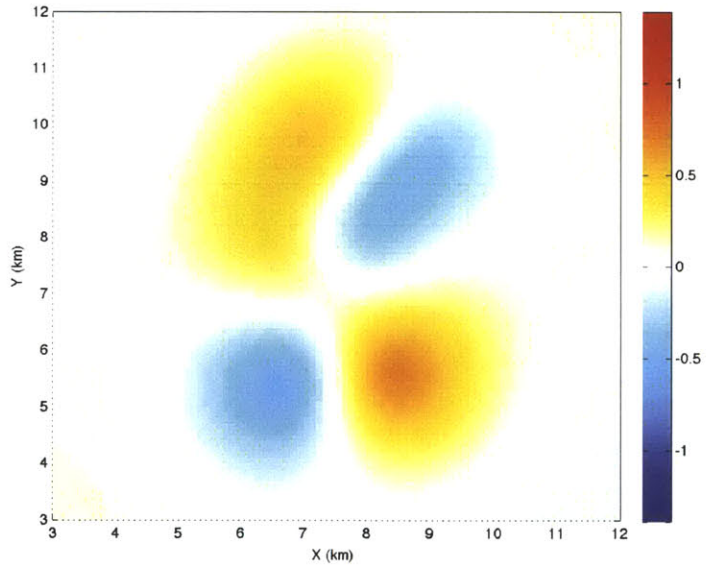

(b) Case 2 (deep)

Figure 3.3: Strike-slip Depth Error: Difference from Reference Model (mm)

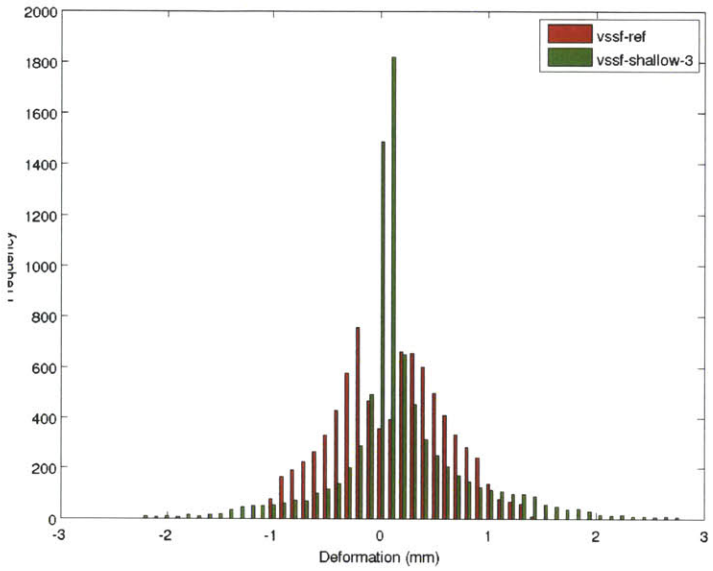

(a) Case 1 (shallow)

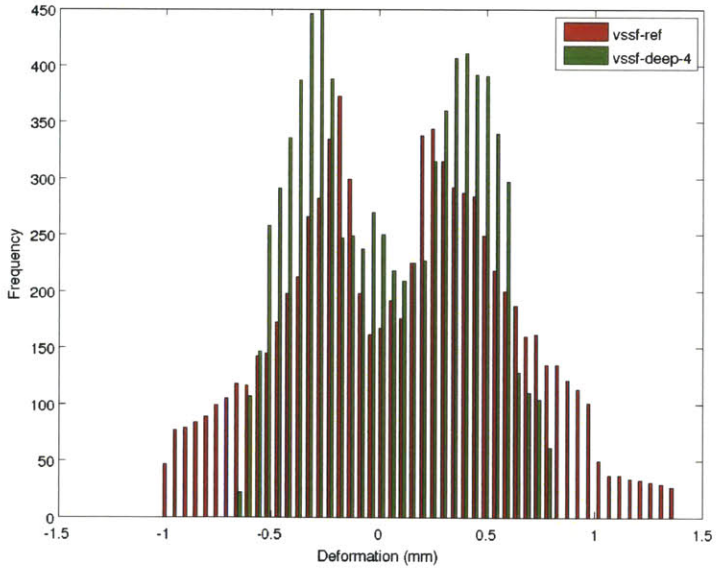

(b) Case 2 (deep)

Figure 3.4: Strike-slip Depth Error: Histogram of Case vs. Reference Model

3.1.2 Errors in Fault Dip

Fault dip errors are more difficult to constrain than depth or X-Y location errors. Seismic information is a potentially powerful additional tool, but there are some systematic changes in deformation symmetry with varying dip that can identify dip errors. Dip errors are particularly easy to detect for strike-slip faults because they are sub-vertical, so small dip changes result in large asymmetries in the deformation pattern. The gradient map is particularly useful in this case to identify the direction of the dip error. Figure 3.5 shows the deformation due to the vertical reference fault and faults oriented at 10 and 20 degrees from vertical towards the east.

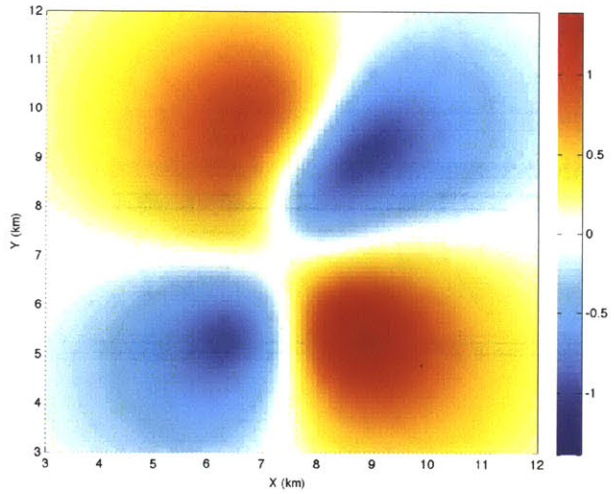

(a) Reference Model

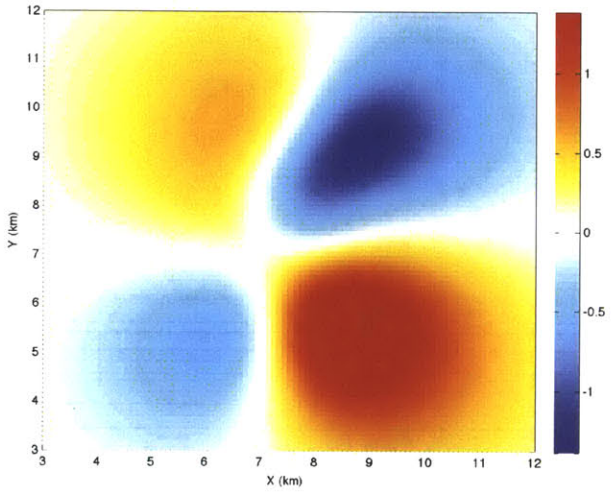

(b) Case 3 (10 deg)

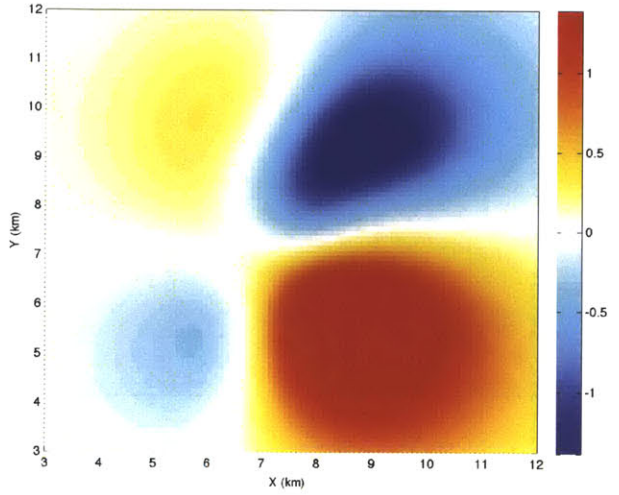

(c) Case 3a (20 deg)

Figure 3.5: Strike-slip Dip Error: Vertical Displacements (mm)

The difference maps in Figure 3.6 show a divide between the northern and southern halves reflecting the additive effect of the asymmetry. The reference model is relatively higher in both the northwest and northeast quadrants due to increased deformation (subsidence) in the northeast quadrant and decreased uplift in the northwest quadrant in Case 3. The lower half of the model shows a positive difference because the uplift in the southeast quadrant is increased and the subsidence in the southwest quadrant is diminished. The asymmetric deformation pattern and difference map result are accentuated in Case 4, which dips a further 10 degrees from vertical towards the east.

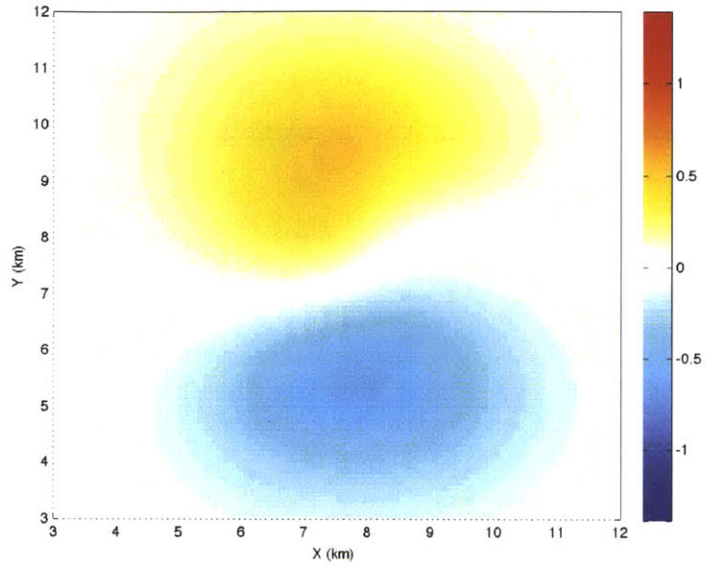

(a) Case 3 (10 deg off)

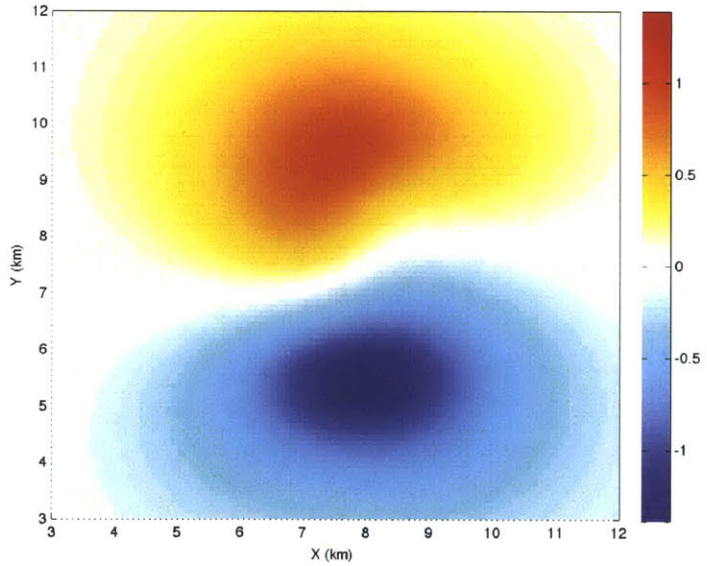

(b) Case 3a (20 deg off)

Figure 3.6: Strike-slip Dip Error: Difference from Reference Model (mm)

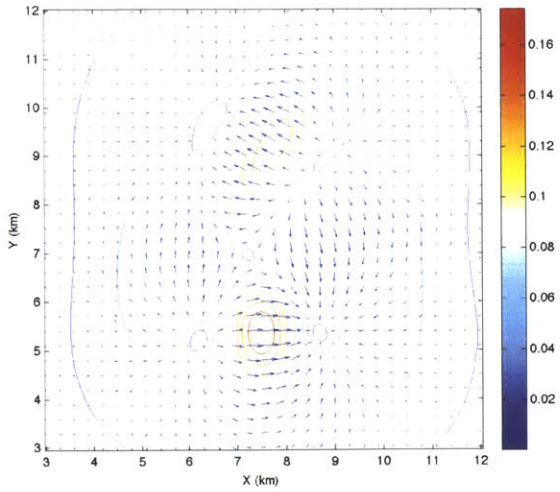

(a) Reference Model

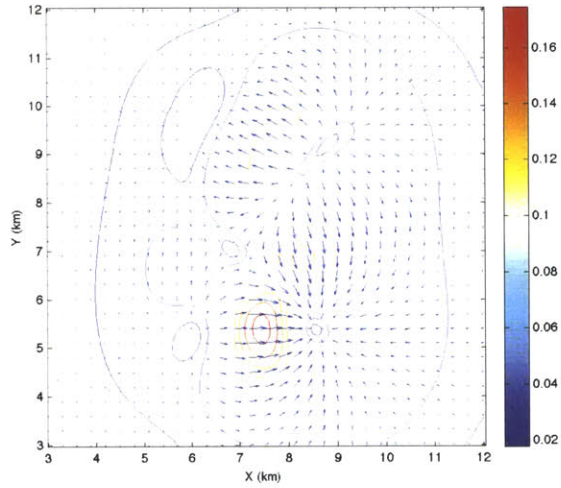

(b) Case 3 (10 deg off)

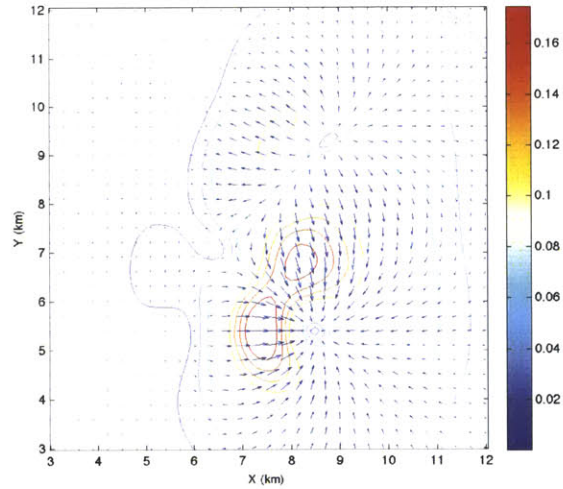

(c) Case 3a (20 deg off)

Figure 3.7: Strike-slip Dip Error Gradient: Direction Arrows and Magnitude Contours

Although the difference maps are useful and characteristic of a dip error in a strike-slip faulting regime, the difference map pattern is not unique. Spatial gradient maps tell a much clearer tale of the asymmetry. Figures 3.7 and 3.8 show gradient and gradient difference maps for Cases 3 and 3a. The arrows on the plots indicate the direction while the contours indicate the magnitude of the gradient at a specific point. Plotting the gradients in this way makes the plot and comparison independent of fault strike.

The reference model's gradient is symmetric since the fault is vertical. As the dip increases, first to 10 and then to 20 degrees to the east, the deformation becomes increasingly asymmetric and concentrated in the eastern half of the model. The gradient difference plots between the two models and the reference reinforce the conclusion from the simple difference maps that increasing deformation asymmetry is indicative of a dip error on a strike-slip fault. The sensitivity of the asymmetric deformation pattern to dip errors could point to an interesting alternative interpretation of asymmetric InSAR observations from Tibet (Peltzer et. al, [10], 1999) attributed to a variable elastic modulus.

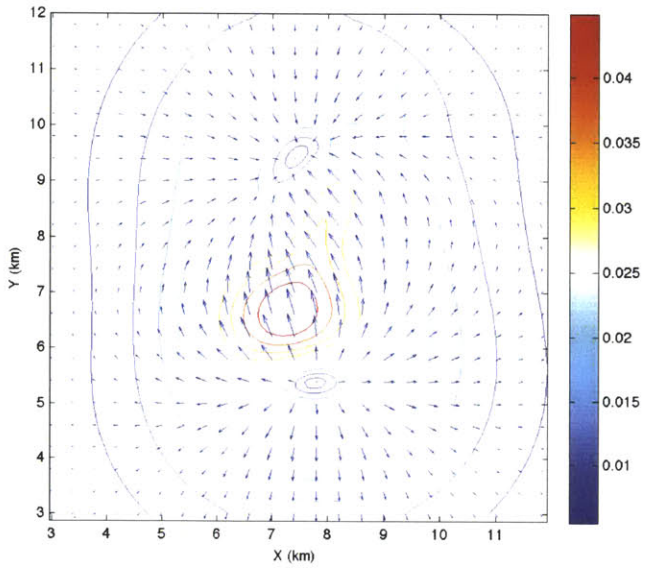

(a) Case 3 (10 deg off)

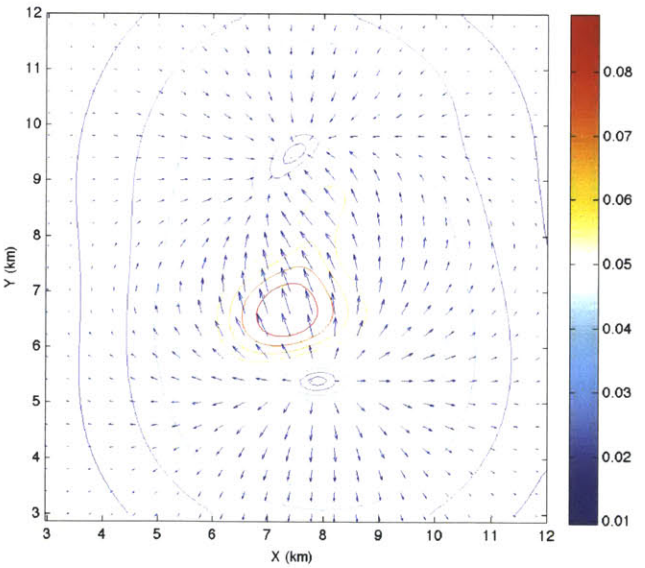

(b) Case 3a (20 deg off)

Figure 3.8: Strike-slip Dip Error: Vector Gradient Difference Plots

3.1.3 Errors in Slip Distance

The slip distance can be constrained seismically for a well-observed earthquake since earthquake magnitude is a linear function of slip distance and the rupture area. Geodetically, changing the slip without changing the size of the fault results in an increase or decrease in deformation. Figure 3.9 shows the reference model and the impact of increasing and decreasing the slip by approximately 50% in Cases 4 and 5 respectively.

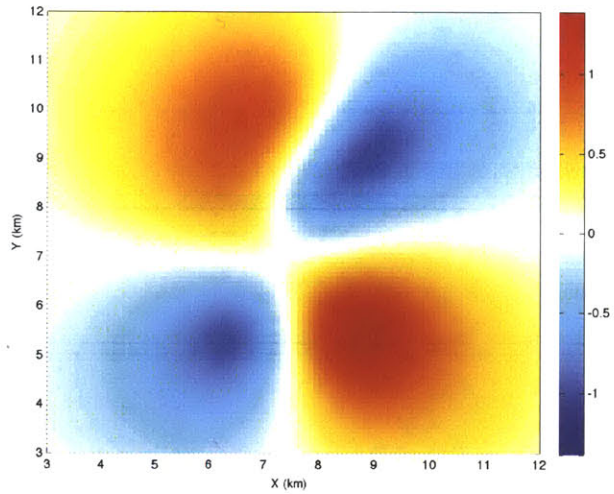

(a) Reference Model

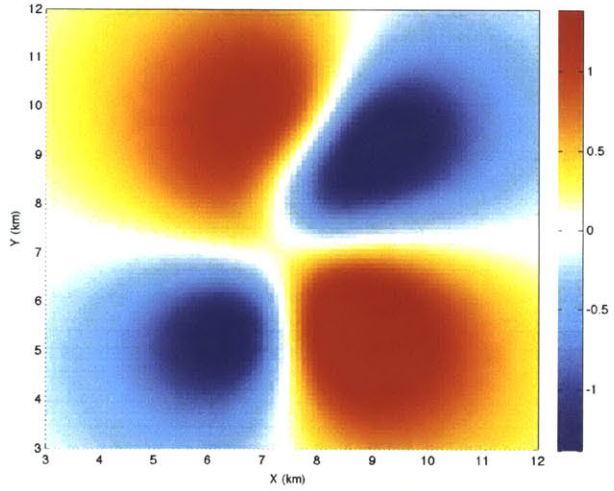

(b) Case 4 (more slip)

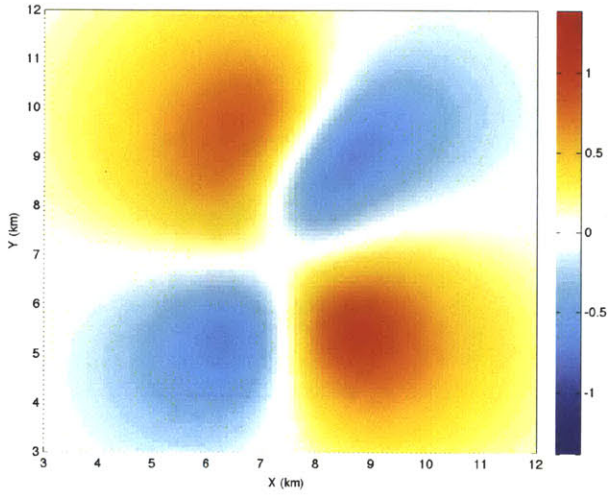

(c) Case 5 (less slip)

Figure 3.9: Strike-slip Slip Error: Vertical Displacements (mm) (cont.)

The difference maps for Cases 4 and 5 (Figure 3.10) show that the mismatch is concentrated at the deformation peaks instead of broadly across the entire model as in a depth error. The peak deformation areas in the vertical strike slip fault are symmetric so the increase or decrease in deformation is also symmetric for this type of error.

Slip errors of this simplified type look superficially similar to depth errors in the basic image statistics, but the increases or decreases in deformation are concentrated in the peak areas instead of spread across the model. This is clearly shown in Figure 3.11 by the narrowing of the deformation histogram under low slip and its broadening under high slip.

Figure 3.12 shows gradient plots, where gradient magnitude contours are overlain by arrows indicating the vector direction, for the reference model and Cases 4 and 5 (more slip and less slip respectively). The quiver plots show very clearly that changing the slip doesn't change the areal extent of deformation, only its magnitude. In contrast, changing the fault depth changes the lateral extent of deformation. A smaller area is affected more dramatically by a shallower fault and a larger area more gently deformed by a deep fault. The gradient difference plots (Figures 3.13) confirm the symmetric errors introduced by slip errors on a vertical strike-slip fault.

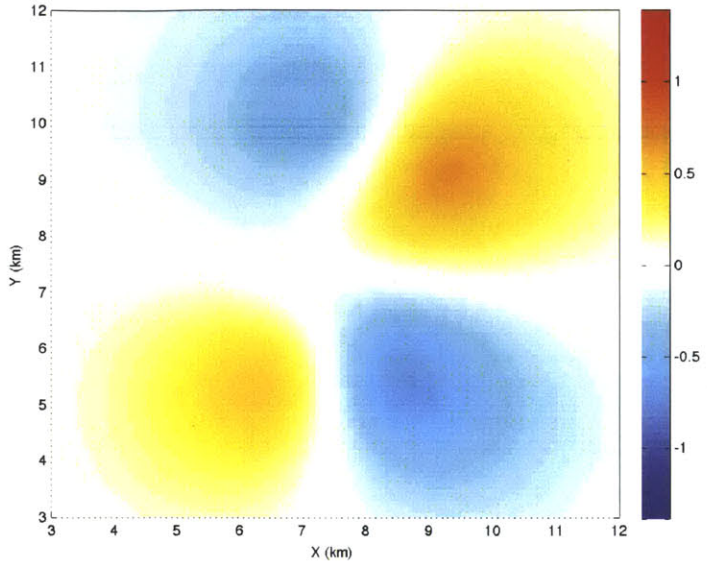

(a) Case 4 (more slip)

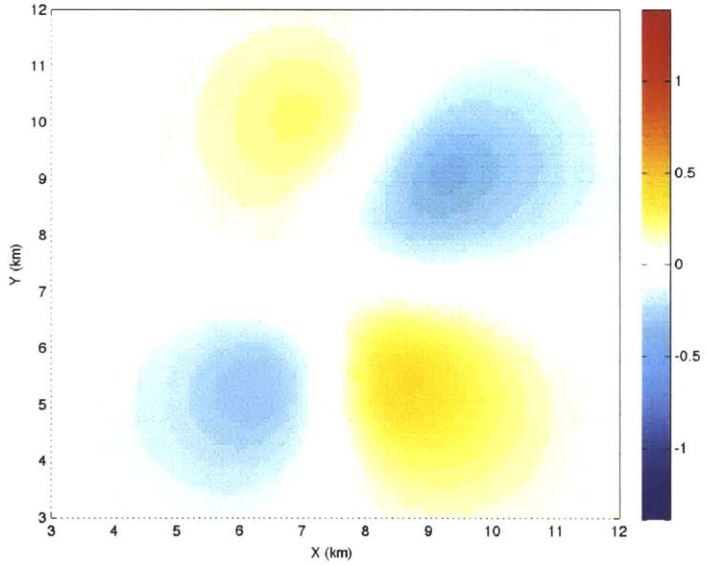

(b) Case 5 (less slip)

Figure 3.10: Strike-slip Slip Error: Difference from Reference Model (mm)

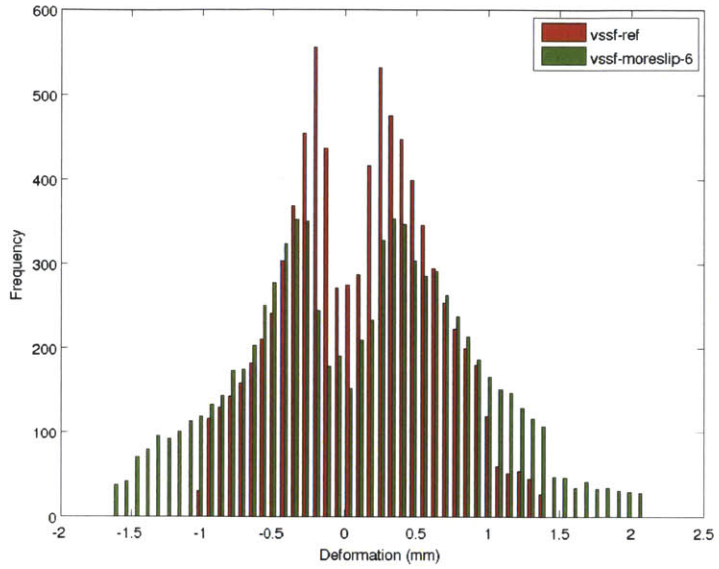

(a) Case 4 (more slip)

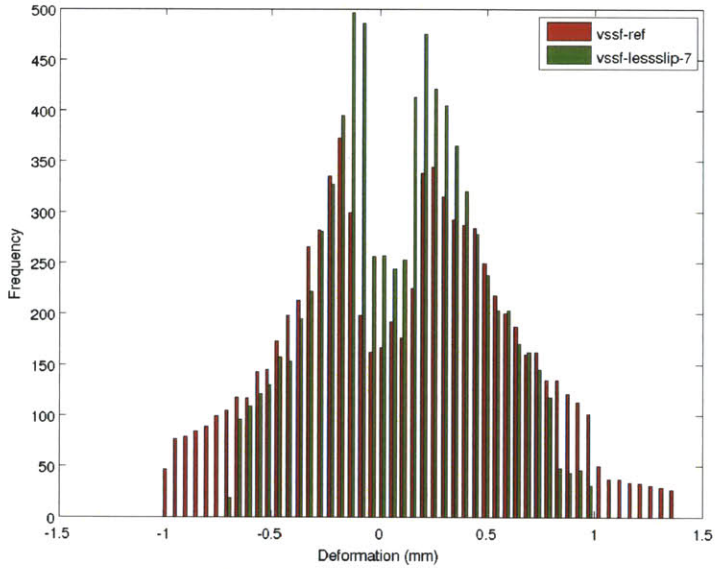

(b) Case 5 (less slip)

Figure 3.11: Strike-slip Slip Error: Histogram of Case vs. Reference Model

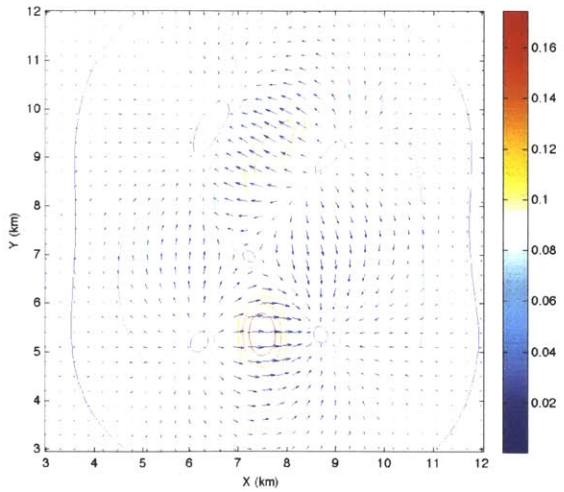

(a) Reference Model

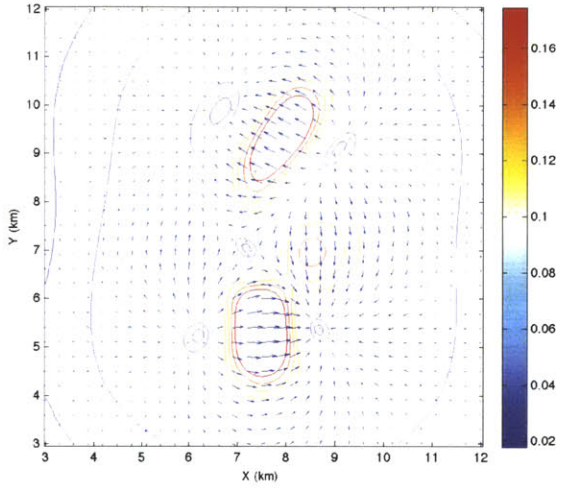

(b) Case 4 (more slip)

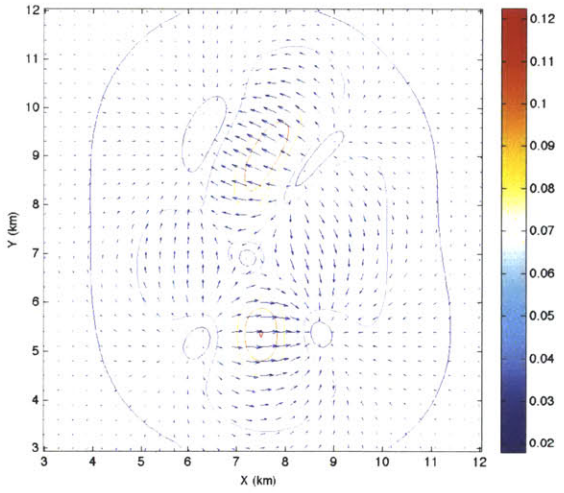

(c) Case 5 (less slip)

Figure 3.12: Strike-slip Slip Error: Gradient Direction Arrows and Magnitude Contours

Taken together, the test suite is able to uniquely identify slip errors for strike-slip faults since they result in increases in the peak deformation without significant changes in the location or extent of the deformation. The cases in this section do not preserve seismic moment, potentially a useful constraint available for medium and large earthquakes.

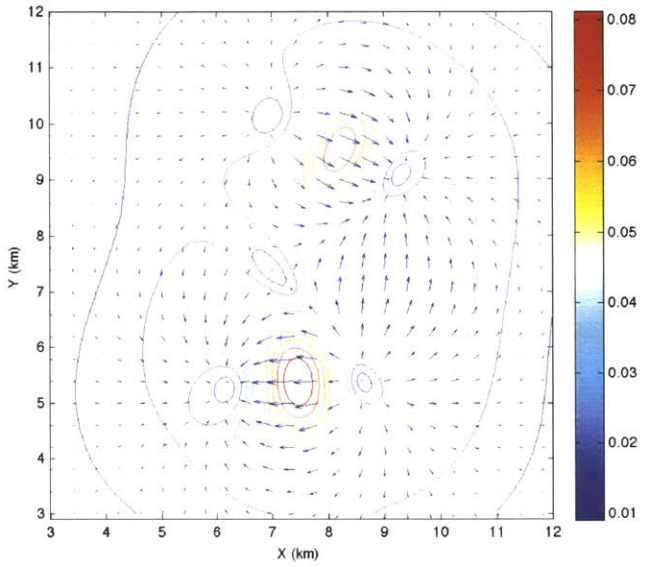

(a) Case 4 (more slip)

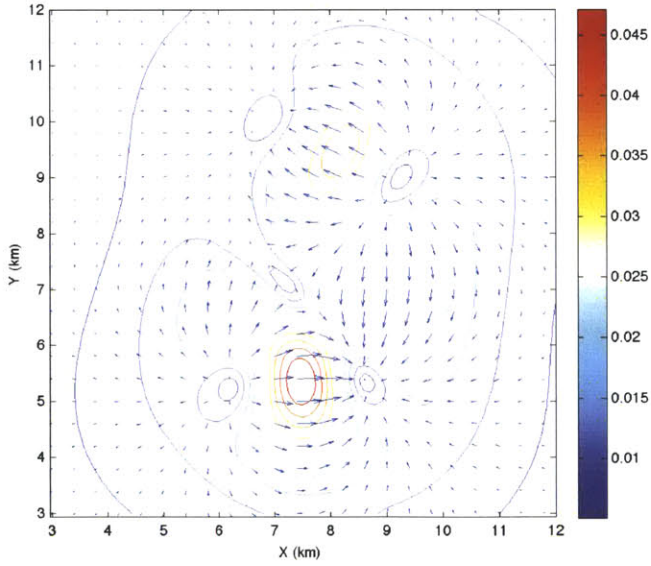

(b) Case 5 (less slip)

Figure 3.13: Strike-slip Slip Error: Vector Gradient Difference Plots

3.1.4 Errors in Fault Location: Displacement in X or Y direction

Errors in the X-Y placement of a fault are particularly obvious in strike-slip faulting and are also among the most easily corroborated by non-InSAR data, eg. earthquake locations, exploration seismic data or geologic surface expression of the fault. Figure 3.14 shows the vertical displacements measured due to the reference model, Case 6 (offset 500m in X) and Case 7 (offset 500m in Y). In this case the only difference between the three models is the fault's position in X-Y space. Figure 3.15 shows difference maps between Cases 6 and 7 and the reference model, which illustrate the offset.

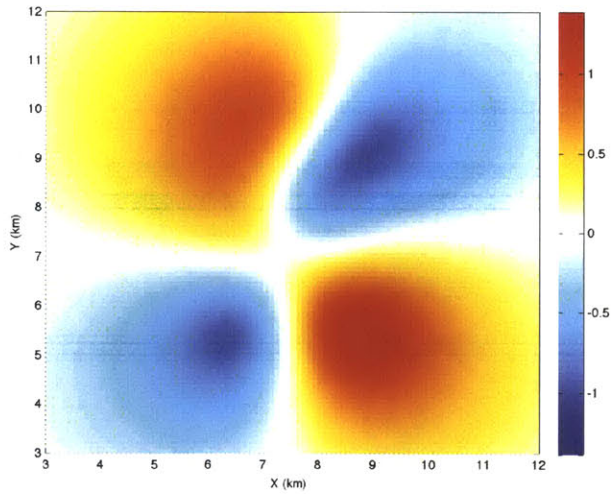

(a) Reference Model

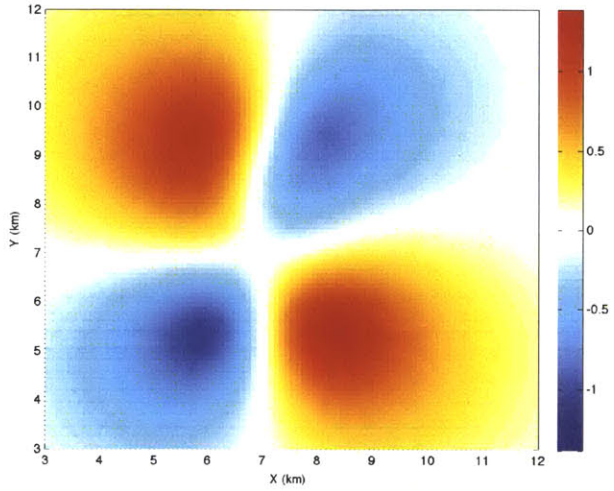

(b) Case 6

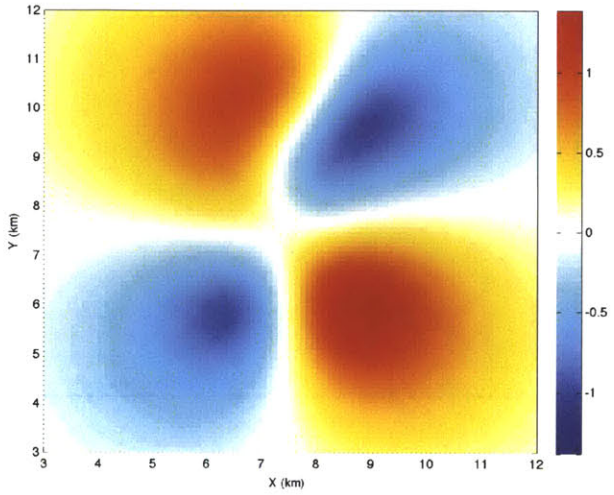

(c) Case 7

Figure 3.14: Strike-slip Location Error: Vertical Displacements (mm)

To identify X-Y errors algorithmically a modelling program could make a series of models with increasing offsets in both directions, calculate the difference maps and then make profiles of Error vs. Offset at specific points. The X and Y profiles will have minima at the correct locations provided that the modelled fault's strike is correct.

Fault X-Y location is a parameter that benefits from a lot of external information. Faults important enough to have InSAR images taken at regular intervals are frequently instrumented for seismic data collection (tectonic faults), visible on exploration seismic data (reservoir faults) and are frequently instrumented with GPS stations. In addition, tectonic strike-slip faults are often visible at the surface. The X-Y location and fault length are very important parameters whose precision should be improved with all available types of data. These errors are sufficiently unique and easily resolved that they will not be presented separately for the other fault types.

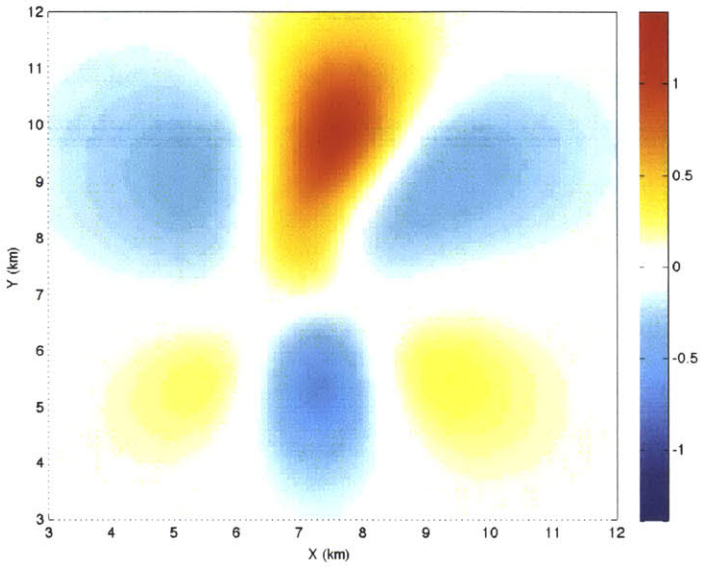

(a) Case 6

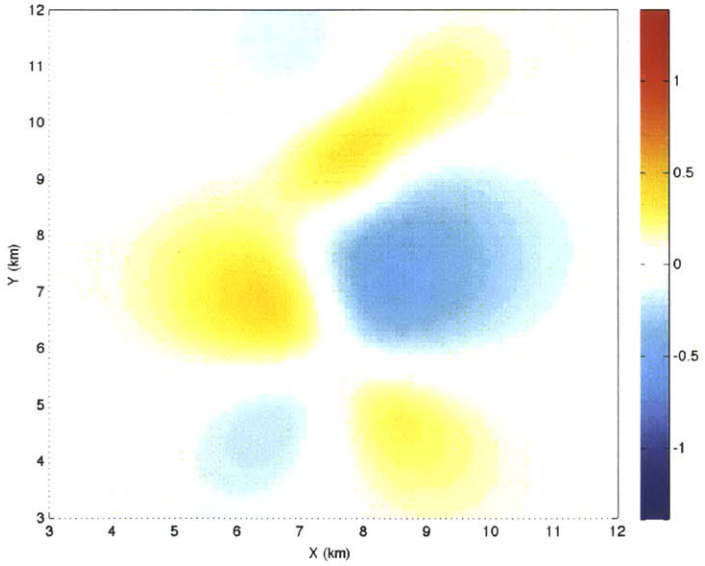

(b) Case 7

Figure 3.15: Strike-slip Location Error: Difference from Reference Model (mm)

3.1.5 Summary of Strike-slip Faulting Errors

Fault depth and slip distance errors both result in systematically high or low displacements visible in the difference maps and average statistics. The differentiating factor between the two is that the deformation changes due to slip distance errors presents as an exaggeration or diminution of the peaks of existing deformation pattern but a depth error significantly changes the areal extent of the deformation. External information, particularly seismic data, could be a useful additional constraint on this error type. Dip errors on strike-slip faults result in easily identifiable asymmetric deformation patterns, which are particularly visible on gradient maps. Location errors in X and Y are easily identified in isolation and can be constrained by many other types of geophysical and geological data.

3.2 Normal Faulting

Normal faults are common in extensional tectonic settings where one side of a fault moves downwards past the other as the compressive stress is reduced. Pure dip-slip motion is considered in this section, i.e. the displacement is vertical in the plane of the fault. Earthquakes on normal faults are generally smaller than on other types of faults because extensional strain can be relieved in smaller increments than strain caused by crustal shortening.

Cases 1 and 2 show the deformation due to faults that are shallower

and deeper than the reference model. Cases 3 and 4 see the faults dipping at 10 degrees shallower and deeper, respectively, than the reference model. Cases 5 and 6 see less and more slip than the reference model. The X and Y offset cases are not presented because their identification and processing is not notably different than the methods developed for strike-slip faulting.

The fault parameters for all of the cases in this section are summarized in Table 3.3. The faults for the reference case and grid (100m spacing) are shown in Figure 3.16. Basic image statistics for each of the cases are summarized in Table 3.4. All subsequent models in this section were created by modifying single parameters in the reference model, which is treated as a fully processed interferogram collected over a field site.

Table 3.3: Normal Fault Model Parameters

Case	X start (km)	Y start (km)	X end (km)	Y end (km)	Right-lat Slip (m)	Reverse Slip (m)	Dip (deg)	Fault Top (km)	Fault Bottom (km)
ref	7.5	5.5	7.5	7.5	0	-0.05	60	1.5	3.0
ref	7.5	7.5	8.25	9.5	0	-0.05	55	1.25	3.25
1	7.5	5.5	7.5	7.5	0	-0.05	60	1	2.5
1	7.5	7.5	8.25	9.5	0	-0.05	55	0.75	2.75
2	7.5	5.5	7.5	7.5	0	-0.05	60	2	3.5
2	7.5	7.5	8.25	9.5	0	-0.05	55	1.75	3.75
3	7.5	5.5	7.5	7.5	0	-0.05	50	1.5	3.0
3	7.5	7.5	8.25	9.5	0	-0.05	45	1.25	3.25
3	7.5	5.5	7.5	7.5	0	-0.05	30	1.5	3.0
3	7.5	7.5	8.25	9.5	0	-0.05	25	1.25	3.25
4	7.5	5.5	7.5	7.5	0	-0.05	70	1.5	3.0
4	7.5	7.5	8.25	9.5	0	-0.05	65	1.25	3.25
5	7.5	5.5	7.5	7.5	0	-0.03	60	1.5	3.0
5	7.5	7.5	8.25	9.5	0	-0.03	55	1.25	3.25
6	7.5	5.5	7.5	7.5	0	-0.08	60	1.5	3.0
6	7.5	7.5	8.25	9.5	0	-0.08	55	1.25	3.25

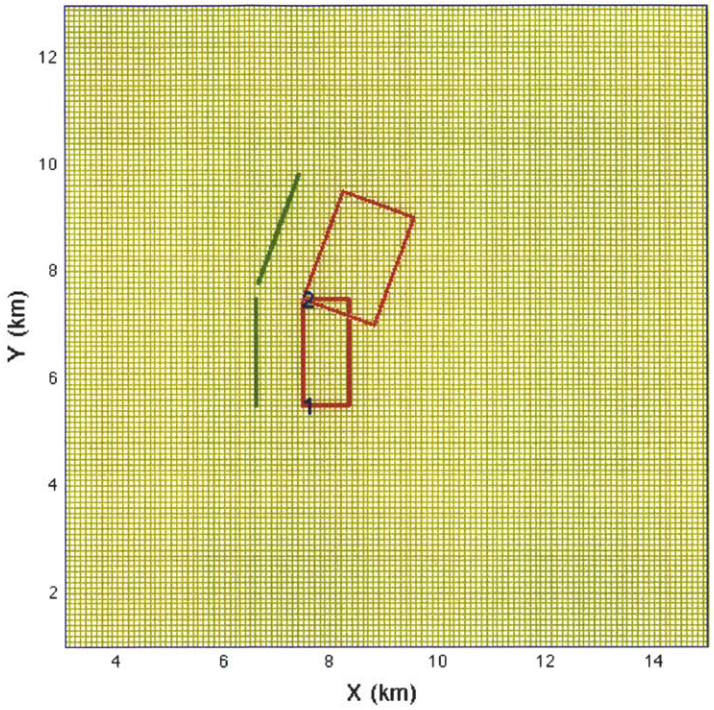

Figure 3.16: Normal fault reference model and calculation grid

Table 3.4: Normal Fault Model Statistics

Case	Average Displacement (mm)	Standard Deviation (mm)	Maximum (mm)	Minimum (mm)
Ref	-1.7	2.8	1.3	-14.6
1	-1.8	3.5	1.8	-20.3
2	-1.5	2.3	0.9	-10.8
3	-2.2	3.9	0.9	-19.9
3a	-4.5	7.4	0.3	-34.6
4	-1.3	2.0	1.6	-10.4
5	-1.0	1.7	0.8	-8.8
6	-2.7	4.5	2.0	-23.4

3.2.1 Errors in Fault Depth

Steeply-dipping normal faults result primarily in surface subsidence. For faults with intermediate or shallow dip X-Y deformation becomes increasingly important, but is not considered for these models since InSAR data cannot yet be separated into vector components. Cases 1 and 2, translations of the same fault shallower and deeper respectively, are shown with the reference model in Figure 3.17. The shallower fault results in a smaller area of more intense deformation (average: -1.8mm, peak: -20.3mm). The deeper fault sees its deformation diminished (average: -1.5mm, peak:-10.8mm) but spread over a larger area.

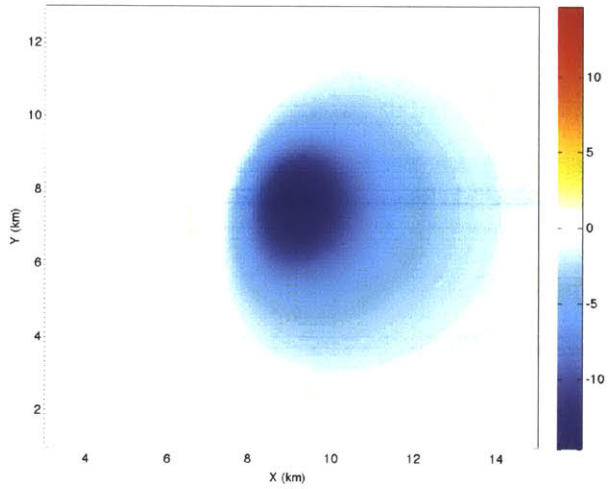

(a) Reference Model

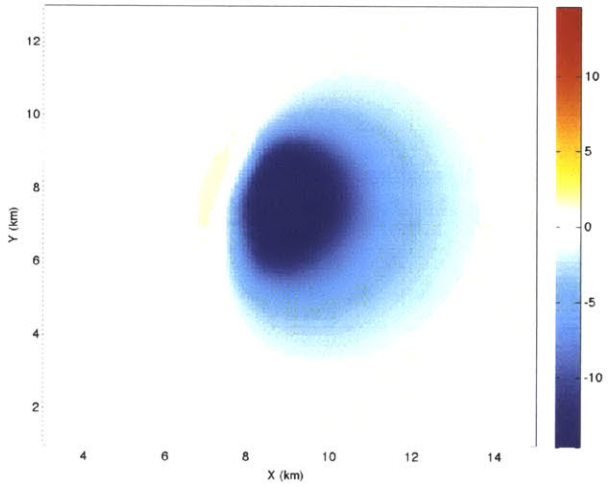

(b) Case 1 (shallow)

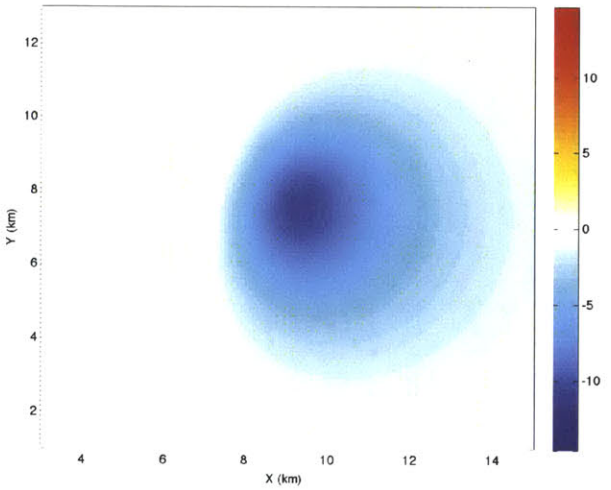

(c) Case 2 (deep)

Figure 3.17: Normal Fault Depth Error: Vertical Displacements (mm)

Errors in fault depth are relatively easy to see from difference maps (Figure 3.18) or from the basic image statistics. For example, an average deformation that is too high in the presence of a similar distribution and standard deviation indicates a shallow fault. Histogram plots (Figure 3.19) of the data show the differences nicely, particularly in the highly deformed tails. Case 1 is 500m shallower and Case 2 is 500m deeper than the reference fault.

The shallow fault shows broader tails and lower shoulders in the histogram, and the deeper fault is tightly peaked about zero deformation. Fault depth is also frequently subject to useful constraint by seismic data, but geodetic modelling alone can constrain it given that the other fault geometry parameters are constrained.

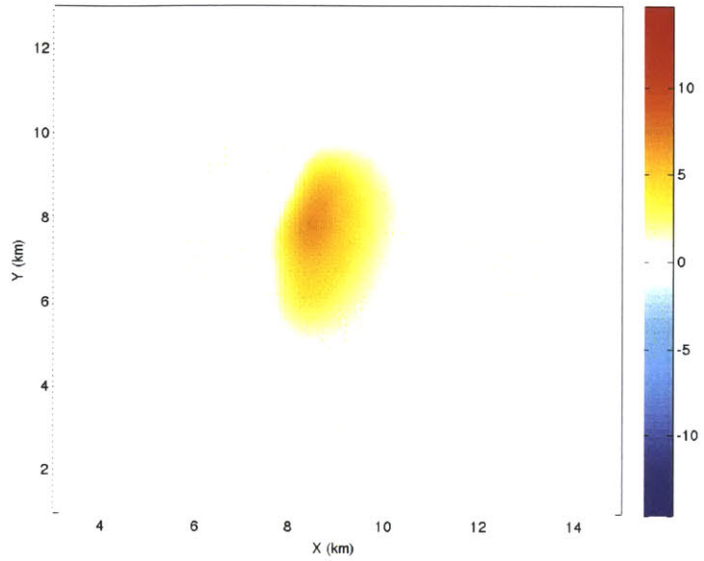

(a) Case 1 (shallow)

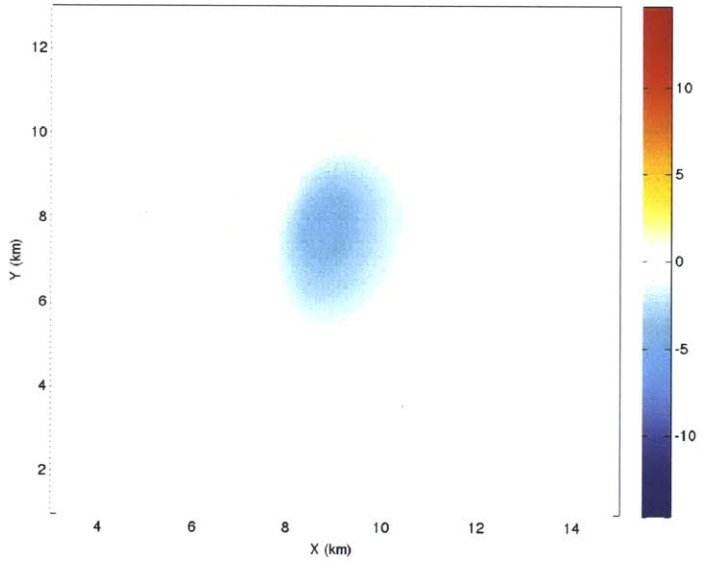

(b) Case 2 (deep)

Figure 3.18: Normal Fault Depth Error: Difference from Reference Model (mm)

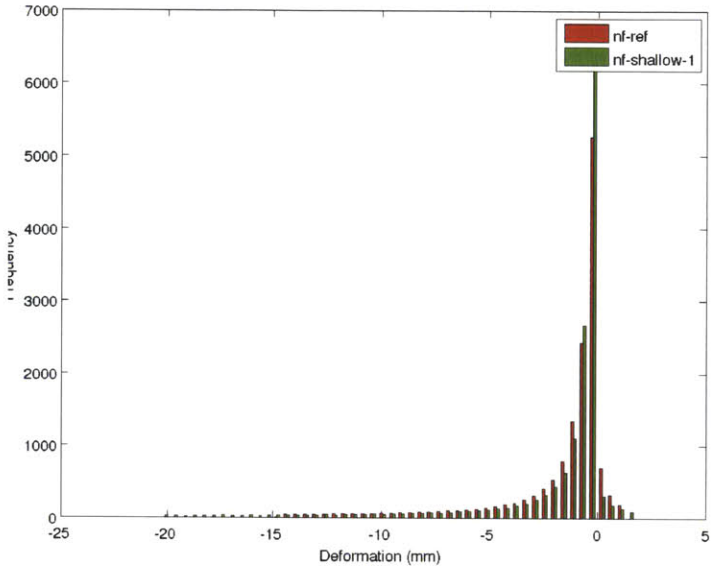

(a) Case 1 (shallow)

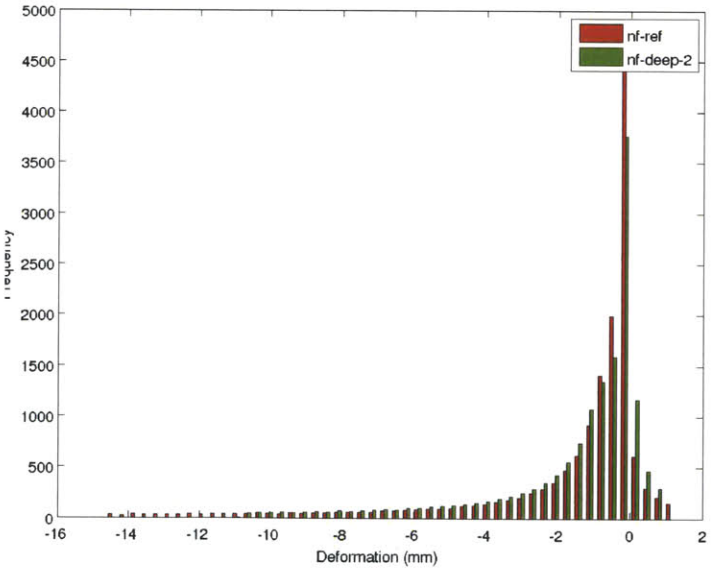

(b) Case 2 (deep)

Figure 3.19: Normal Fault Depth Error: Histogram of Case vs. Reference Model

3.2.2 Errors in Fault Dip

Dip errors are difficult to constrain, particularly for faults with shallow or intermediate dip. Seismic information is a potentially powerful additional tool, but there are some systematic changes in deformation symmetry with varying dip that can identify dip errors. Dip errors are harder to identify on dipping faults than vertical faults because the asymmetry generated by the error is more subtle and easily confused with fault depth errors. Figure 3.20 shows the surface deformation for the reference model and Cases 3, 3a, 4a: 10 degrees shallower, 30 degrees shallower and 10 degrees steeper respectively. The difference maps are shown in Figure 3.21 and histograms of the deformation are shown in Figure 3.22. Gradient and Gradient difference plots are shown for the three models in Figures 3.23 and 3.24.

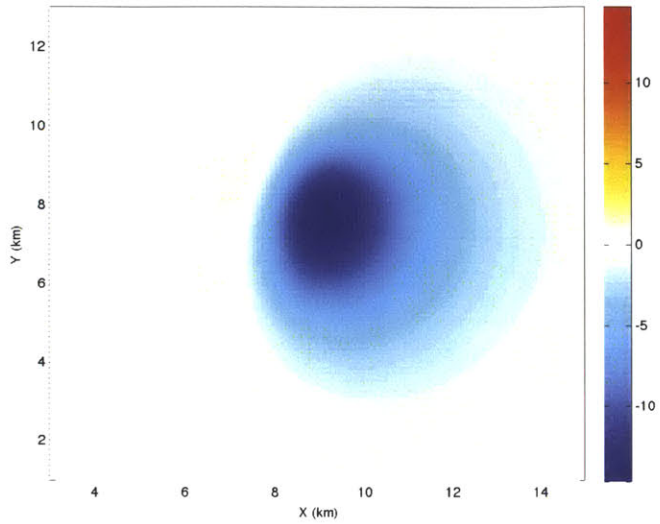

(a) Reference Model

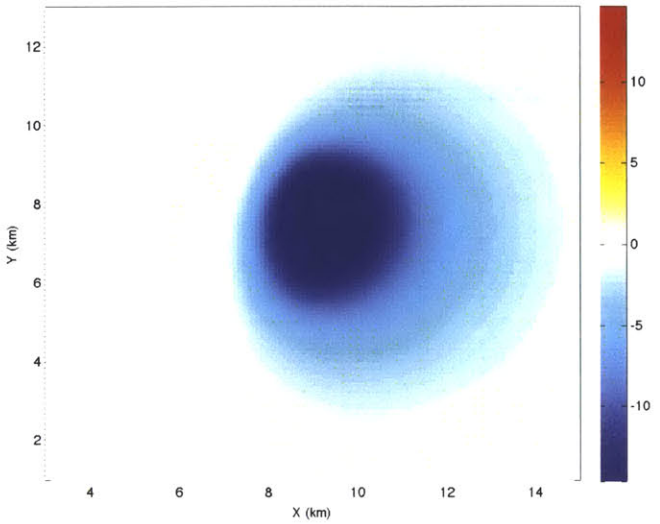

(b) Case 3 (10 deg shallow)

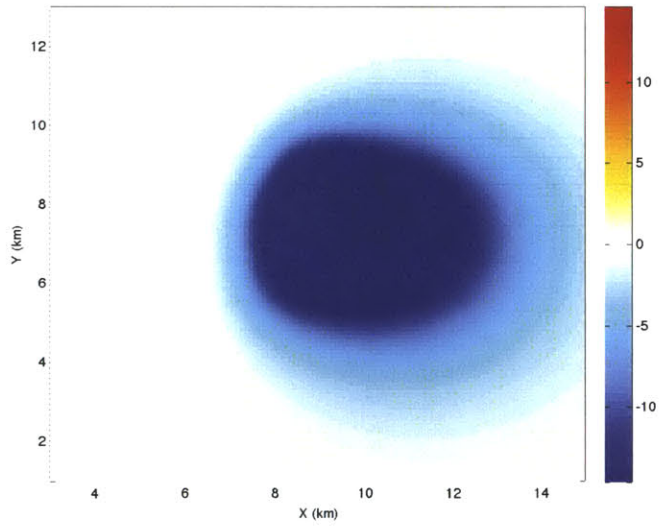

(c) Case 3a (30 deg shallow)

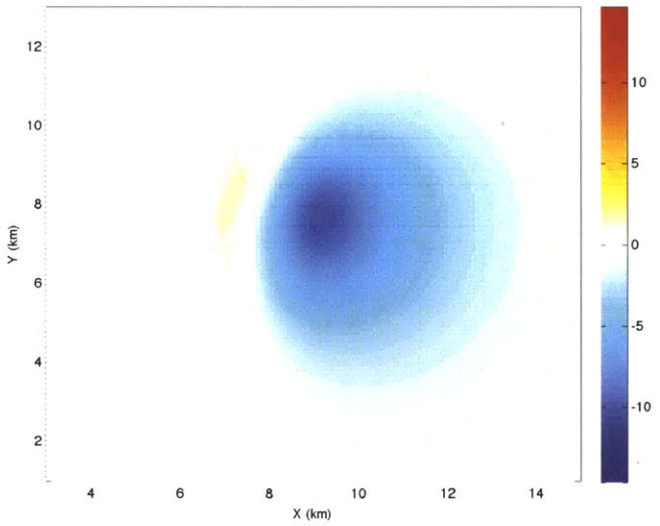

(d) Case 4 (10 deg steep)

Figure 3.20: Normal Fault Dip Error: Vertical Displacements (mm)

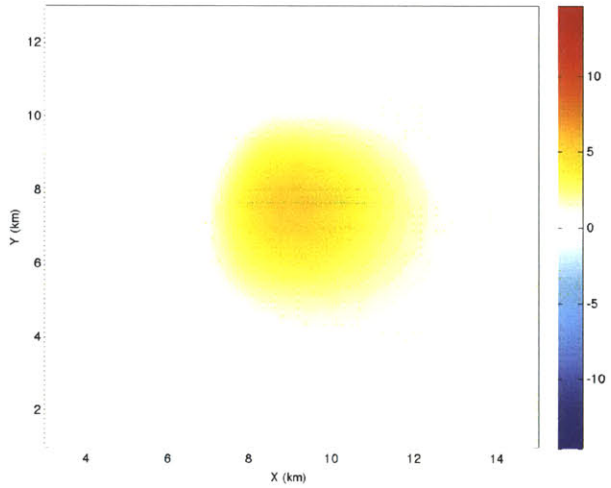

(a) Case 3 (10 deg shallow)

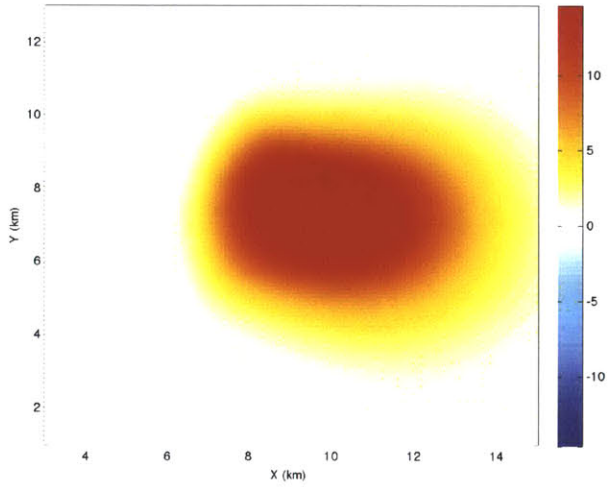

(b) Case 3a (30 deg shallow)

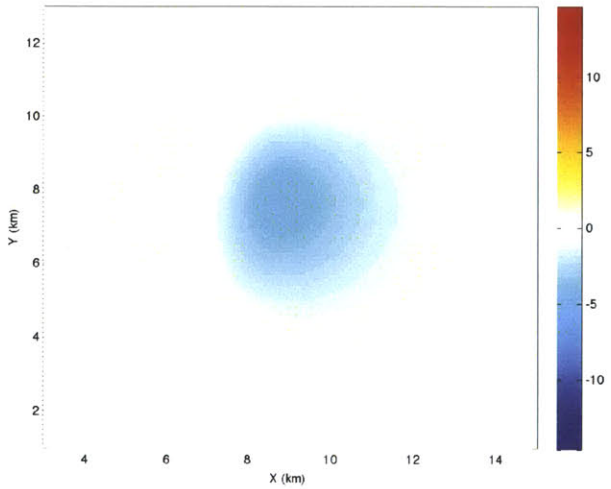

(c) Case 4 (10 deg steep)

Figure 3.21: Normal Fault Dip Error: Difference from Reference Model (mm)

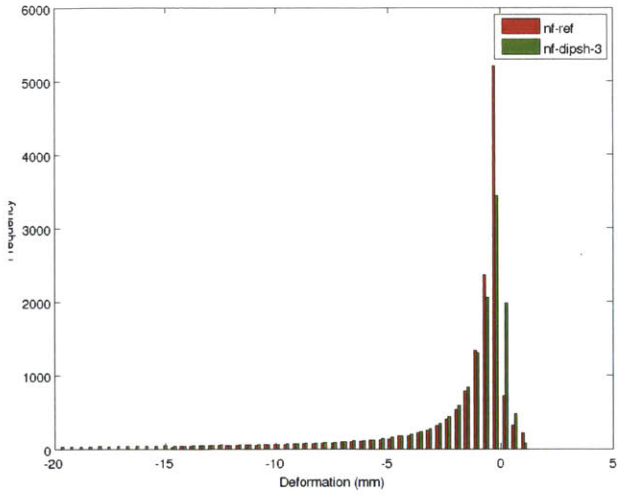

(a) Case 3 (10 deg shallow)

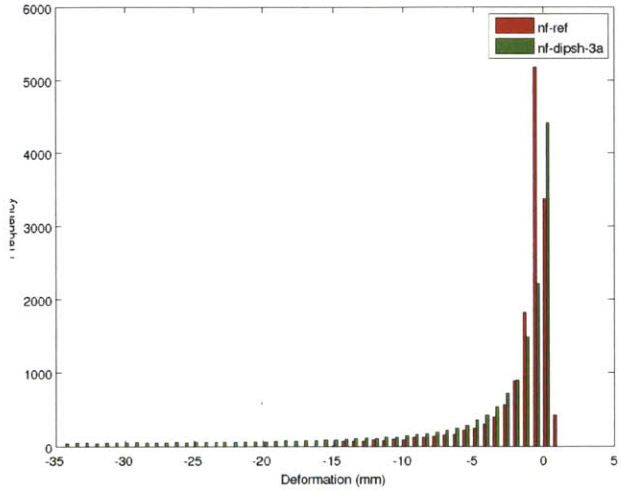

(b) Case 3a (30 deg shallow)

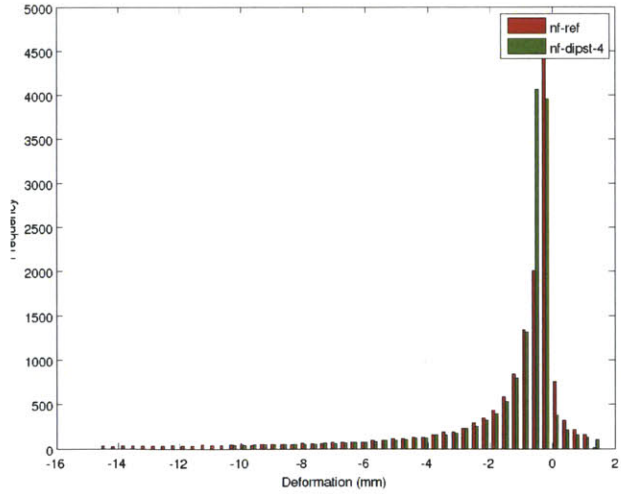

(c) Case 4 (10 degree steep)

Figure 3.22: Normal Fault Dip Error: Histogram of Case vs. Reference Model

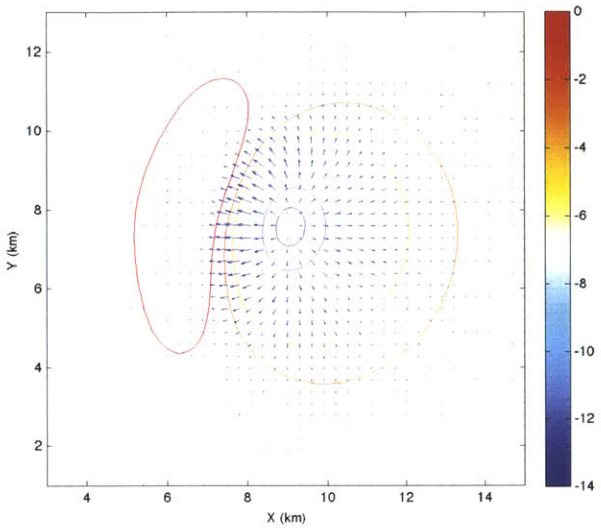

(a) Reference Model

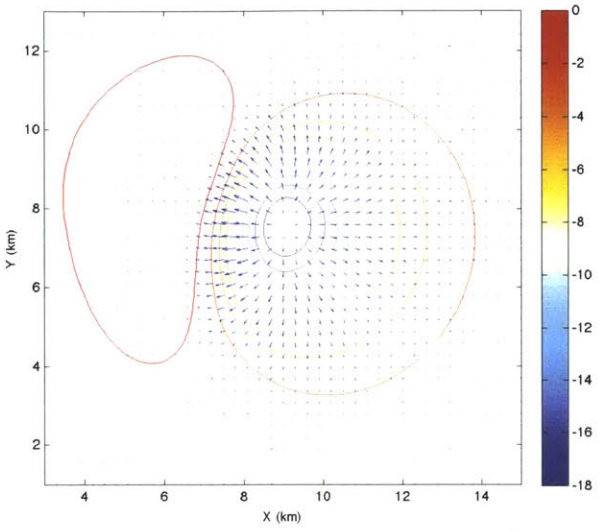

(b) Case 3 (10 deg shallow)

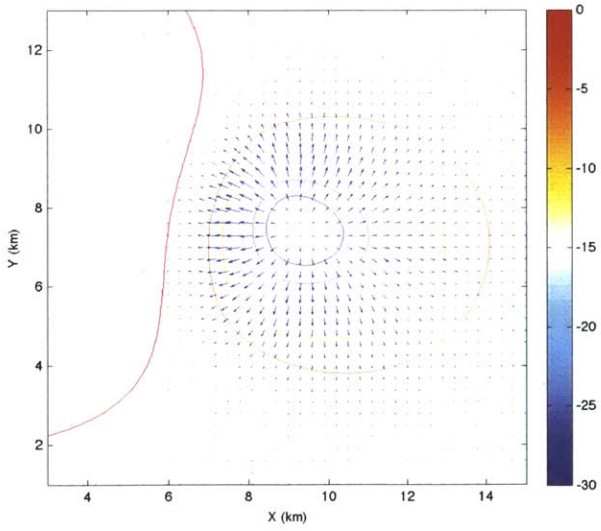

(c) Case 3a (30 deg shallow)

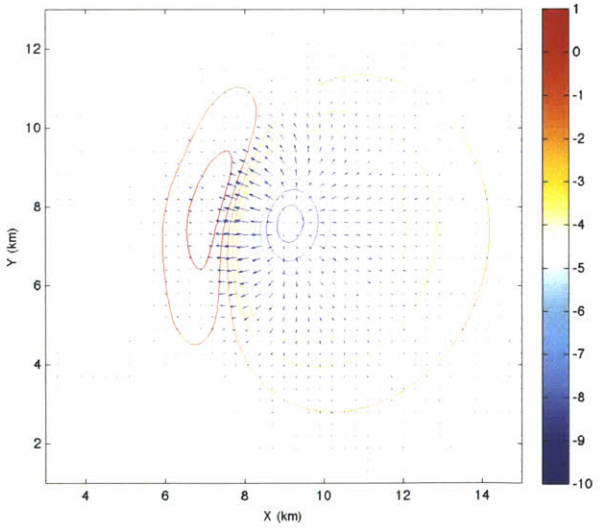

(d) Case 4 (10 degree steep)

Figure 3.23: Normal Fault Dip Error: Gradient Direction Arrows and Magnitude Contours

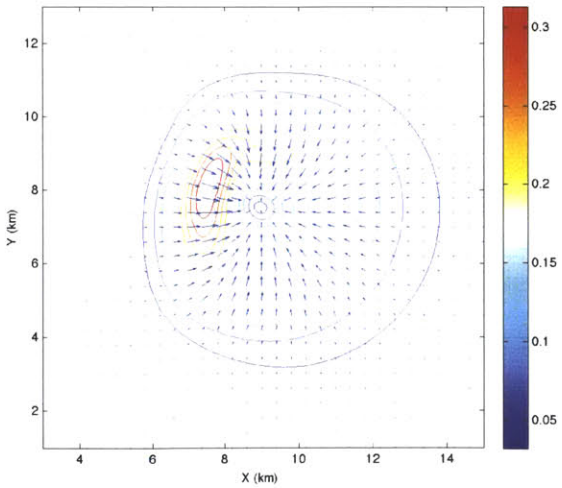

(a) Case 3 (10 deg shallow)

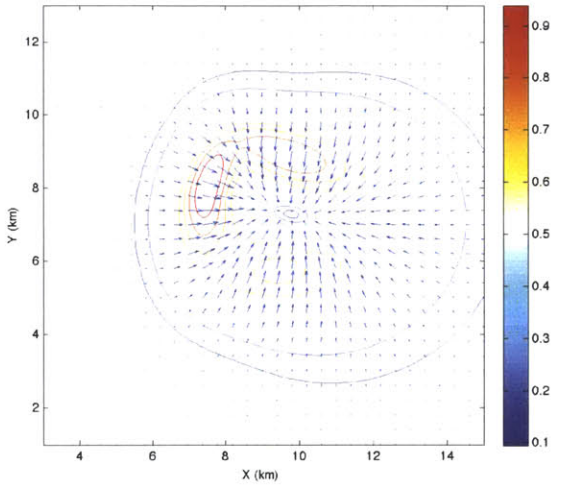

(b) Case 3a (30 deg shallow)

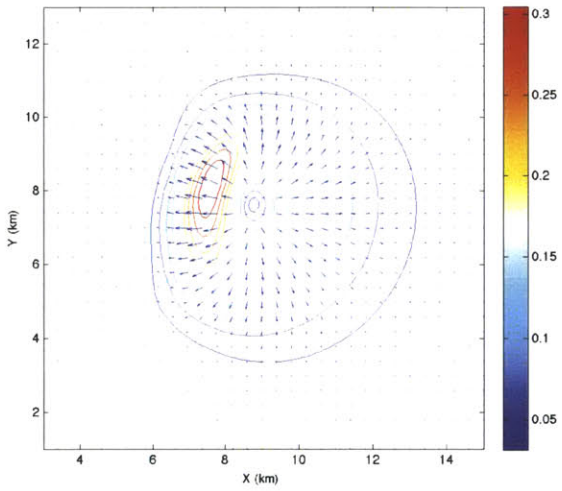

(c) Case 4 (10 degree steep)

Figure 3.24: Normal Fault Dip Error: Vector Gradient Difference Plots

Although superficially similar to depth errors, the deformation changes caused by dip errors remain localized at the peak deformation; the areal extent of deformation does not change significantly. The histograms for dip errors illustrate their subtlety very well: dip errors are much more similar to the reference histogram than any other error type, particularly in the deformation tails.

Unlike strike-slip faulting, asymmetry in the deformation pattern is difficult to identify for the smaller 10 degree errors. The 30 degree dip error shows substantial asymmetry, but this level of error is probably unrealistic since fault dips can usually be constrained much better than 30 degrees from seismic and other data.

The gradient maps are useful for identifying the direction of the dip error (shallower vs. steeper), since the errors are mirror images on the gradient difference maps. It appears that there is a limit to the sensitivity of dip errors that can be uniquely identified using geodetic models alone since the 10 degrees errors are poorly resolved. Accordingly, external constrains on fault dip estimates appear to be particularly important for faults of intermediate dip.

3.2.3 Errors in Slip Distance

The geodetic response of to a change in slip without a change in fault dimension is a net increase or decrease in deformation, but the magnitude of the earthquake also increases or decreases. Slip errors of this simplified type are the least realistic of the reductionist cases presented. However, identifying slip errors in this simplified static fault area case is an important first step towards developing more robust tests for magnitude-preserving slip/fault area models. Figures 3.25 and 3.26 show the deformation and difference maps for the reference model and Cases 5 and 6.

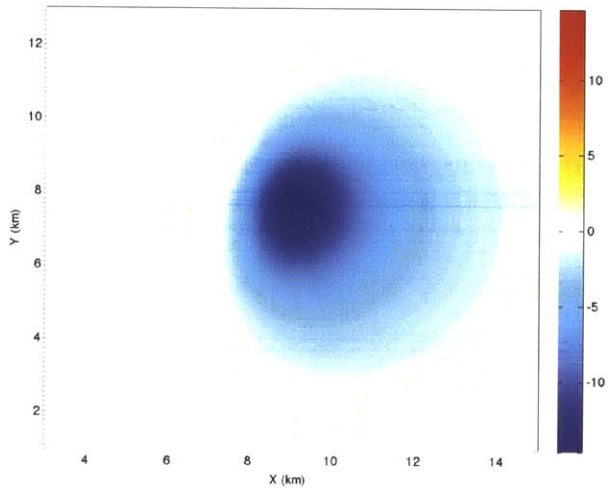

(a) Reference Model

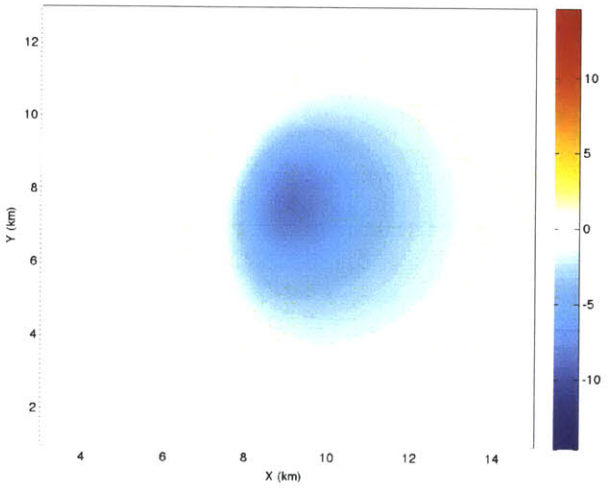

(b) Case 5 (less slip)

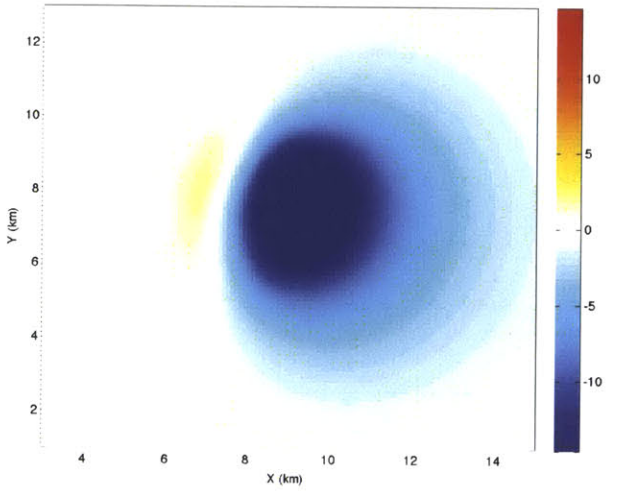

(c) Case 6 (more slip)

Figure 3.25: Normal Fault Slip Error: Vertical Displacements (mm) (cont.)

Slip errors of this type look superficially similar to both depth errors and fault dip errors. The main differentiating factor from depth errors is the concentration of changes in deformation at the peak areas instead of spread evenly across the model. The main differentiating factor from the dip errors is that the histogram tails for slip errors are much more different from the reference model. This is clearly shown in Figure 3.27 by the slight narrowing of the deformation histogram under low slip, its broadening under high slip and the respectively suppressed and accentuated tails. The gradient and gradient difference maps (Figures 3.28 and 3.29) for all three error types are quite similar but the differences in the slip error gradients are somewhat larger than those of dip errors.

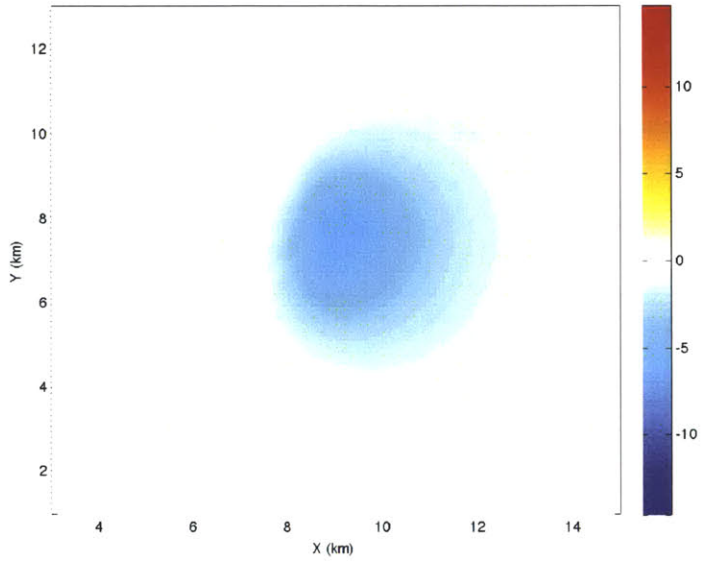

(a) Case 5 (less slip)

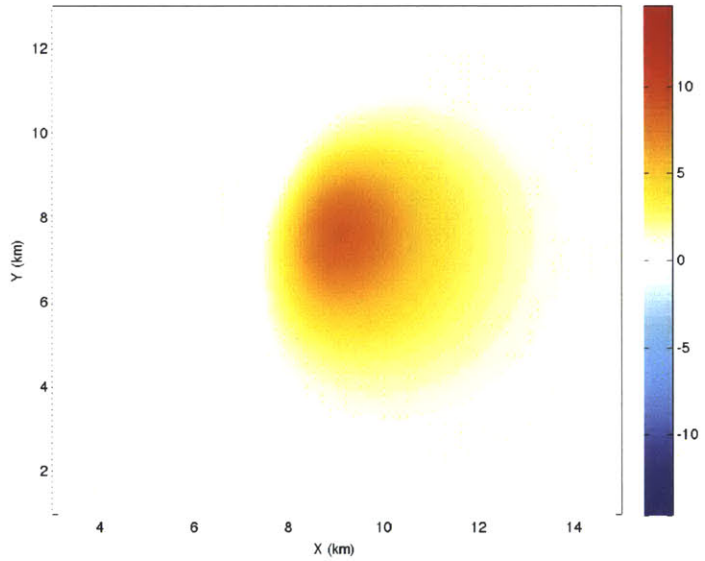

(b) Case 6 (more slip)

Figure 3.26: Normal Fault Slip Error: Difference from Reference Model (mm)

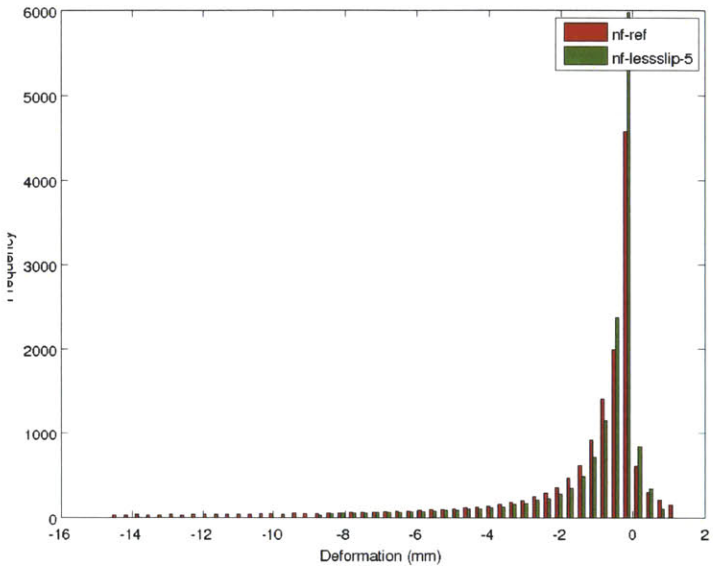

(a) Case 5 (less slip)

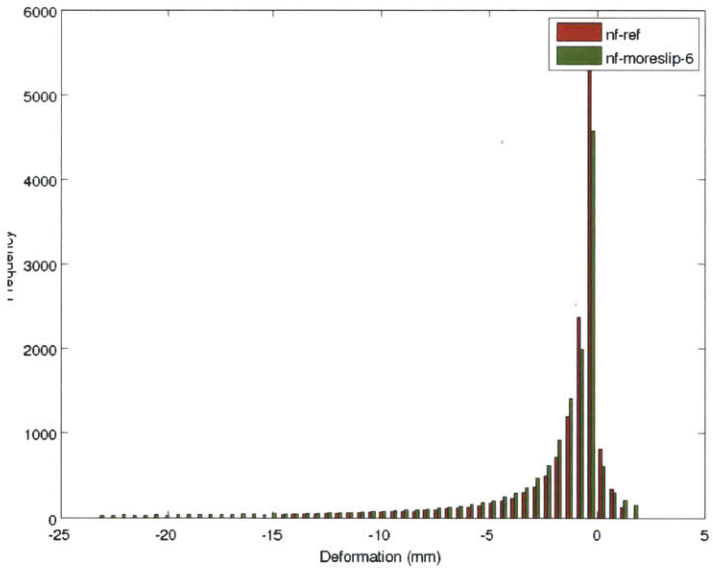

(b) Case 6 (more slip)

Figure 3.27: Normal Fault Slip Error: Histogram of Case vs. Reference Model

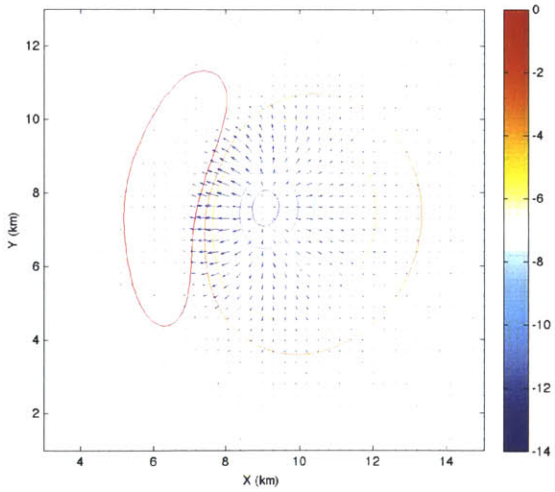

(a) Reference Model

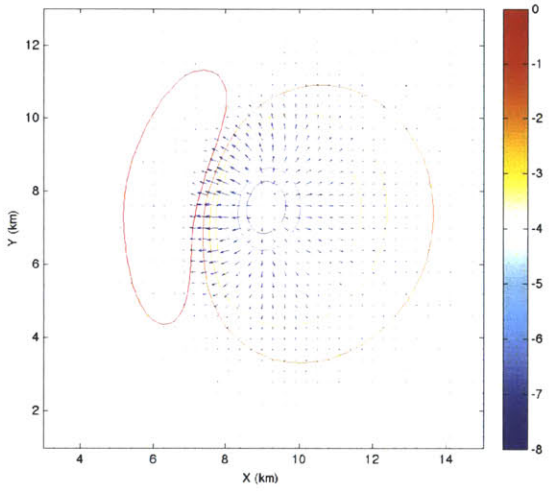

(b) Case 5 (less slip)

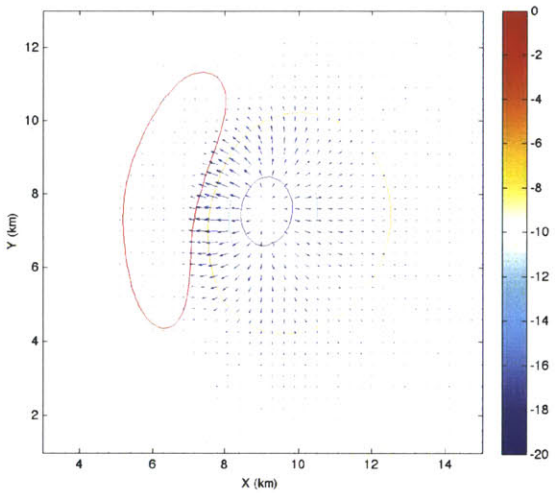

(c) Case 6 (more slip)

Figure 3.28: Normal Fault Slip Error: Gradient Direction Arrows and Magnitude Contours

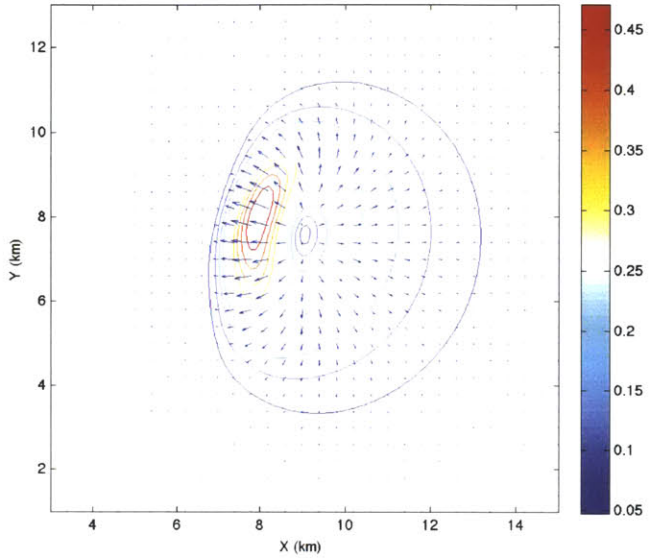

(a) Case 5 (less slip)

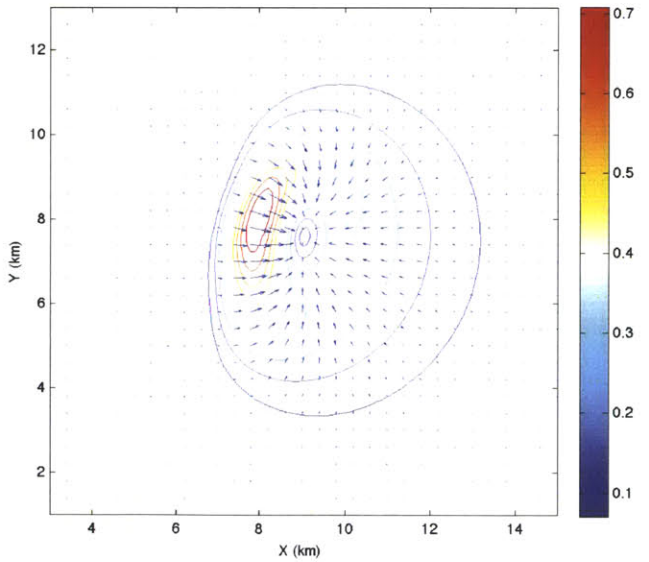

(b) Case 6 (more slip)

Figure 3.29: Normal Fault Slip Error: Vector Gradient Difference Plots

3.2.4 Summary of Normal Fault Errors

The three error types considered for normal faults, fault depth, fault dip and slip distance are difficult to distinguish. Fault depth errors change the lateral extent of deformation significantly and symmetrically; they are primarily a sharp accentuation or broad diminution of the reference model's deformation pattern. Fault dip errors concentrate their deformation changes in the peaks, but moderate errors are very difficult to distinguish in intermediately dipping faults. External data constraints appear to have particular utility for dip errors.

Slip errors are differentiable from depth errors primarily because they influence the deformation peaks rather than the lateral extents of deformation. The somewhat artificial slip errors modeled here are difficult to distinguish from small fault dip errors. More realistic magnitude-preserving fault models that varied slip and fault area together could potentially resolve this ambiguity. Very large errors in fault dip are uniquely identifiable from geodetic models but this constraint is likely a moot point due to the availability of geometric constraints from seismic data. The difficulty of distinguishing between these errors appears to be more related to the intermediate dip of the reference model than the normal faulting regime.

3.3 Thrust Faulting

Thrust faults are low-angle reverse faults that frequently develop within lithologic units when continental plates meet at a convergent boundary. The type example of thrust faulting is the Himalayan orogenic complex. GPS data is currently a more useful geodetic technique than InSAR in these environments because thrust fault movement is predominantly in the X-Y plane.

However, because there is still observable vertical and line-of-sight deformation on thrust faults and 3-D InSAR vector deformation processing techniques are being actively developed, it is appropriate to explore a thrust faulting model suite. Cases 1 and 2 present depth errors, 3 and 4 present small dip errors, while 5 and 6 present slip distance errors.

The fault parameters for all of the cases are summarized in Table 3.5. The faults for the reference case and grid (200m spacing) are shown in Figure 3.30. Table 3.6 summarizes the image statistics for each of the cases. All subsequent models in this section were created by modifying single parameters in the reference model, which is treated as if it were an interferogram collected over a field site.

Table 3.5: Thrust Fault Model Parameters

Case	X start (km)	Y start (km)	X end (km)	Y end (km)	Right-lat Slip (m)	Reverse Slip (m)	Dip (deg)	Fault Top (km)	Fault Bottom (km)
ref	7.5	5.5	7.5	7.5	0	0.05	20	1.5	3.0
ref	7.5	7.5	8.25	9.5	0	0.04	25	1.5	3.5
1	7.5	5.5	7.5	7.5	0	0.05	20	1	2.5
1	7.5	7.5	8.25	9.5	0	0.04	25	1	3.0
2	7.5	5.5	7.5	7.5	0	0.05	20	2	3.5
2	7.5	7.5	8.25	9.5	0	0.04	25	2	4.0
3	7.5	5.5	7.5	7.5	0	0.05	15	1.5	3.0
3	7.5	7.5	8.25	9.5	0	0.04	20	1.5	3.5
4	7.5	5.5	7.5	7.5	0	0.05	25	1.5	3.0
4	7.5	7.5	8.25	9.5	0	0.04	30	1.5	3.5
5	7.5	5.5	7.5	7.5	0	0.08	20	1.5	3.0
5	7.5	7.5	8.25	9.5	0	0.05	25	1.5	3.5
6	7.5	5.5	7.5	7.5	0	0.03	20	1.5	3.0
6	7.5	7.5	8.25	9.5	0	0.02	25	1.5	3.5

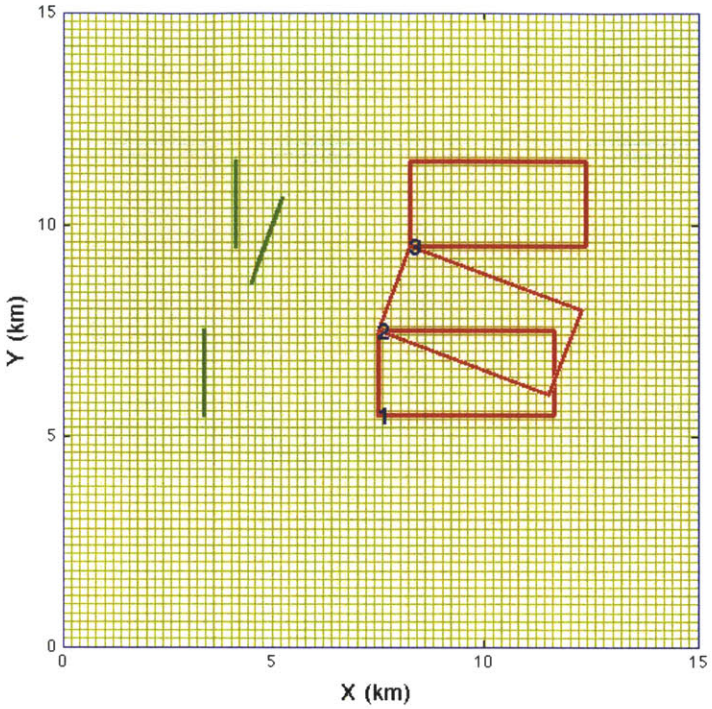

Figure 3.30: Thrust fault reference model and calculation grid

Table 3.6: Thrust Fault Model Statistics

Case	Average Displacement (mm)	Standard Deviation (mm)	Maximum (mm)	Minimum (mm)
Ref	4.7	8.0	35.0	-0.2
1	4.9	9.2	42.5	-0.4
2	4.6	7.0	29.2	-0.2
3	6.1	9.8	39.8	-0.1
4	3.8	6.7	30.5	-0.4
5	7.1	11.9	51.1	-0.3
6	2.7	4.5	19.6	-0.1

3.3.1 Errors in Fault Depth

Errors in fault depth are relatively easy to see from difference maps or from the basic image statistics. Since thrust faults result in uplift, difference maps showing negative values (Case 1) indicate more surface deformation. Histogram plots of the data show the differences nicely, particularly in the extended tail of the shallower fault. Case 1 is 500m shallower and Case 2 is 500m deeper than the reference fault. Figures 3.31 and 3.32 show the deformation and difference maps for the reference model, Case 1 (shallow fault) and Case 2 (deep fault).

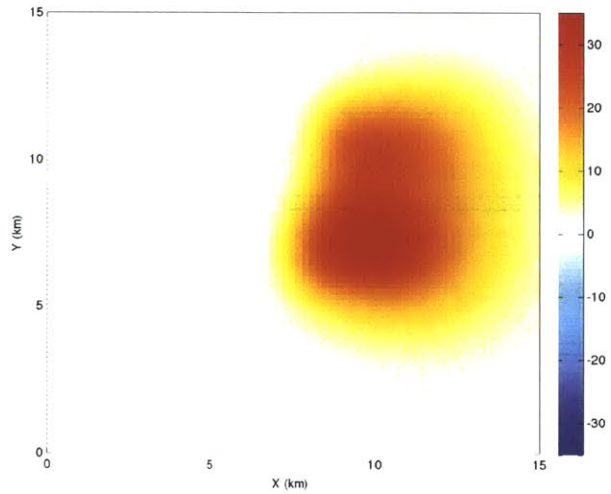

(a) Reference Model

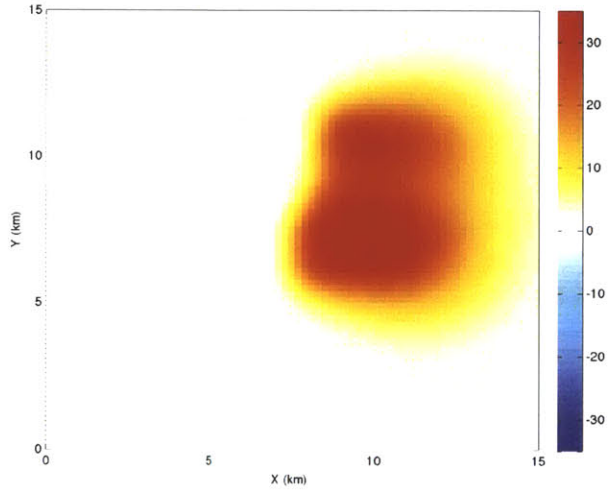

(b) Case 1 (shallow)

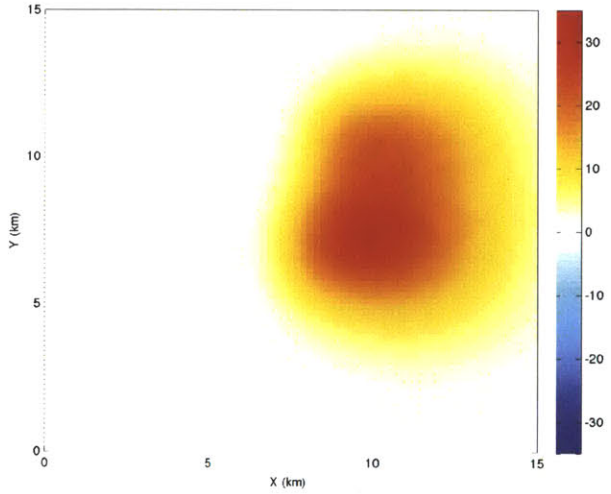

(c) Case 2 (deep)

Figure 3.31: Thrust Fault Depth Error: Vertical Displacements (mm)

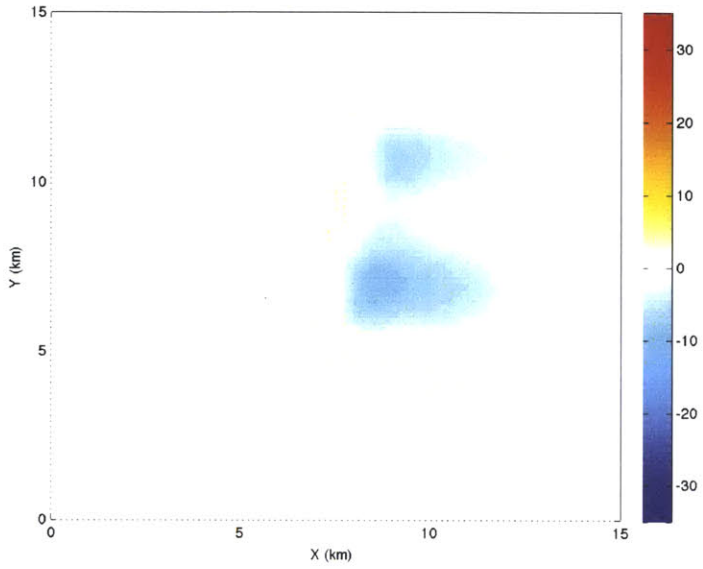

(a) Case 1 (shallow)

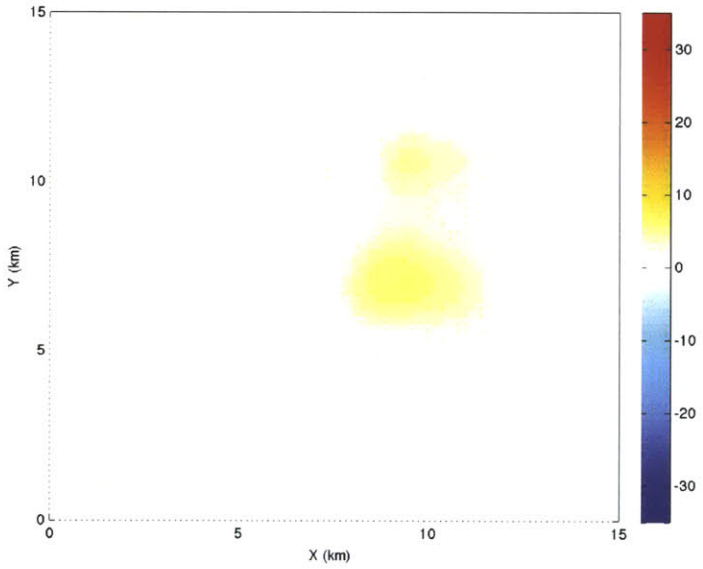

(b) Case 2 (deep)

Figure 3.32: Thrust Fault Depth Error: Difference from Reference Model (mm)

Fault depth is frequently subject to useful constraint by seismic data, but geodetic modelling alone can constrain it given that the other fault geometry parameters are constrained. The low dip angle of the faults in this model moderates the change in lateral extent of vertical surface deformation, but this is still a useful differentiating factor. The three dimensional deformation would be more interesting than vertical deformation for thrust faults. The X and Y difference maps would show much more deformation than the vertical deformation map presented here.

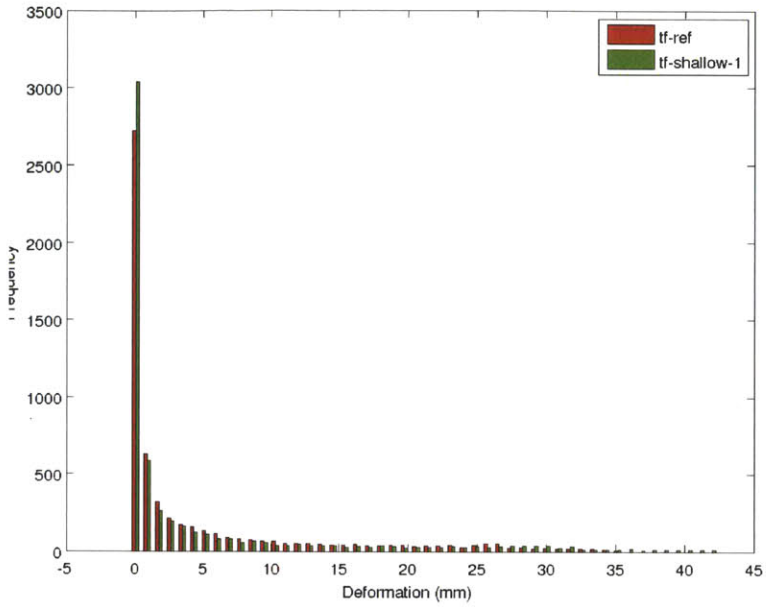

(a) Case 1 (shallow)

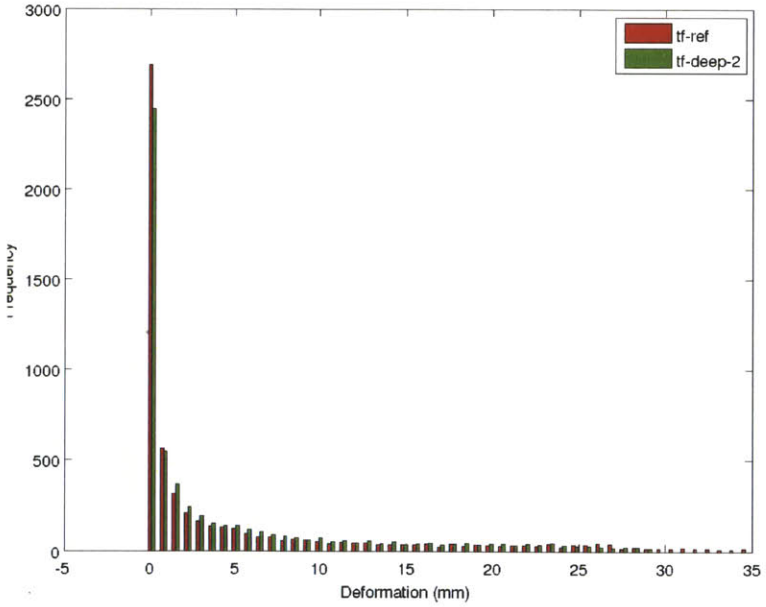

(b) Case 2 (deep)

Figure 3.33: Thrust Fault Depth Error: Histogram of Case vs. Reference Model

3.3.2 Errors in Fault Dip

Fault dip errors are more difficult to constrain than depth or X-Y location errors. Seismic information is a potentially powerful additional tool, but there are some systematic changes in deformation symmetry with varying dip that can identify dip errors. Since thrust faults dip so shallowly, the deformation pattern changes rapidly in both areal extent and magnitude if the dip is in error. Less surface area is deformed by a steeper fault and a broader area is deformed by a shallower fault.

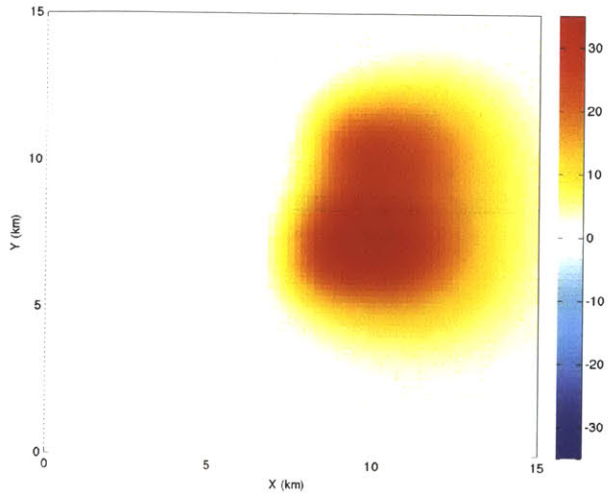

(a) Reference Model

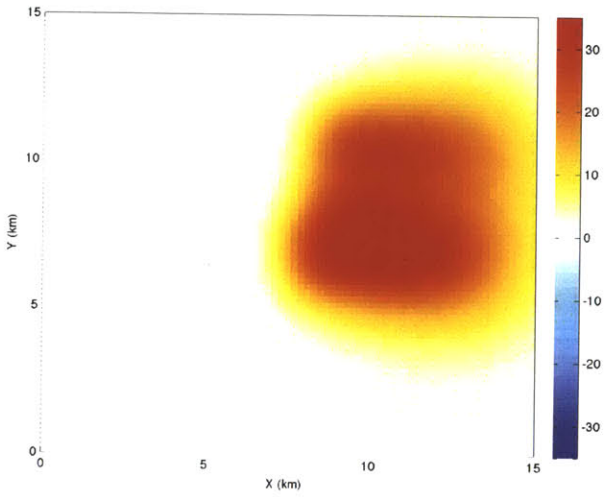

(b) Case 3 (5 deg shallow)

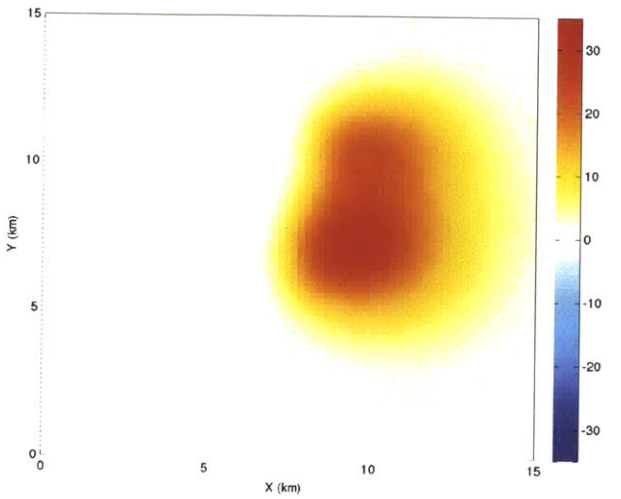

(c) Case 4 (5 deg steep)

Figure 3.34: Thrust Fault Dip Error: Vertical Displacements (mm)

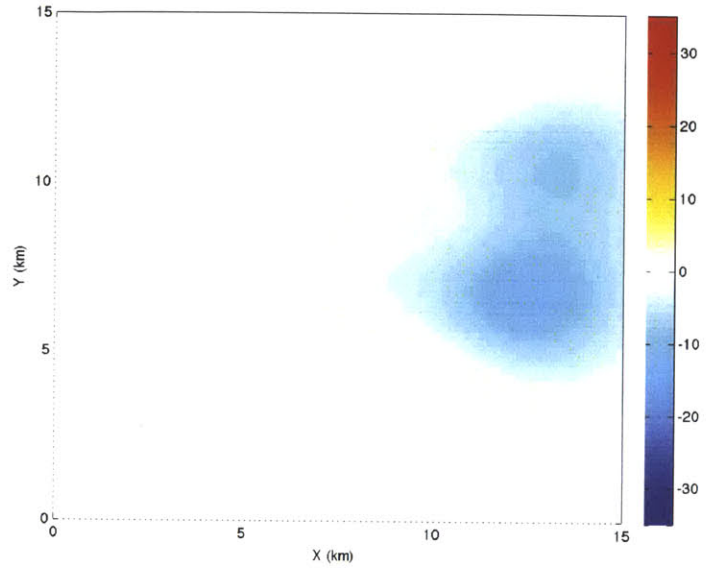

(a) Case 3 (5 deg shallow)

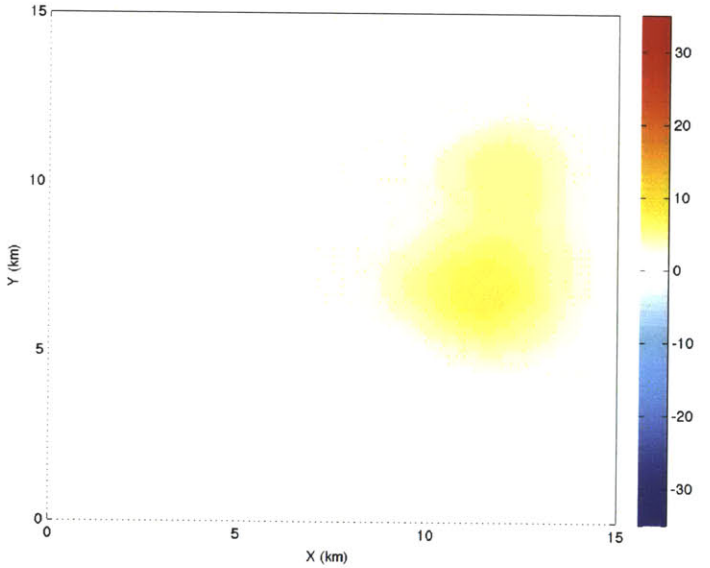

(b) Case 4 (5 deg steep)

Figure 3.35: Thrust Fault Dip Error: Difference from Reference Model (mm)

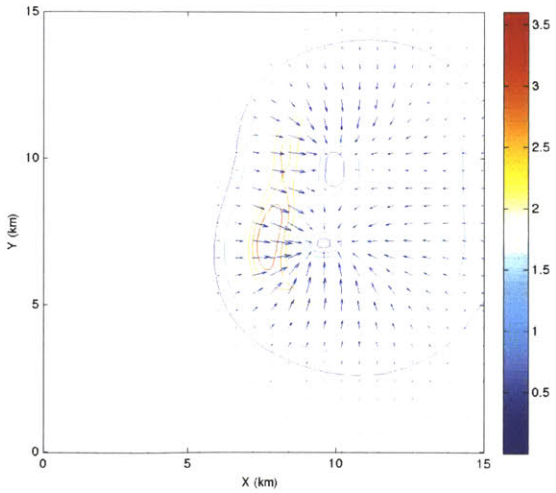

(a) Reference Model

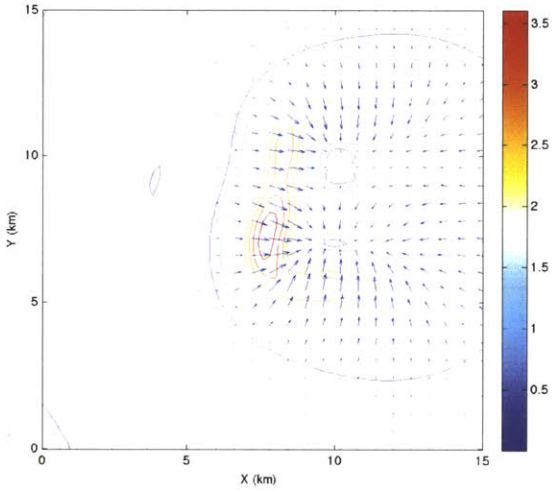

(b) Case 3(5 deg shallow)

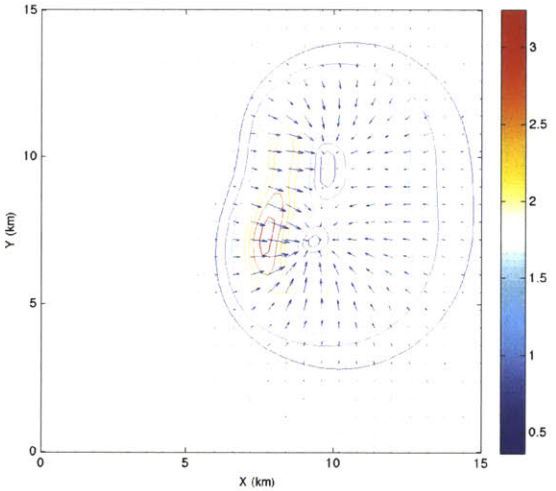

(c) Case 4 (5 deg steep)

Figure 3.36: Thrust Fault Dip Error: Gradient Direction Arrows and Magnitude Contours

The gradient and gradient difference maps, Figures 3.36 and 3.37 allow us to identify the direction of the dip error and are very useful for distinguishing dip errors from slip errors. The deformation gradients are reduced in the steeper model and increased in the shallower model. Sensitivity to dip errors appears to be more strongly a function of the reference fault dip than the magnitude of the error. At extreme dips, such as the vertical strike slip fault and the thrust fault models, sensitivity is high to relatively small dip errors of 5-10 degrees. In contrast, the intermediately-dipping normal fault model showed little sensitivity to errors less than 30 degrees. Horizontal deformation data such as might be available from GPS stations would show dip errors even more clearly.

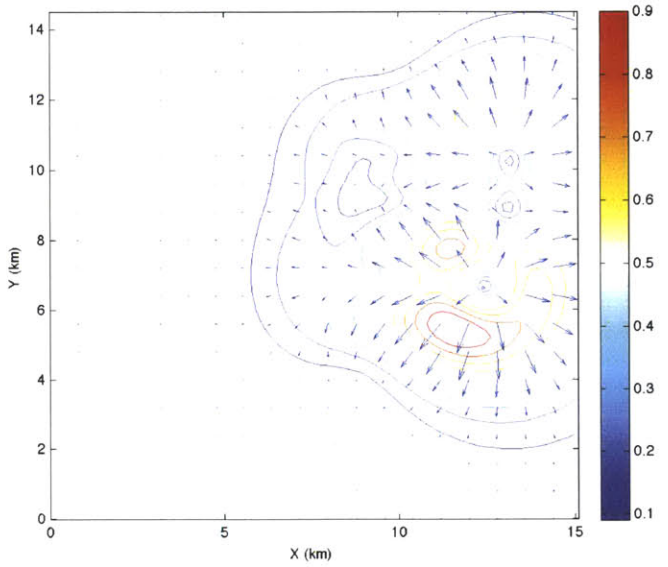

(a) Case 3 (5 deg shallow)

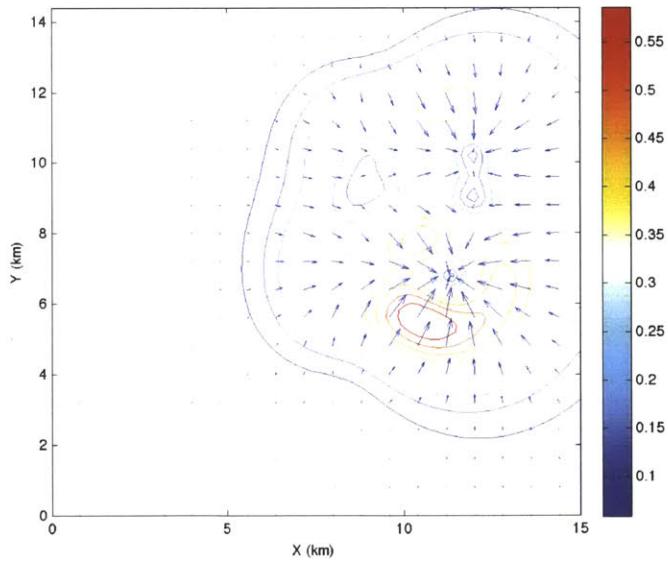

(b) Case 4 (5 deg steep)

Figure 3.37: Thrust Fault Dip Error: Vector Gradient Difference Plots

3.3.3 Errors in Slip Distance

The models in this section are somewhat artificial because they do not preserve earthquake magnitude. They still provide a useful indicator of the effects of slip distance on surface displacement, especially with respect to the lateral extents of deformation. Figure 3.38 shows the surface displacements for the reference model, Case 5 (more slip) and Case 6 (less slip).

Slip errors of this type look superficially similar to depth errors statistically but the increases or decreases in deformation are concentrated in the peak areas instead of spread across the model. The deformation histograms (Figure 3.40) have accordingly longer and shorter tails for more and less slip.

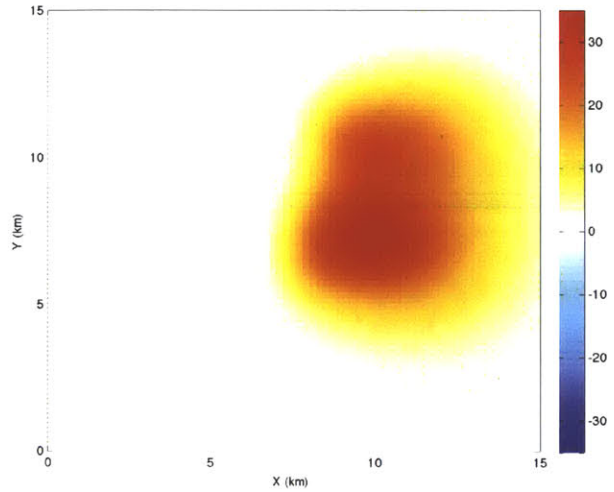

(a) Reference Model

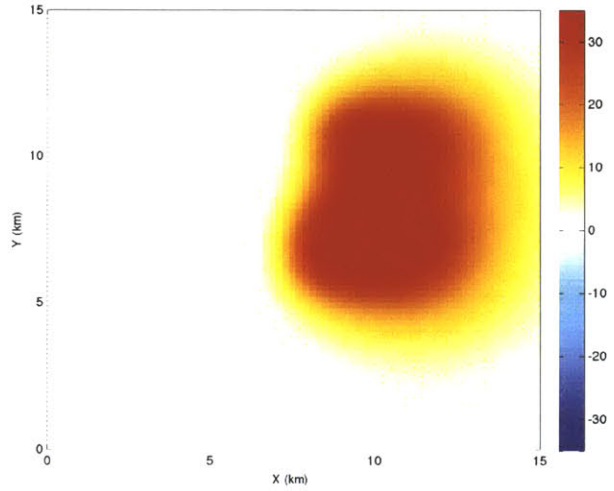

(b) Case 5 (more slip)

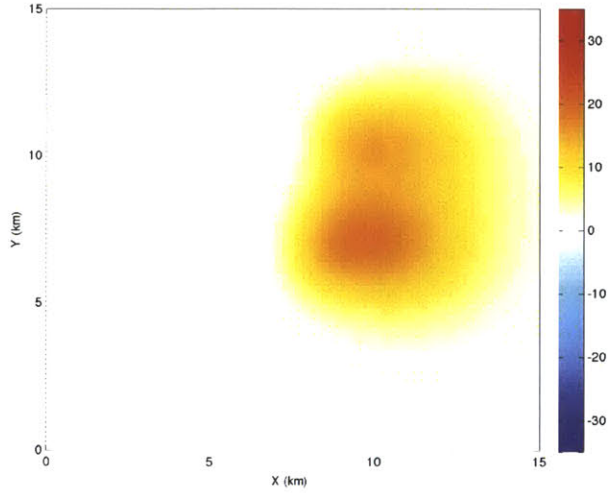

(c) Case 6 (less slip)

Figure 3.38: Thrust Fault Slip Error: Vertical Displacements (mm) (cont.)

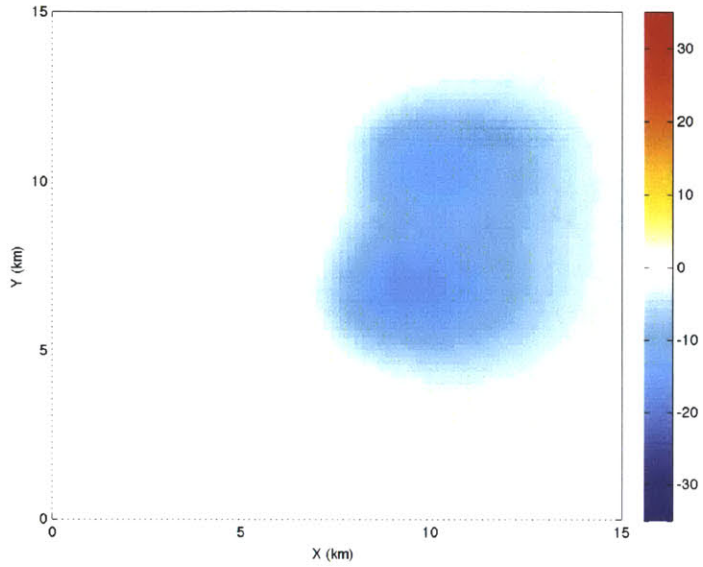

(a) Case 5 (more slip)

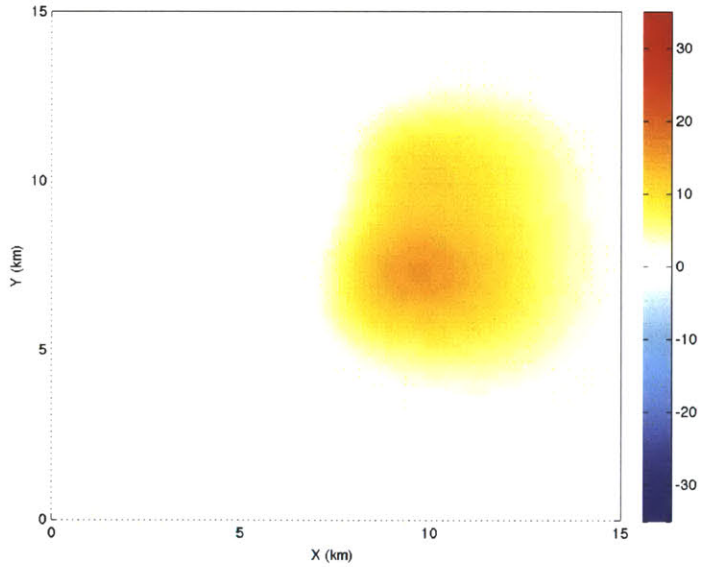

(b) Case 6 (less slip)

Figure 3.39: Thrust Fault Slip Error: Difference from Reference Model (mm)

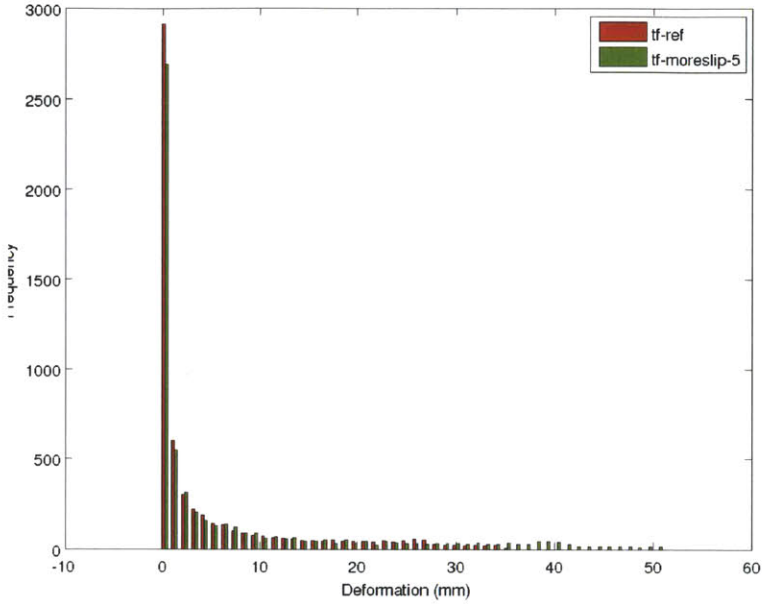

(a) Case 5 (more slip)

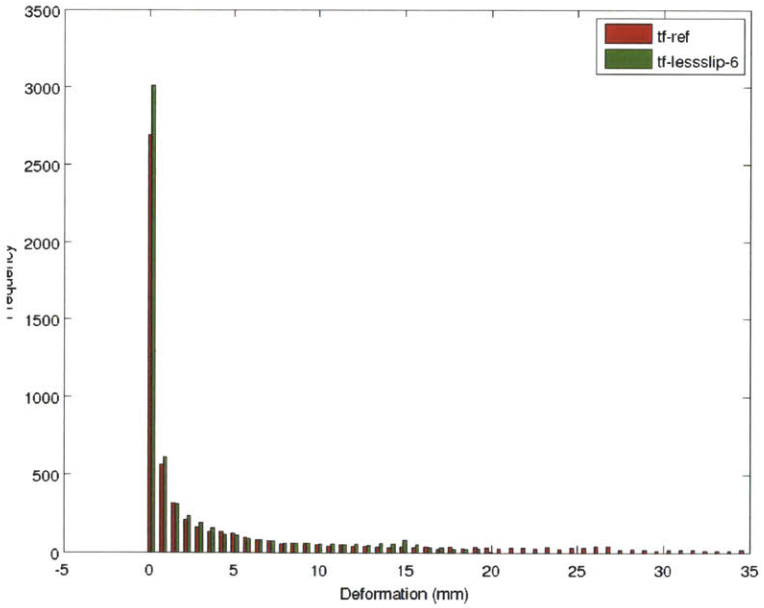

(b) Case 6 (less slip)

Figure 3.40: Thrust Fault Slip Error: Histogram of Case vs. Reference Model

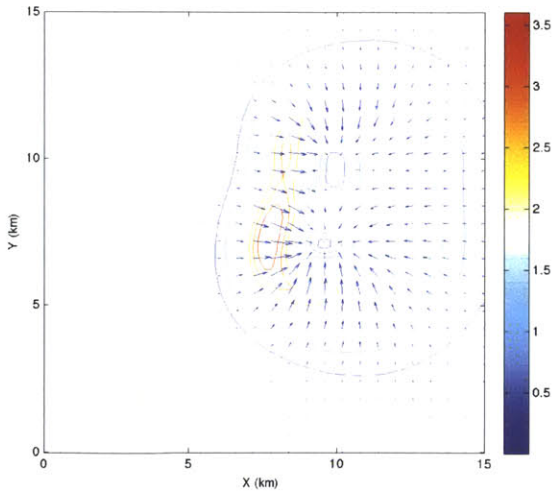

(a) Reference Model

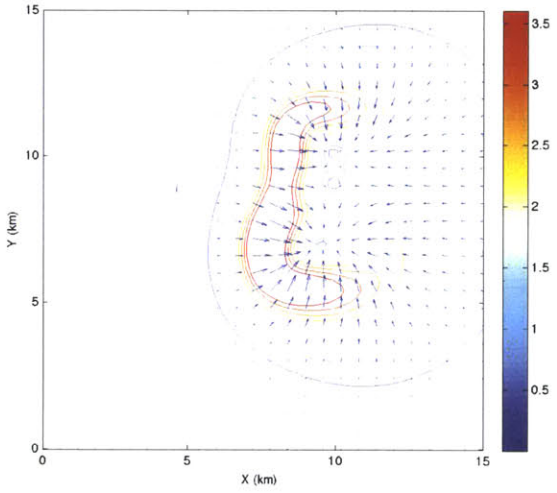

(b) Case 5 (more slip)

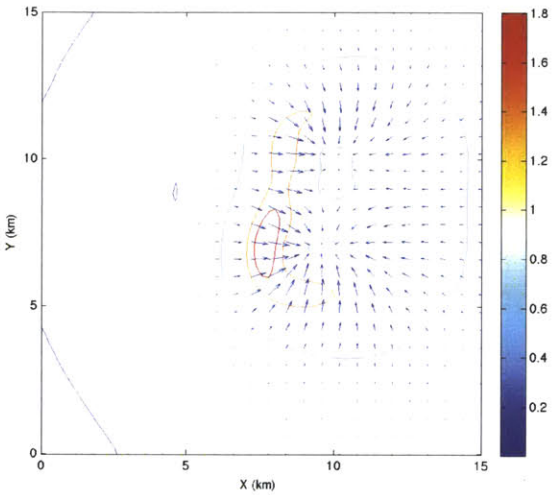

(c) Case 6 (less slip)

Figure 3.41: Thrust Fault Slip Error: Gradient Vector Arrows with Magnitude Contours

The gradient and gradient difference maps (Figures 3.41 and 3.42 are useful for distinguishing between the dip and slip errors. The gradients in the dip error case indicate that the lateral extent of surface deformation has changed significantly. In contrast, the lateral extent of deformation for the slip errors is nearly the same. The magnitude of the two errors is more reflective of the larger parameter changes applied to the slip than of a distinguishing characteristic. The average, standard deviation and maximum values increase for both error types, so the basic image statistics are of little distinguishing value. The three dimensional deformation picture for thrust faults is much more informative and would offer new ways to distinguish between depth and slip errors in particular.

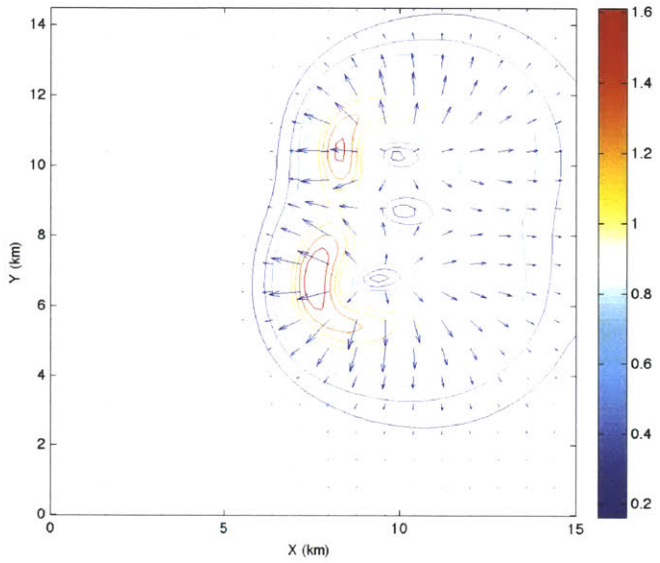

(a) Case 5 (more slip)

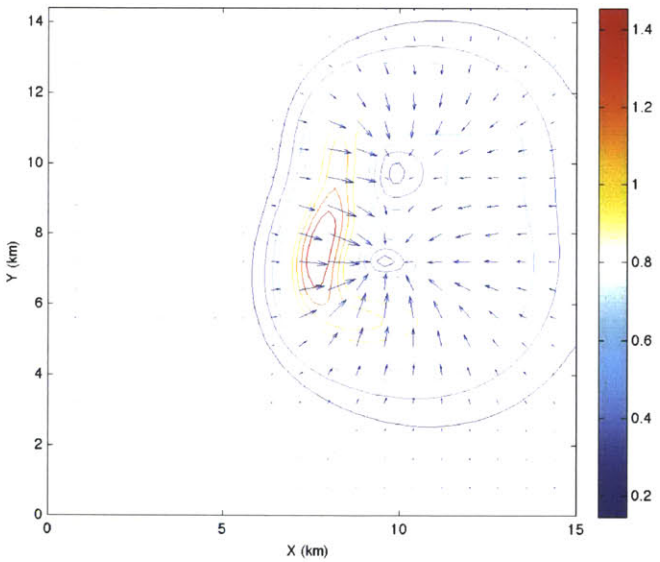

(b) Case 6 (less slip)

Figure 3.42: Thrust Fault Slip Error: Vector Gradient Difference Plots

3.3.4 Summary of Thrust Faulting Errors

Depth and slip errors are difficult to distinguish for thrust faults. Slip errors as modelled here do not preserve earthquake moment and because the faults dip so shallowly they are difficult to distinguish from depth errors. In contrast, the very low dip of thrust faults makes the surface deformation much more sensitive to dip errors than for intermediately dipping faults, so variation in the lateral extent of deformation can distinguish even small dip errors.

Slip errors modelled in a magnitude-preserving way by varying the fault rupture area and the slip distance simultaneously might be more readily distinguished because the shape and extent of the surface deformation would vary much more. However, varying multiple parameters simultaneously raises a different set of challenges. The average and maximum values move together for all three error types, but useful clues can be extracted from the shapes and lengths of the histogram tails as compared to the reference histogram. Lateral surface deformation data would be especially useful in distinguishing between depth and slip errors for thrust faults.

3.4 Reservoir-type faulting: Intersecting Normal Faults and an Inflationary Point Source

Coulomb 3.2 can create models of nearly arbitrary structural complexity, within the bounds of a homogeneous half-space earth model. A reservoir-type reference model located in an extensional tectonic environment is examined a simple normal fault pair and a moderate amount of isotropic point source inflation, such as might be observed at an injection well. Reservoirs can also have reverse or strike-slip faulting regimes. Normal fault activation will be most common in extensional tectonic environments or when high-pressure injection results in tensile crack opening.

The fault parameters for all of the cases are summarized in Table 3.7. The "slip" for the point source is listed under the reverse slip column but is a dilatation in m^3. The fault and point source geometry is shown with the 100m cell calculation grid in Figure 3.43. The image statistics are summarized in Table 3.8. Case 1 shows the effect of removing the point source completely, while Case 2 has a far-too-large point source. Cases 3 and 4 present depth errors for shallow and deep faults respectively. Cases 5 and 6 have too little and too much slip on faults geometrically identical to the reference model. Cases 7 and 8 have dip errors where the faults dip at 10 degrees shallower and steeper than the reference model. All subsequent

models in this section were created by modifying single parameters in the reference model, which is treated as if it were an interferogram collected over a field site.

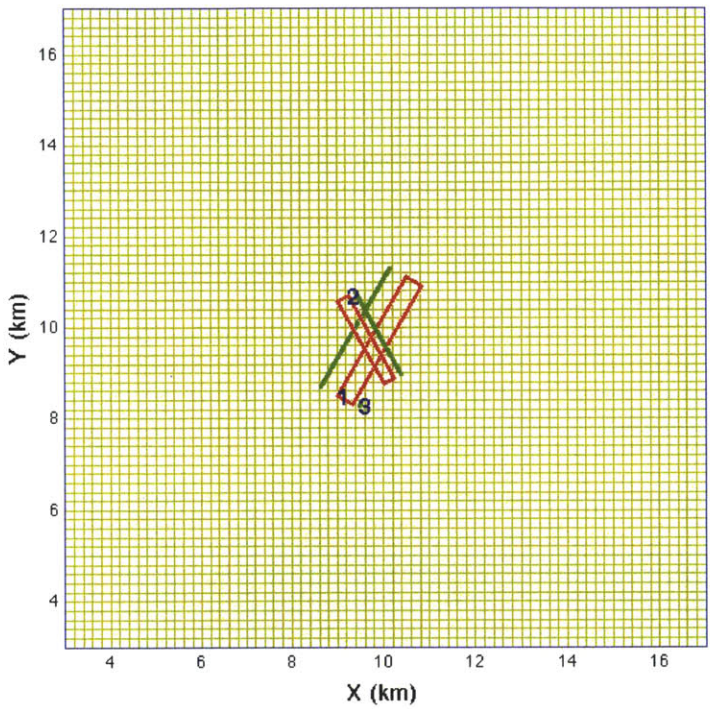

Figure 3.43: Reservoir-type model with faults (1,2), point source (3) and calculation grid

Table 3.7: Reservoir Faulting Model Parameters

Case	X start (km)	Y start (km)	X end (km)	Y end (km)	Right-lat Slip (m)	Reverse Slip (m)	Dip (deg)	Fault Top (km)	Fault Bottom (km)
ref	9.0	8.5	10.5	11.1	0	-0.05	75	1.5	3.0
ref	9.25	10.7	10.25	8.9	0	-0.03	80	1.0	2.5
ref-pt	9.49	8.29	9.51	8.31	0	$1x10^8$	89.9	1.99	2.01
1	9.0	8.5	10.5	11.1	0	-0.05	75	1.5	3.0
1	9.25	10.7	10.25	8.9	0	-0.03	80	1.0	2.5
2	9.0	8.5	10.5	11.1	0	-0.05	75	1.5	3.0
2	9.25	10.7	10.25	8.9	0	-0.03	80	1.0	2.5
2-pt	9.49	8.29	9.51	8.31	0	$5x10^8$	89.9	1.99	2.10
3	9.0	8.5	10.5	11.1	0	-0.05	75	1.0	3.0
3	9.25	10.7	10.25	8.9	0	-0.03	80	0.5	2.0
3-pt	9.49	8.29	9.51	8.31	0	$1x10^8$	89.9	1.49	1.51
4	9.0	8.5	10.5	11.1	0	-0.05	75	2.0	4.0
4	9.25	10.7	10.25	8.9	0	-0.03	80	1.5	3.0
4-pt	9.49	8.29	9.51	8.31	0	$1x10^8$	89.9	2.49	2.51
5	9.0	8.5	10.5	11.1	0	-0.03	75	1.5	3.0
5	9.25	10.7	10.25	8.9	0	-0.02	80	1.0	2.5
5-pt	9.49	8.29	9.51	8.31	0	$1x10^8$	89.9	1.99	2.01
6	9.0	8.5	10.5	11.1	0	-0.08	75	1.5	3.0
6	9.25	10.7	10.25	8.9	0	-0.05	80	1.0	2.5
6-pt	9.49	8.29	9.51	8.31	0	$1x10^8$	89.9	1.99	2.01
7	9.0	8.5	10.5	11.1	0	-0.05	65	1.5	3.0
7	9.25	10.7	10.25	8.9	0	-0.03	70	1.0	2.5
7-pt	9.49	8.29	9.51	8.31	0	$1x10^8$	89.9	1.99	2.01
8	9.0	8.5	10.5	11.1	0	-0.05	85	1.5	3.0
8	9.25	10.7	10.25	8.9	0	-0.03	90	1.0	2.5
8-pt	9.49	8.29	9.51	8.31	0	$1x10^8$	89.9	1.99	2.01

Table 3.8: Reservoir Faulting Model Statistics

Case	Average Displacement (mm)	Standard Deviation (mm)	Maximum (mm)	Minimum (mm)
Ref	-0.57	0.75	2.95	-4.54
1	-0.76	0.87	2.20	-5.15
2	0.17	1.23	7.42	-2.68
3	-0.82	1.17	4.62	-7.99
4	-0.60	0.72	2.25	-3.61
5	-0.29	0.44	2.13	-2.56
6	-1.04	1.26	4.33	-7.67
7	-0.71	1.04	2.28	-6.25
8	-0.51	0.64	3.38	-3.51

3.4.1 Point Source Errors

The first two cases present errors in the homogeneous point source. The point source inflation modelled here is somewhat unrealistic because it does not account for heterogeneous fluid migration as a coupled hydromechanical Finite Element solver could, but it serves as a useful first order simplification. Figure 3.44 shows the deformation at the surface for Cases 1 and 2, while Figure 3.45 shows their differences from the reference model.

Point source errors of this simplified type are very easy to identify because they yield perfect error circles on the difference maps. The X-Y location of a point source should be known from well data, as should a reasonable approximation of the injected volume. The hydrogeology of the subsurface is always difficult to parameterize. Half-space earth models are clearly not the correct avenue to address questions about how the fluid will migrate and the effects that might have on surface deformation. In a real-world modelling situation point source errors would likely be harder to identify because they could be hidden by other less geometrically evident errors.

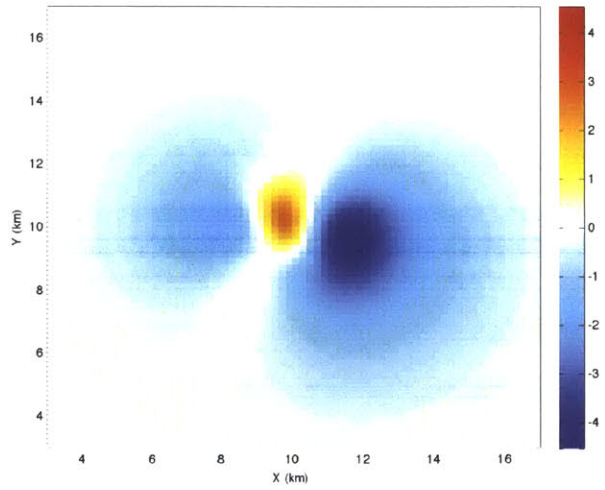

(a) Reference Model

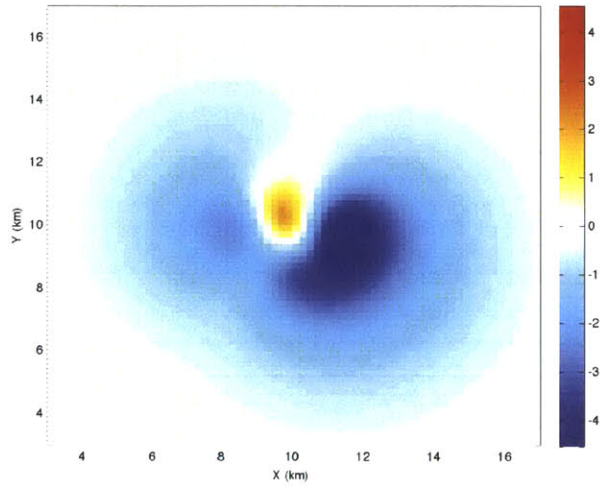

(b) Case 1 (no point source)

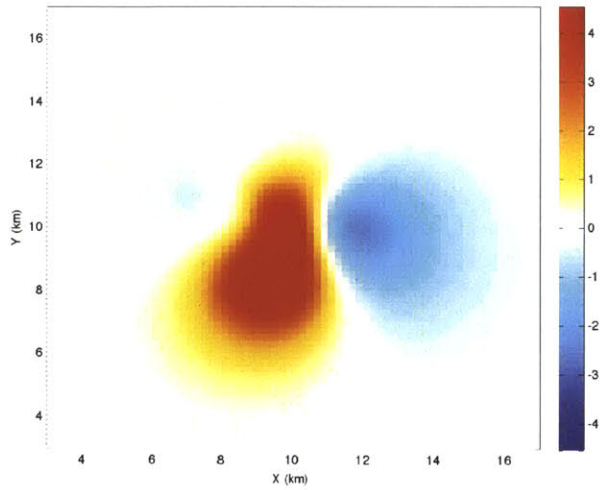

(c) Case 2 (large point source)

Figure 3.44: Reservoir Faulting Point Source Error: Vertical Displacements (mm)

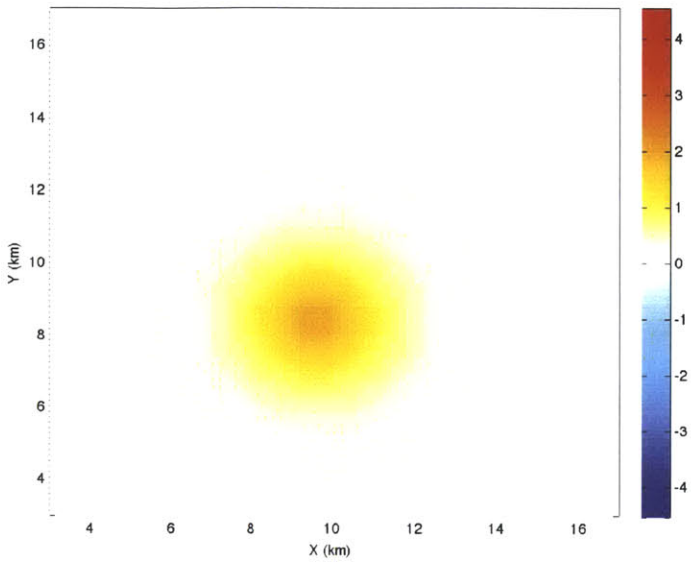

(a) Case 1 (no point source)

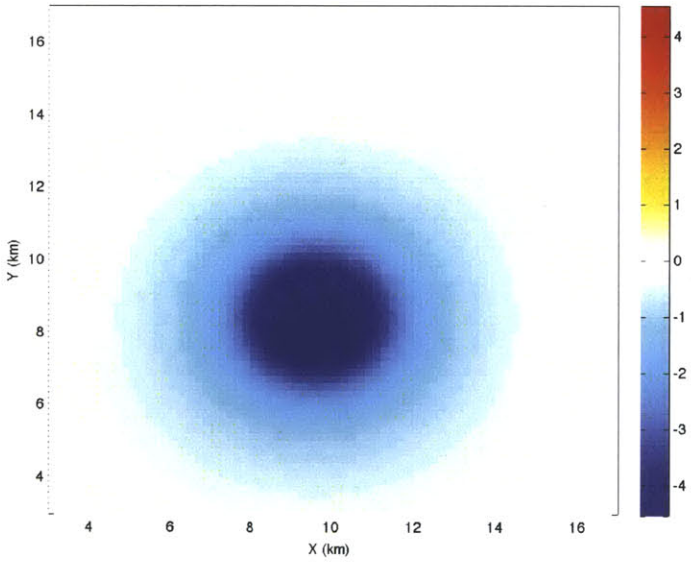

(b) Case 2 (large point source)

Figure 3.45: Reservoir Faulting Point Source Error: Difference from Reference Model (mm)

3.4.2 Errors in Fault Depth

The images in Figures 3.46 and 3.47 show the deformation and difference maps for Cases 3 and 4, shallower and deeper than the reference model respectively. Errors in fault and point source depth are relatively obvious on difference maps or from the basic image statistics. The shallower fault has greater peak deformation and a smaller lateral extent of deformation compared to the broader, muted deformation of the deep faults.

Histogram plots of the data (Figure 3.48 show the differences nicely, with Case 3 having a longer deformation tail and Case 4 more more cells with low levels of deformation but a shorter tail. Case 3 is 500m shallower and Case 4 is 500m deeper than the reference faults and point source. Fault depth and geometry are frequently subject to accurate seismic constraints in reservoir settings, which can be of great use for distinguishing between error types in geomechanical models.

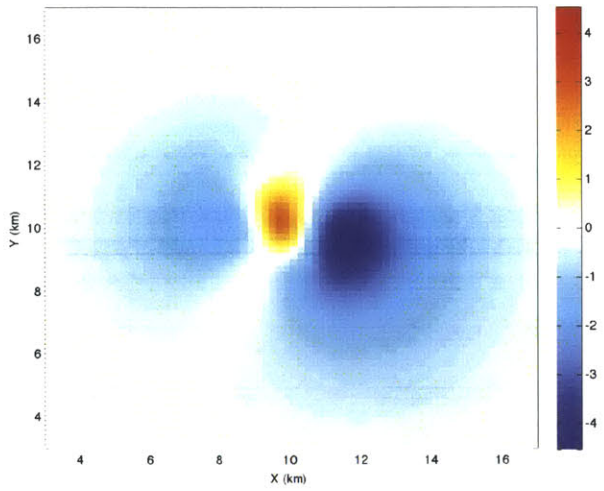

(a) Reference Model

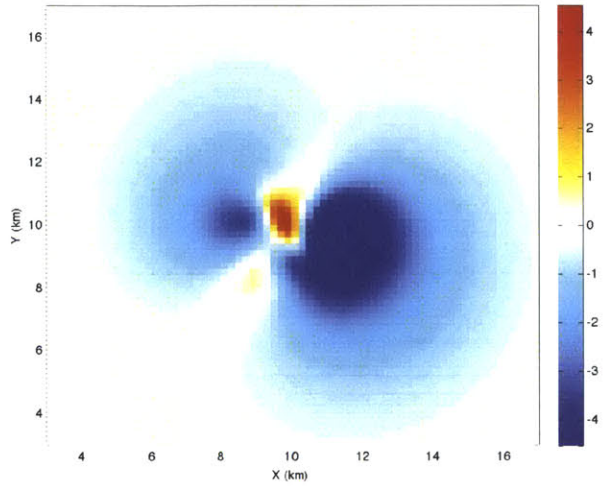

(b) Case 3 (shallow)

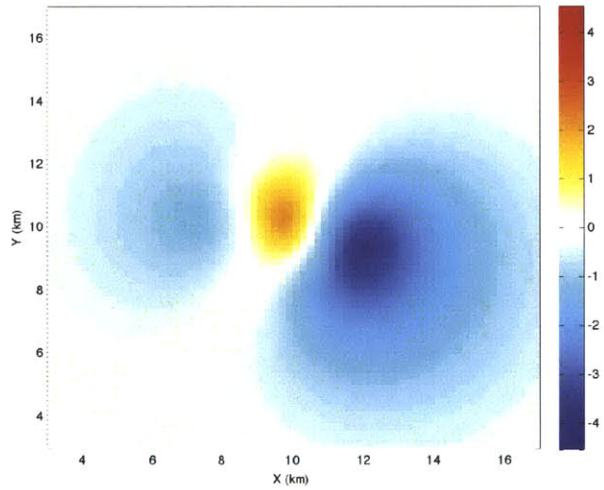

(c) Case 4 (deep)

Figure 3.46: Reservoir Faulting Point Source Error: Vertical Displacements (mm)

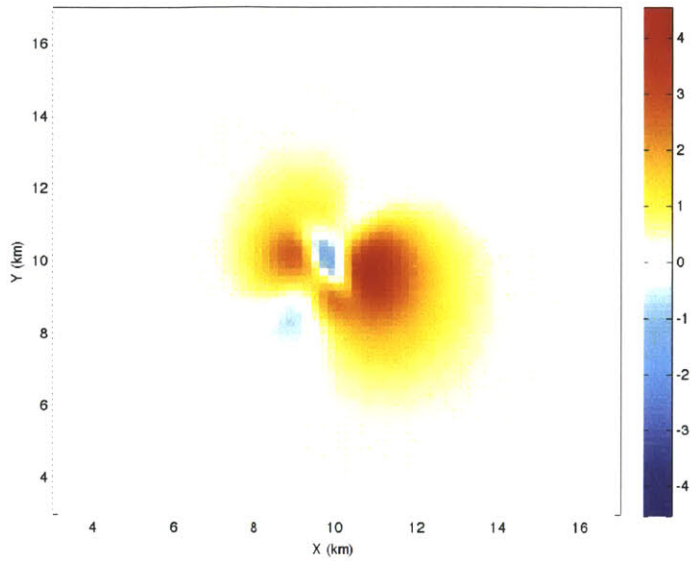

(a) Case 3 (shallow)

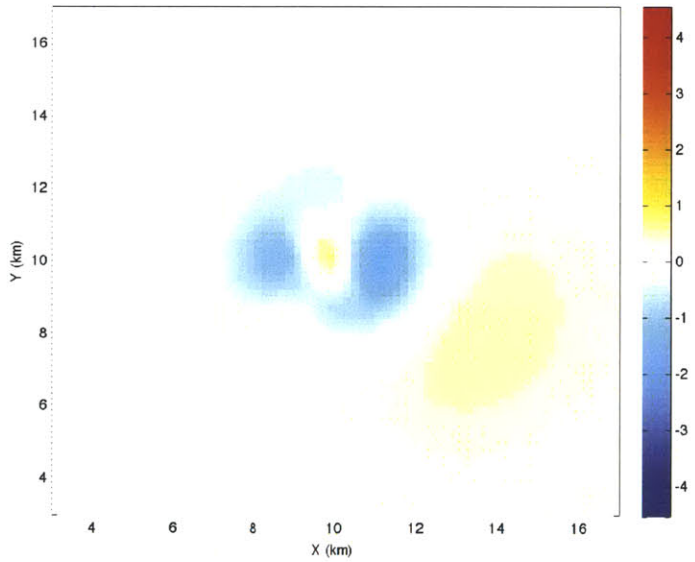

(b) Case 4 (deep)

Figure 3.47: Reservoir Faulting Point Source Error: Difference from Reference Model (mm)

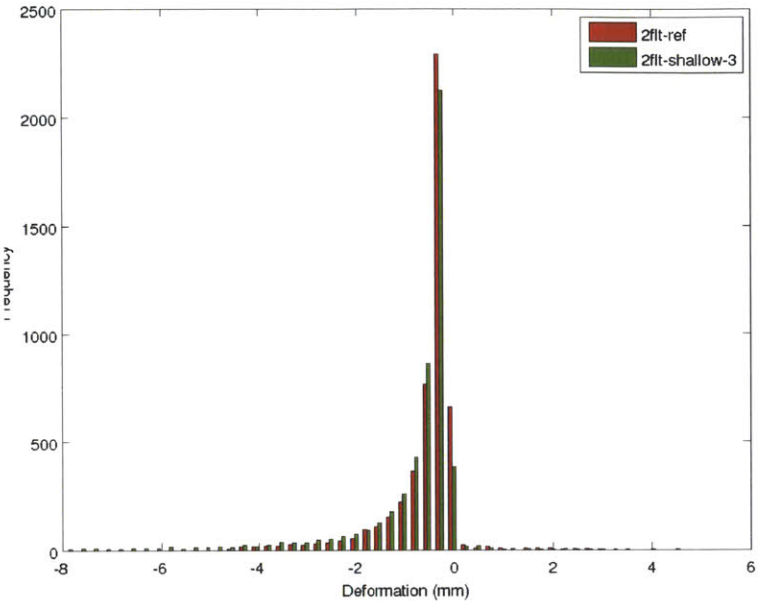

(a) Case 3 (shallow)

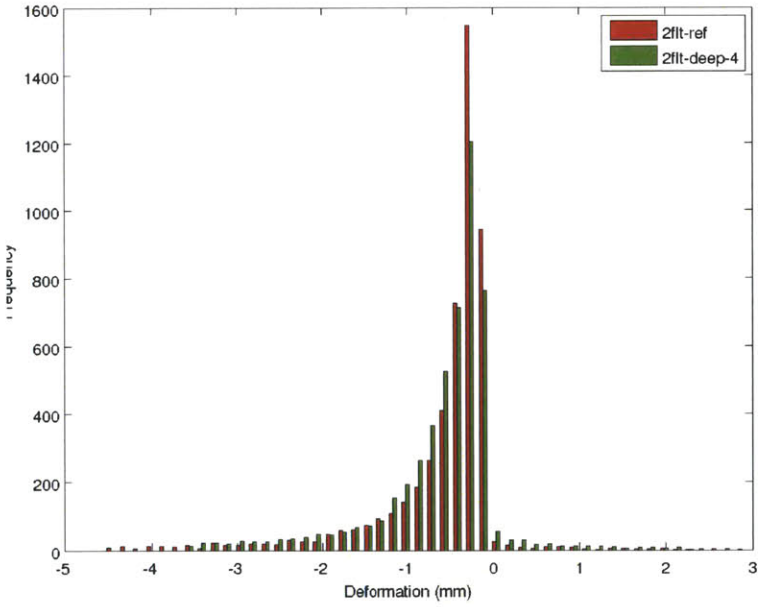

(b) Case 4 (deep)

Figure 3.48: Reservoir Faulting Point Source Error: Histogram of Case vs. Reference Model

3.4.3 Errors in Slip Distance

Slip errors look superficially similar to depth errors statistically and on the plots. However, the increases or decreases in deformation are concentrated at the peak areas instead of spread across the entire model. The difference maps (Figure 3.50) look very similar to the original deformation map, compared with the broad lateral changes evident in the depth error cases.

The gradient and gradient difference maps (Figures 3.52 and 3.53 confirm these conclusions: changing the slip distance on steeply dipping faults accentuates or diminishes the pattern symmetrically with respect to the reference model. A more detailed magnitude-preserving treatment of slip errors would yield different results because the fault area would change as well as the slip. The maximum and minimum changes from the reference model would be diminished and the area affected would broaden or tighten with larger or smaller faults, similar to depth errors.

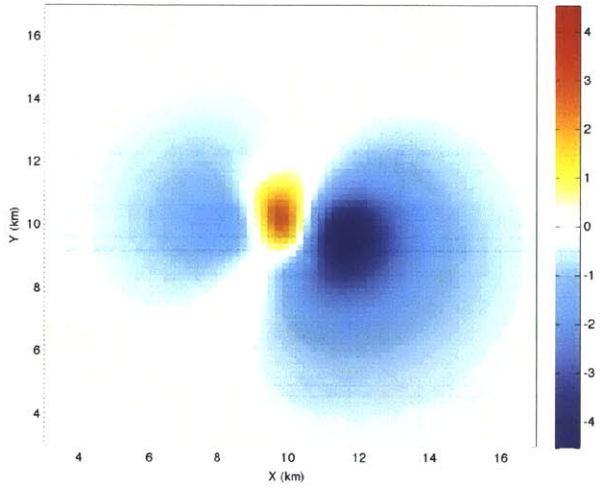

(a) Reference Model

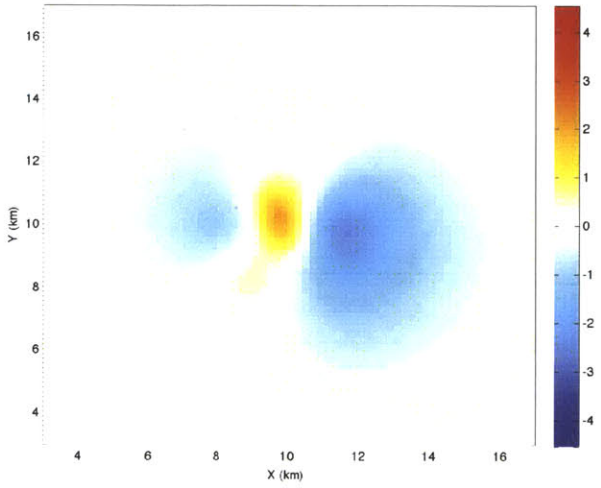

(b) Case 5 (less slip)

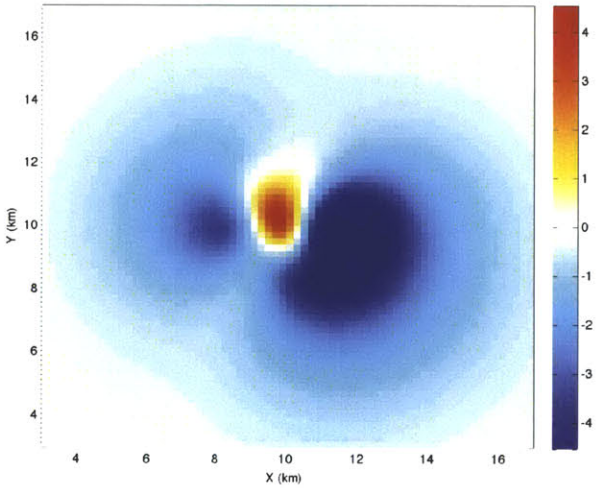

(c) Case 6 (more slip)

Figure 3.49: Reservoir Faulting Slip Error: Vertical Displacements (mm) (cont.)

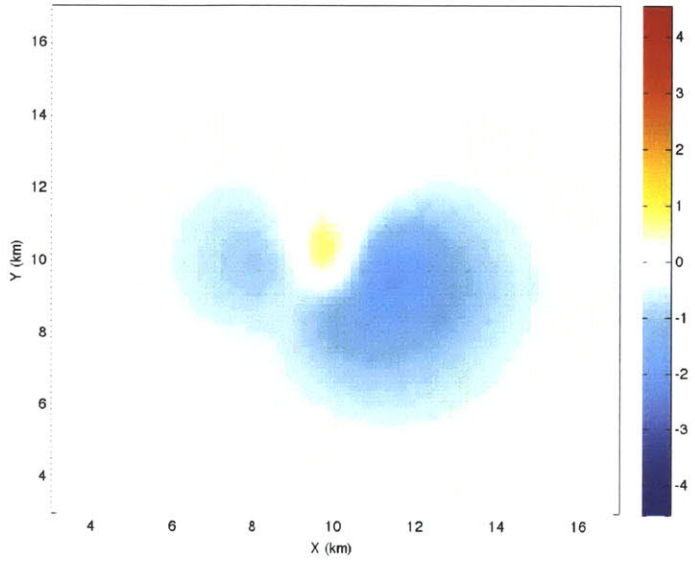

(a) Case 5 (less slip)

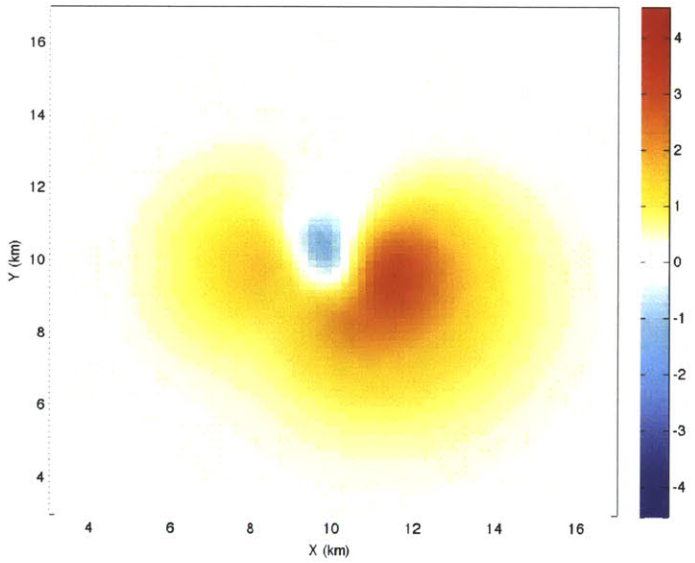

(b) Case 6 (more slip)

Figure 3.50: Reservoir Faulting Slip Error: Difference from Reference Model (mm)

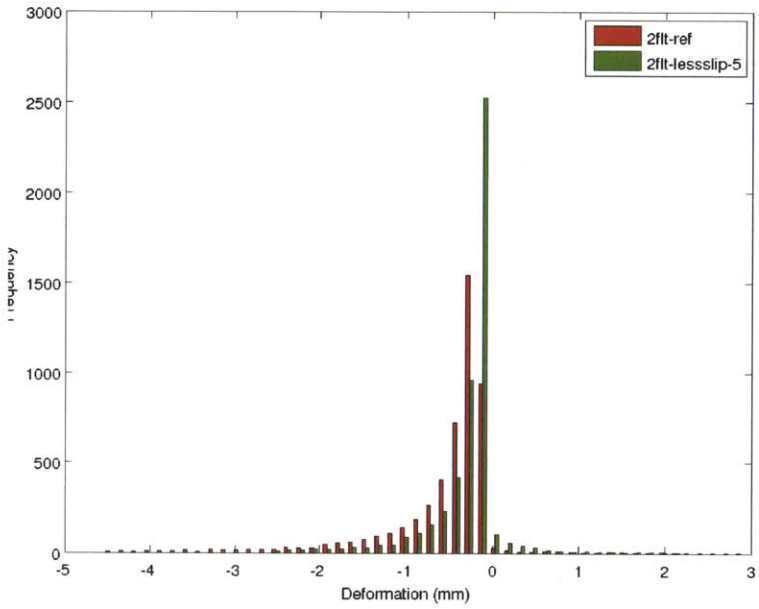

(a) Case 5 (less slip)

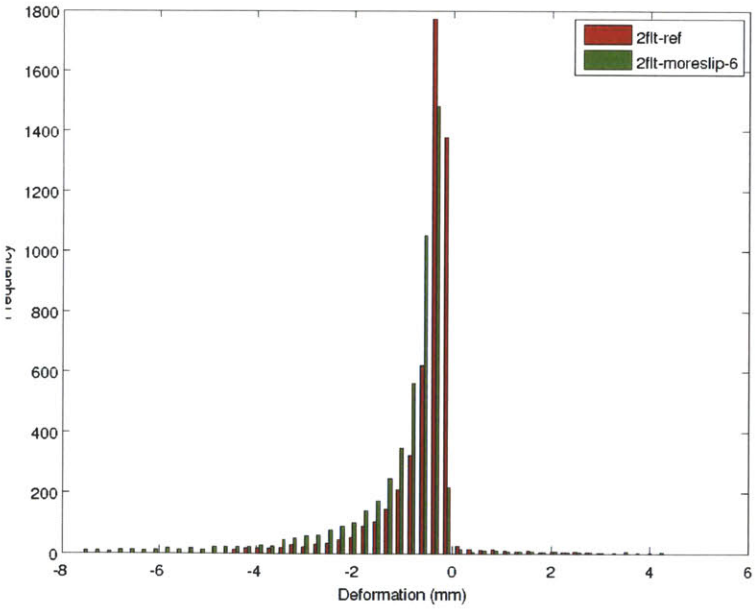

(b) Case 6 (more slip)

Figure 3.51: Reservoir Faulting Slip Error: Histogram of Case vs. Reference Model

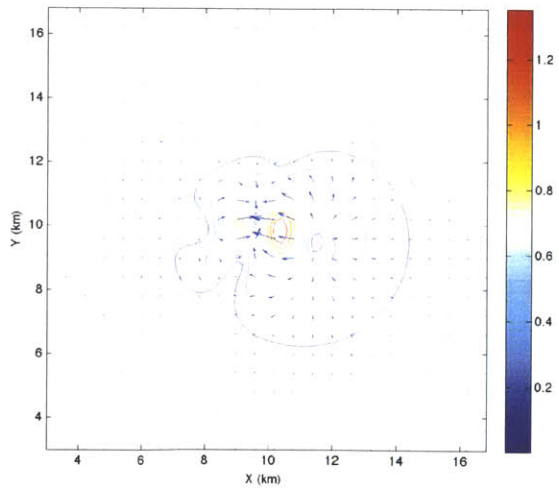

(a) Reference Model

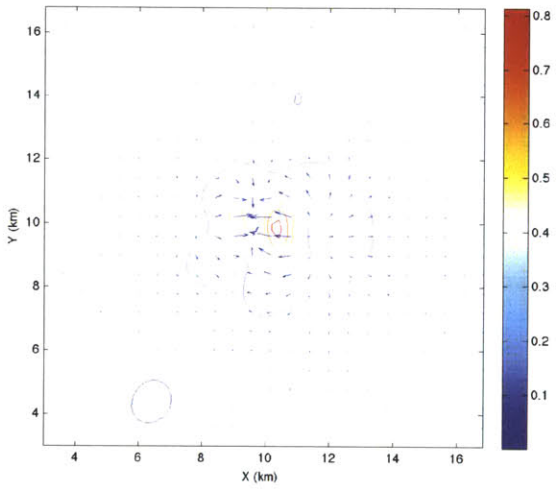

(b) Case 5 (less slip)

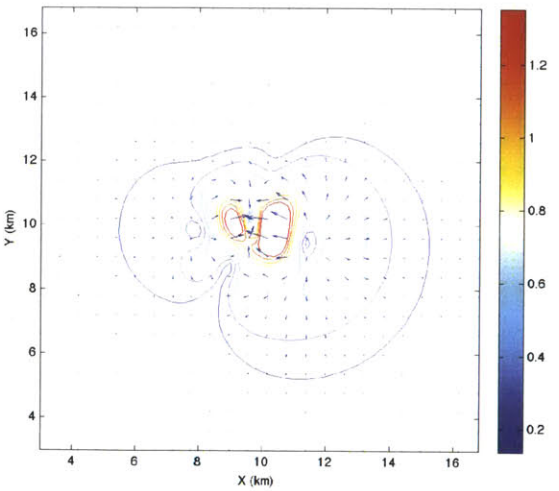

(c) Case 6 (more slip)

Figure 3.52: Reservoir Faulting Slip Error: Gradient Direction Arrows and Magnitude Contours

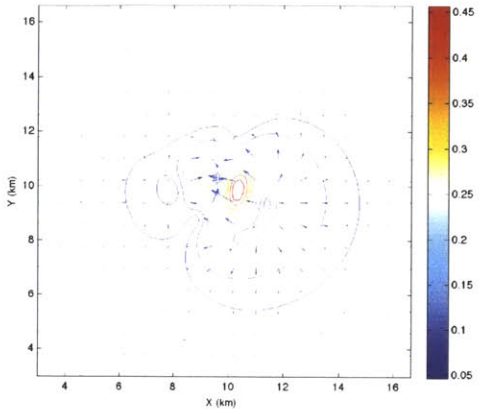

(a) Case 5 (less slip)

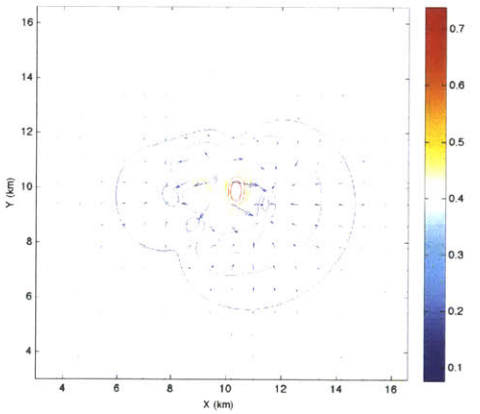

(b) Case 6 (more slip)

Figure 3.53: Reservoir Faulting Slip Error: Vector Gradient Difference Plots

3.4.4 Errors in Fault Dip

Fault dip errors are more difficult to constrain than depth or X-Y location errors, especially for movement on faults with shallow or intermediate dip. Seismic information is a potentially powerful additional tool in a reservoir setting, but there are some systematic changes in surface deformation symmetry with varying dip that can identify dip errors. Dip errors are challenging to detect for intermediately-dipping faults because the asymmetries generated are somewhat more subtle and easily confused for depth errors.

The faults in the reference model for this model suite dip quite steeply (75 and 80 degrees), so the increasing deformation asymmetry is observable with the 10 degree errors in Cases 7 and 8 (Figure 3.54). The difference maps are shown in Figure 3.55. For intermediately- or shallowly-dipping faults the difference maps are less clear and gradient maps are needed as in the normal fault model suite (Section 3.2).

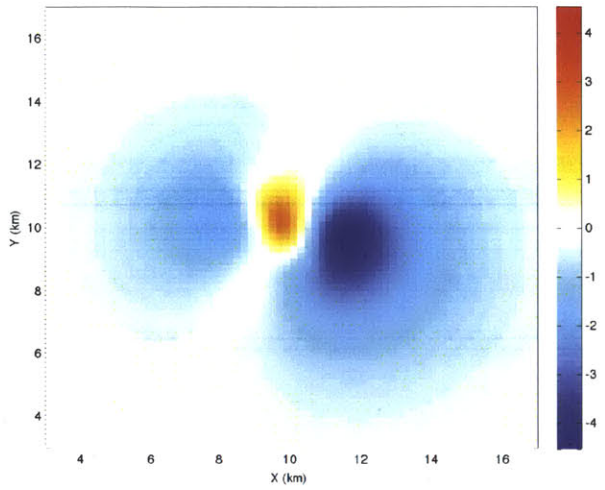

(a) Reference Model

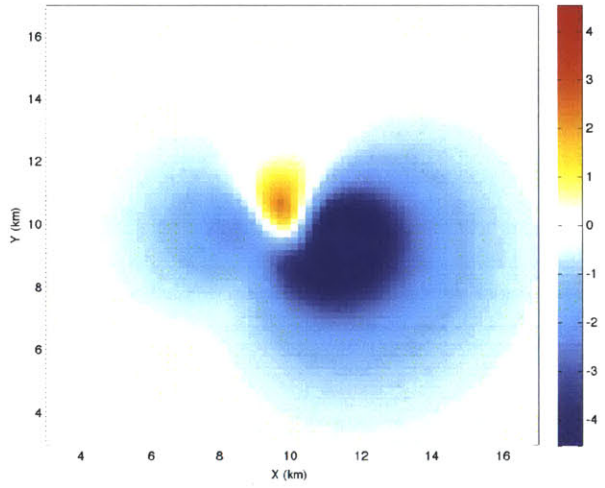

(b) Case 7 (10 deg shallow)

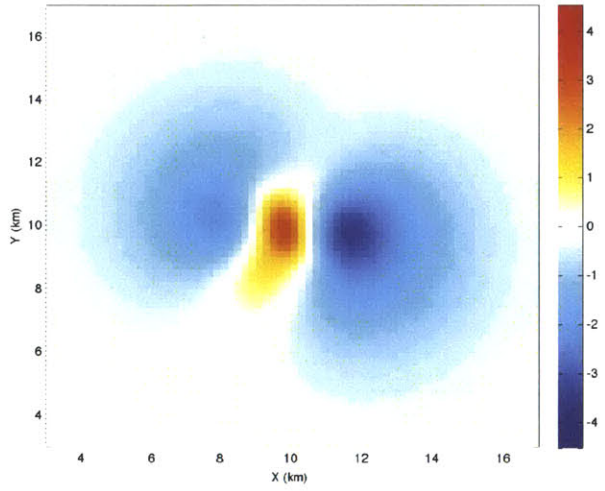

(c) Case 8 (10 deg steep)

Figure 3.54: Reservoir Faulting Dip Error: Vertical Displacements (mm)

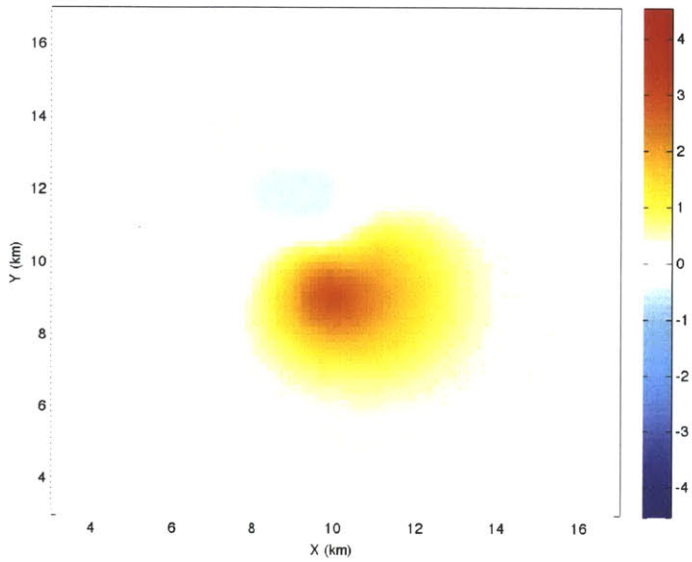

(a) Case 7 (10 deg shallow)

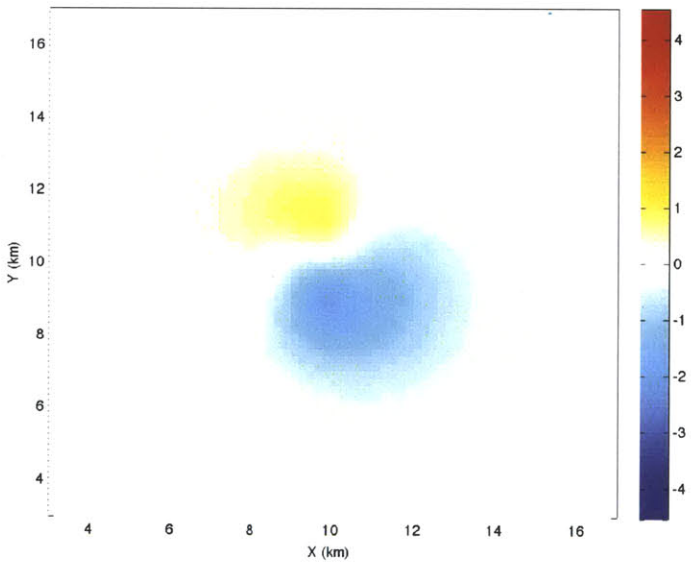

(b) Case 8 (10 deg steep)

Figure 3.55: Reservoir Faulting Dip Error: Difference from Reference Model (mm)

3.4.5 Summary of Reservoir-type Fault Errors

The potential geodetic modelling errors in a reservoir environment with steeply dipping faults are reasonably easy to distinguish. Depth errors change the lateral extent of the deformation and sharpen or blur the features of the deformation depending on the direction of the error. Point source errors are easy to distinguish if the often-suspect assumption of radially symmetric fluid flow from an injection point is satisfied because they are perfect circles on difference maps.

Changing the fault slip distance on steeply dipping faults results in symmetric deformation, accentuating or diminishing the reference model's deformation pattern rather homogeneously. Changing the fault dip results in asymmetric deformation, which is easily observed because the faults in this particular model are very steep. The deformation asymmetry due to dip errors is much less obvious in faults of intermediate or shallow dip.

Chapter 4

Future Work

This study's intent is to lay the foundation for a system to evaluate geomechanical models against geodetic data quickly, repeatably and quantitatively. Many issues remain before an automated model optimizer could be devised, or even before competing models of the same field site could be evaluated and ranked. Some of the most compelling issues are discussed briefly in this chapter, including compound modelling errors and the impacts of noisy interferograms.

4.1 Compound Modelling Errors and Integrating External Data

Modelling errors are rarely of the idealized single-parameter variety explored here. Parameterizing a fault that has both depth and dip errors,

for example, will be significantly more difficult than distinguishing between single error types. A basic amount of a priori geologic information is required to make geomechanical models of surface deformation, but there is potentially much more data available than is routinely used. One approach could be to use the data available from external data sources, particularly seismic data including moment tensors, for fault geometry and GPS for 3D surface deformation, to identify the most uncertain parameters and to focus model refinement efforts on them.

Fault slip and fault size are coupled and often directly mapped from seismic data for large earthquakes. Using this data routinely could eliminate a major oversimplification in the model suite presented here, the non-preservation of earthquake magnitude with slip errors. Fault size and slip are so non-unique geodetically that using seismic data is preferable to modelling them. Slip errors are difficult to distinguish from depth or dip errors, so adopting external measurements where available permits an important reduction of the parameter space. Untangling multiple parameter errors in more complicated models is a difficult task which should be eased by using the tests outlined in Chapter 3.

4.2 Impacts of Interferogram Noise

The "interferograms" used in this study are unnaturally smooth since they are really just models themselves. Real interferograms have noise which

cannot necessarily be distinguished from geodetic signal and removed. There is a risk that the tests proposed could falter when comparing noisy images, particularly between subtly differentiated errors like depth and dip errors on intermediately dipping faults. When the noise is purely random the key features should still be visible, but any spatially correlated-noise could obscure the signal beyond simple recovery.

Figures 4.56 shows a reference model interferogram and an interferogram with Gaussian noise with a standard deviation of 20 percent of the reference model's standard deviation to the normal faulting reference model. The third interferogram has twice the Gaussian noise, weighted by Y co-ordinate to be more intense in the north. The error identification picture with noise is more ambiguous than that presented in Chapter 3 and could pose an obstacle when attempting to make models to match real data. One mitigating factor is that all of the parameter optimizations for a given interferogram are subject to the same noise, so the errors might negate themselves in the aggregate.

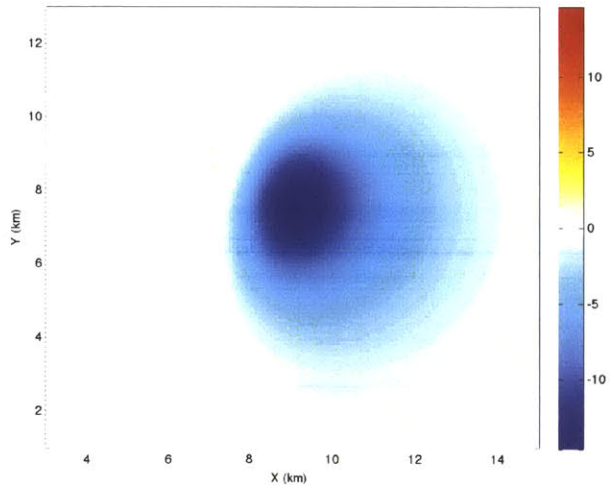

(a) Reference Model

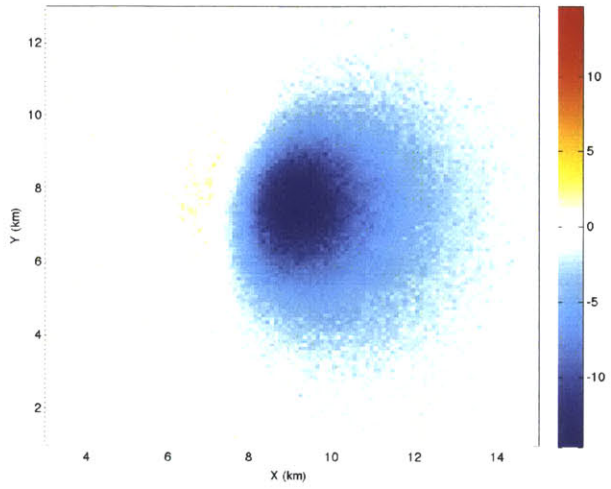

(b) Reference Model with Noise

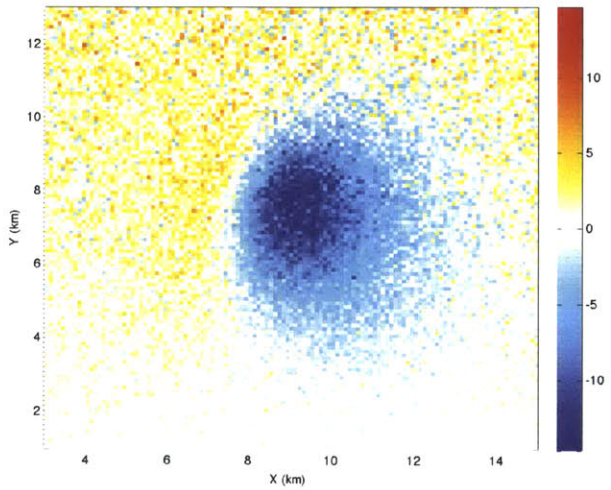

(c) Reference Model with Increasing Noise in North

Figure 4.56: Vertical Strike-Slip Reference Model With Varying Levels of Noise

With purely Gaussian noise, the long wavelength features are still quite visible. Any type of spatially correlated noise, for example, orbital errors, topography or atmospheric distortions would be much more difficult to assess. Figures 4.57 and 4.58 show the effects of a simulated error where the noise level increases from south to north for strike slip fault cases 3 (dip 10 degrees too shallow) and 6 (more slip than the reference model). The long wavelength features are substantially obscured by the spatially-correlated noise. Pre-processing or filtering would be needed before the tests presented here could be useful.

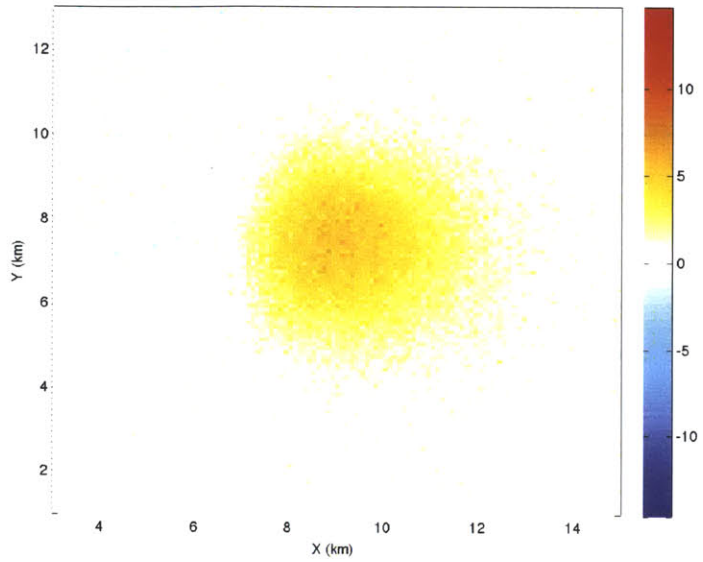

(a) Dip: 10 Degrees Shallow

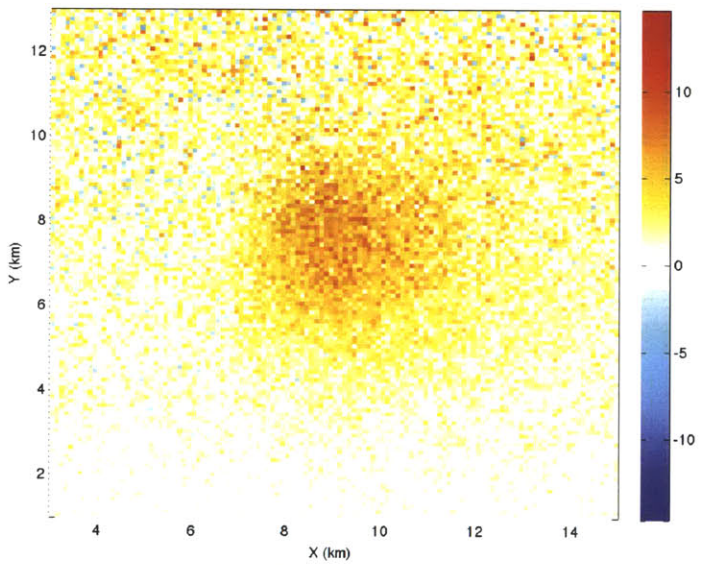

(b) Dip: 10 Degrees Shallow

Figure 4.57: Strike-slip Case 5 (dip 10 degrees shallow): Noisy Difference Maps

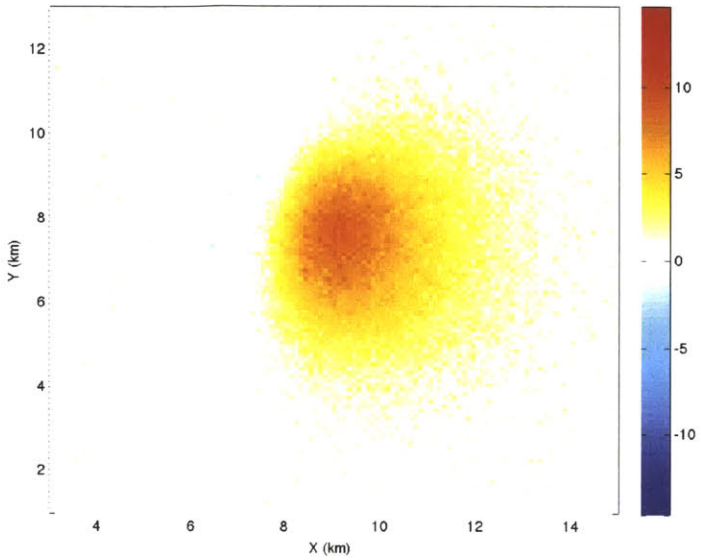

(a) Excess Slip Model

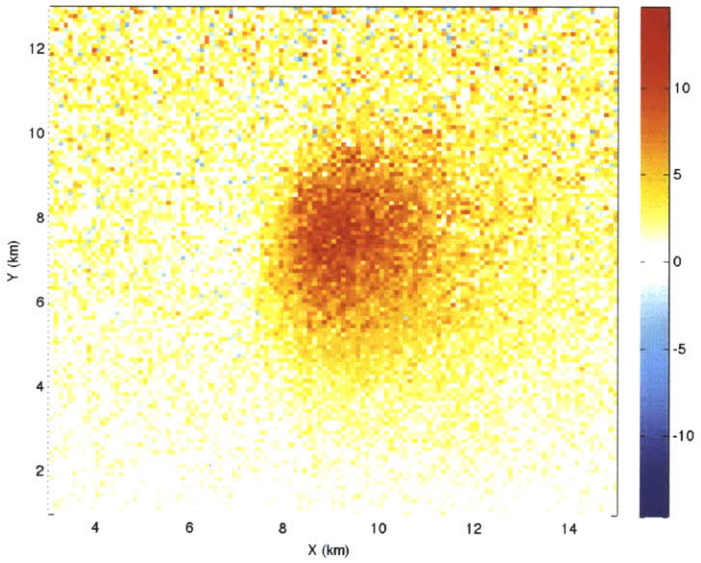

(b) Excess Slip Model

Figure 4.58: Strike-slip Case 6 (more slip): Noisy Difference Maps

4.3 Moving Towards Artificial Intelligence

The tests outlined here are intended to serve as part of the basis for an automated inverse model program able to integrate geodetic and seismic observations cohesively. A learning algorithm could be trained to use the tests presented here with the results from large land-based earthquakes that occurred in areas of dense GPS stations and regular InSAR imaging, for example, California or the Himalayas. Earthquakes whose fault dimensions and rupture patterns are well constrained will be particularly useful test cases.

Eventually an artificially intelligent modelling program could accept seismic, geologic and geodetic information simultaneously and optimize a combined slip and fluids solution. A coupled hydromechanical model has a much larger parameter space than the simple Coulomb models considered in this work. Additional reductionist modelling work will be needed before a simple decision framework can be devised. More advanced statistical tests on the deformation histograms to see whether models belong to the same statistical population as the interferogram, such as the Wilcoxon or q-q tests, might eventually be useful for an intelligent optimization engine.

This type of wholesale intelligent automation is a distant prospect, but there are also some useful near-term applications. Much of the current geomechanical modelling presented in the literature is somewhat ad hoc or unclear in its optimization. Most papers present a single "best" model

without clearly defining best, and this work can be used to quantify or at least question that statement. Establishing a set of formal, quantitative ranking or optimization criteria using the tests presented earlier is the first important step towards automated optimization.

A potentially exciting application is the comparison of models from different research groups. When .jpeg images of the model results and interferograms are available, MatLab can process them and the tests presented here could potentially be applied. This prospect is particularly enticing when competing models are produced of the same site or phenomenon, for example at the In-Salah CO_2 sequestration project (eg. Rutqvist, 2009 [13], Vasco, 2010 [23], Rutqvist, Morris 2011 [7]). The ability to make these types of comparisons will become more important and interesting as InSAR data becomes more easily accessible and geomechanical models are more widely produced to match it.

Chapter 5

Conclusions

This document investigates the surface deformation effects of different types of geomechanical fault modelling errors. The study's goal, to establish a suite of very simple tests and statistics that can distinguish between common types of errors for different fault types, has been largely accomplished using simplified examples of strike-slip, normal, thrust and reservoir faulting regimes. The models were constructed with Coulomb 3.2, which uses the Okada solutions (1985, [8]) to calculate surface deformation due to dislocations in a homogeneous elastic half-space Earth.

The tests can serve as optimization aids for human modellers and potentially as the basis of a future artificially intelligent modelling program. The tests can also be used to compare and evaluate competing models of the same phenomena, something that will become more important as both geomechanical modelling and high-precision InSAR data are more widely

adopted. To simulate comparison with InSAR data, the suite of erroneous models was tested against their common parent reference model, which acted as an interferogram. For simplicity, all deformation was assumed to be one dimensionally vertical instead of line-of-sight.

Three types of parameterization errors, dip, slip and depth, were explored in detail for the four different faulting regimes. The reservoir model is a compound fault model including a point source inflationary component to approximate an injection well. An initial reference model was generated for each regime and then errors were introduced systematically to single model parameters. Simple difference maps proved to be very useful in coarsely distinguishing the errors, with data histograms and gradient maps, as well as gradient difference maps, helping to distinguish between similar errors.

Fault depth errors are relatively easy to identify in all of the faulting regimes because the maximum deformation and the lateral extent of deformation increase or decrease inversely. For example, in the reservoir faulting model the shallow faults have increased peak deformation and decreased lateral extent of deformation. The deep faults have reduced peak deformation and broader areal extent with respect to the reference model. The simple difference maps identify this basic pattern neatly and the gradient maps can be useful for distinguishing between depth and other error types. Data histograms show shorter deformation tails and lower peak bin totals for the deep model compared to the shallow model and the

reference model.

In many cases, the challenge of distinguishing fault error types seems to depend less on the type of faulting than on the fault dip. Error sensitivity is lost intermediately dipping faults, approximately 25-65 degrees. As discussed in Section 3.2 on Normal faulting, gradient maps can be useful. Dip errors on faults with extreme dips, either near-vertical or near-horizontal such as the strike-slip and thrust fault models, produce rapid changes in peak deformation and areal extent of deformation and are easily identified.

Slip errors as modelled here are reasonably simple to identify. In isolation, they produce an amplification of the existing deformation pattern with the change in surface deformation concentrated exclusively at the existing peaks or minima instead of spread laterally like a depth error. Slip is often subject to external constraint from seismic data, which could be very useful in an integrated modelling framework. The slip errors modelled here are extremely simplified and do not preserve earthquake magnitude. A more detailed study of slip errors in a magnitude-preserving way would require changing the fault area with each model, which would cause large and potentially identifiable changes in the areal extent of deformation. Removing the constant slip simplification in favour of variable slip along faults would change the deformation patterns significantly but with a much smaller impact on comparisons between different models.

On the balance, the suite of models and simple tests presented are

capable of identifying most of the simplest parameter errors uniquely. Disentangling multiple errors in the same model, more complicated geometric configurations and media properties, integrating other data types and addressing the impact uneven spatial sensitivity of InSAR data are important outstanding questions. The models and tests presented here are the simplest possible case studies and should form a foundation for comparing multiple models of the same site to each other and the ground truth data.

Bibliography

[1] Delouis, B. et al., *Joint inversion of InSAR, GPS, teleseismic, and strong-motion data for the spatial and temporal distribution of earthquake slip: Application to the 1999 Izmit mainshock*, Bulletin of the Seismological Society of America, Vol. 92, Num. 1, pages 278-299, 2002.

[2] Frank, C., *The Beginnings of Solid State Physics*, Proceedings of the Royal Society A (Royal Society of London for the Improvement of Natural Knowledge), Vol. 371, Num. 1744, pages 136138, 1980

[3] Fialko, Y. et al., *Three-dimensional deformation caused by the Bam, Iran, earthquake and the origin of shallow slip deficit*, Nature, Vol. 435, Num 7040, pages 295-299, 2005.

[4] Furuya, M. et al., *Fault Source Modeling of the 2008 Wenchuan Earthquake Based on ALOS/PALSAR Data*, Bulletin of the Seismological Society of America, Vol. 100, Num. 5B, pages 750-2766, 2010.

[5] Gray, L., *Using multiple RADARSAT InSAR pairs to estimate a full three-dimensional solution for glacial ice movement*, Geophysical Research Letters, Vol. 38, pages 6, 2011.

[6] Lin, J. and Stein, R. S., *Stress triggering in thrust and subduction earthquakes and stress interaction between the southern San Andreas and nearby thrust and strike-slip faults*, Journal of Geophysical Research-Solid Earth, Vol. 109, Num. B2, 2004

[7] Morris, J.P. et al., *A study of injection-induced mechanical deformation at the In Salah CO2 storage project*, International Journal of Greenhouse Gas Control, Vol. 5, Num. 2, pages 270-280, 2011.

[8] Okada, Y., *Surface Deformation Due to Shear and Tensile Faults in a Half-Space*, Bulletin of the Seismological Society of America, Vol. 75, Num. 4, pages 1135-1154, 1985.

[9] Okada, Y., *Internal Deformation due to Shear and Tensile Faults in a Half-Space*, Bulletin of the Seismological Society of America, Vol. 82, Num. 2, pages 1018-1040, 1992.

[10] Peltzer, G., et al., *Evidence of Nonlinear Elasticity of the Crust from the Mw7.6 Manyi (Tibet) Earthquake*, Science, Vol. 286, Num. 5438, pages 272-276, 1999.

[11] Rodriguez, E. and Martin, J.M., *Theory and Design of Interferometric Synthetic Aperture Radars*, IEEE Proceedings - F Radar and Signal Processing, Vol. 139, Num. 2, pages 146-159, 1992.

[12] Rongved, L. and Frasier, J.T., *Displacement Discontinuity in the Elastic Half-Space*, Journal of Applied Mechanics, Vol. 25, pages 125-128, 1958.

[13] Rutqvist, J., et al., *Coupled reservoir-geomechanical analysis of CO2 injection at In Salah, Algeria*, Energy Procedia, Vol. 1, pages1847-1854, 2009.

[14] Segall, P., *Stress and Subsidence Resulting from Subsurface Fluid Withdrawal in the Epicentral Region of the 1983 Coalinga Earthquake* , Journal of Geophysical Research-Solid Earth and Planets, Vol. 90, Num, NB8, pages 6801-6816, 1985.

[15] Segall, P., *Earthquake and Volcano Deformation*, Princeton University Press, 458 pages, 2010.

[16] Stein, R.S. et al., *Change in Failure Stress on the Southern San Andreas Fault System Caused by the 1992 Magnitude = 7.4 Landers Earthquake*, Science, Vol. 258, Num. 5086, pages 1328-1332, 1992.

[17] Stein R.S. et al., *Stress Triggering of the 1994 M=6.7 Northridge, California, Earthquake by its Predecessors*, Science, Vol. 265, Num. 5177, pages 1432-1435, 1994.

[18] Stein, R.S. et al., *Progressive failure on the North Anatolian fault since 1939 by earthquake stress triggering*, Geophysical Journal International, Vol. 128, Num. 3, pages 594-604, 1997.

[19] Steketee, J.A., *On Volterra's Dislocations in a Semi-Infinite Elastic Medium*, Canadian Journal of Physics, Vol. 36, Num. 2, pages 192-205, 1958.

[20] Toda, S. et al., *Forecasting the evolution of seismicity in southern California: Animations built on earthquake stress transfer*, Journal of Geophysical Research-Solid Earth, Vol. 110, Num. B5, 2005

[21] Toda, S. et al., *12 May 2008 M=7.9 Wenchuan, China, earthquake calculated to increase failure stress and seismicity rate on three major fault systems*, Geophysical Research Letters, Vol. 35, Num. 17, 2008.

[22] Toda, S., *Coulomb 3.2: Graphic-rich deformation and stress-change software*, User Manual, September 2010 Edition. http://earthquake.usgs.gov/research/modeling/coulomb/download.php (Accessed May 12, 2011).

[23] Vasco, D.W. et al., *Satellite-based measurements of surface deformation reveal fluid flow associated with the geological storage of carbon dioxide*, Geophysical Research Letters, Vol. 37, 2010.

[24] Wicks, C. et al. *Migration of Fluids beneath Yellowstone Caldera Inferred from Satellite Radar Interferometry*, Science, Vol. 282, Num. 5388, pages 458-462, 1998.

MatLab Source Code

The post-processing of the Coulomb 3.2 output was done using MatLab. The commented code is included below, beginning with the looping function NdLpLoop, which iterates through different models which are based on the same reference model. NdLpLoop calls the main processing function, NdLpMaster, which contains the bulk of the processing code and calls all of the subsequent functions.

NdLpLoop.m:

```
%This is the top level file that iterates through different models
%by running NdLpMaster (where all the calcs take place) in a loop

clc; clf; close all; clear all;

global FirstTime

%%READ MODELS AND PLOT SIMPLE DEFORMATION
%models.dat is a text file listing the .cou output files from Coulomb 3.2
%Terminate the input with a blank line.  The reference model must be listed
%first.
tmp = fopen('models.dat', 'r');
ModelList = textscan(tmp, '%s', 'delimiter', '\n');
fclose(tmp);

ModList = ModelList{1};

TrueModel = ModList{1}

k = 1

%
while strcmp(ModList{k+1},'') == 0
    if k == 1
        FirstTime = 1  %used to process the reference model
    end
    TestModel = ModList{k+1}
    NdLpMaster(TrueModel, TestModel)
    clf; close all;
```

```
    k = k+1
    FirstTime = 0
end
fprintf('All done!')
```

NdLpMaster.m:

```
function NdLpMaster(TrueModel, TestModel1)

%%This file loads the Displacement.cou file from a run and performs the
%statistical tests as functions.  It is called by NdLpLoop.

%Arguments:
%TrueModel - the reference model's displacement.cou file name as string
%TestModel1 - the test model's displacement.cou file name as string

%Dependent function list:
%   - OpenAndFormat.m: requires the model name, opens it and returns the data
%   from the .cou frile
%   - loc_plot.m: requires the matrix to be plotted and the colour map max,
%   makes a 2D plot of the "interferogram"
%   - loc_plot_2.m: same thing but two plots in a window for comparison
%   - ImageStats_2.m: requires the model name and data matrix, calculates
%   all the stats I can toss in there and plots histograms automatically.
%   - GradPlot.m: makes a gradient plot with a quiver plot overlaid AND
%   X, Y gradient plots of the interferogram for later comparison;
%   - GradPlot_Mod.m: plots the gradient difference maps

global xTrue yTrue FirstTime
%xTrue, yTrue are the x,y coords of the reference model.
%FirstTime tells the code that you're processing the reference model.

% convert displacements to matrices and plot the result
[uuzTrue, ccmax, xTrue, yTrue] = OpenAndFormat(TrueModel);
CMapMax = ccmax
ToPlot = uuzTrue;
loc_plot(ToPlot,CMapMax); hold on
TrueModel = strrep(TrueModel, '.cou','')     %remove the .cou extension for
                                             %latex/.png file name purposes

%title(['Vertical Displacement of ',TrueModel])
print('-dpng', [TrueModel '.png'])

%%IMPORT THE COULOMB 3.2 RESULTS
%Assumes all models are the same size as the reference, uses xTrue, yTrue
```

```
%as global coordinates
[uuzTM1, ccmax, xMod1, yMod1] = OpenAndFormat(TestModel1);
TestModel1 = strrep(TestModel1, '.cou','')
FirstTime
[TrueStat, TestStat] = ImageStats_2(uuzTrue, uuzTM1, TrueModel, TestModel1);
TrueAvg = TrueStat(3); TrueStd = TrueStat(4)

ToPlot = uuzTM1;
loc_plot(ToPlot,CMapMax);
%title(['Vertical Displacement of ',TestModel1]);
print('-dpng', [TestModel1 '.png'])

%     %For TrueModel only, add some Gaussian noise to make it look more like
%     %a real interferogram (experimental)
%     NoisePct = 0.2;            %How much noise to add as fract of avg def
%     NoiseToAdd = NoisePct*TrueStd.*randn(length(xTrue),length(yTrue));
%     TrueModNoise = uuzTrue + NoiseToAdd;
%
%     ToPlot = TrueModNoise;
%     loc_plot(ToPlot,CMapMax); hold on
%     %title(['Vertical Displacement of ',TrueModel, ...
%     %    'with noise: stdev =', NoisePct*TMstd])
%     print('-dpng', [TrueModel '-Noise.png'])
%
%         %For TrueModel only, add some spatially-correlated Gaussian noise
%         %to mimic a real interferogram (experimental)
%     NoisePct = 1.0;            %How much noise to add as fract of avg def
%     NoiseToAdd = NoisePct*TrueStd.*randn(length(xTrue),length(yTrue));
%     NoiseWt = ones(length(xTrue), length(yTrue));
%     for i = 1:length(yTrue)
%         NoiseWt(:,i) = xTrue./max(xTrue);
%     end
%     TrueModNoiseWt = uuzTrue + NoiseToAdd.*NoiseWt + 2*NoiseWt;
%
%
%     ToPlot = NoiseWt;
%     loc_plot(ToPlot,CMapMax); hold on
%     %title(['Vertical Displacement of ',TrueModel, ...
%     %    'with noise: stdev =', NoisePct*TMstd])
%     print('-dpng', [TrueModel '-NoiseWtNoise.png'])
%
%     ToPlot = TrueModNoiseWt;
%     loc_plot(ToPlot,CMapMax); hold on
%     %title(['Vertical Displacement of ',TrueModel, ...
%     %    'with noise: stdev =', NoisePct*TMstd])
```

```
%       print('-dpng', [TrueModel '-NoiseWt.png'])

%%DIFFERENCE PLOTS
diffTM1 = uuzTrue - uuzTM1;
% diffTM1N = TrueModNoise - uuzTM1;
% diffTM1NWt = TrueModNoiseWt - uuzTM1;

% %Plot it up, plotty.  ****CHANGE ToPlot VARIABLE AS NEEDED******
% ToPlot = diffTM1;
% loc_plot(ToPlot,CMapMax); hold on;
% %title(['Difference plot between', TrueModel, ' and ',TestModel1])
% print('-dpng', [TestModel1 '-Diff.png'])
%
% ToPlot = diffTM1N;
% loc_plot(ToPlot,CMapMax); hold on;
% %title(['Difference plot between', TrueModel, '(noise) and ',TestModel1])
% print('-dpng', [TestModel1 '-DiffNoise.png'])
%
% ToPlot = diffTM1NWt;
% loc_plot(ToPlot,CMapMax); hold on;
% %title(['Difference plot between', TrueModel, '(noise) and ',TestModel1])
% print('-dpng', [TestModel1 '-DiffNoiseWt.png'])


%GRADIENT PLOTS - X gradient, Y gradient and quiver over contour

[pxTrue, pyTrue, xGCmax, contIncrement] = GradPlot(xTrue, yTrue,...
    uuzTrue, TrueModel);
% [lapTrue,lapGCmax] = LapPlot(xTrue, yTrue, uuzTrue, TrueModel);
% print('-dpng', [TrueModel '-Lap.png'])

[pxMod1, pyMod1] = GradPlot_Mod(xMod1, yMod1, uuzTM1, TestModel1,...
    xGCmax, contIncrement);
% [lapMod1] = LapPlot_mod(xMod1, yMod1, uuzTM1, TestModel1, lapGCmax);
% print('-dpng', [TestModel1 '-Lap.png'])

%Gradient difference plots

pxDiff = pxTrue - pxMod1;
pyDiff = pyTrue - pyMod1;
    ToPlot1 = pxDiff;     ToPlot2 = pyDiff;
    pxDmax = max(max(abs(pxDiff))); pyDmax = max(max(abs(pyDiff)));
    pDiffCMax = max(pxDmax, pyDmax);
    Title1 = [TestModel1 '-XGradDiff'];
    Title2 = [TestModel1 '-YGradDiff'];
```

```
    loc_plot_2(ToPlot1, ToPlot2, xGCmax/2, Title1, Title2);
    hold on;

    %quiver plot instead of separate x-y plots
    DecVal = 4;          %Decimate the plot so it's not as dense
    numX = length(pxDiff(:,1));
    numY = length(pxDiff(1,:));
    pxDiffDec = pxDiff(1:DecVal:numX,1:DecVal:numY);
    pyDiffDec = pyDiff(1:DecVal:numX,1:DecVal:numY);

    pxDiff_2 = pxDiff.*pxDiff;
    pyDiff_2 = pyDiff.*pyDiff;
    pMagDiff = sqrt(pxDiff_2 + pyDiff_2);

    figure
    NumConts = 10  %number of contour levels
    contour(xTrue,yTrue,pMagDiff,NumConts), hold on; grid off; hold on;
    quiver(xTrue(1:DecVal:numX),yTrue(1:DecVal:numY),pxDiffDec,pyDiffDec)
    %hold on; title(['Quiver plot of 2D Gradient: ', ModName])
    hold on; xlabel('X (km)'); ylabel('Y (km)');
    load 'ANATOLIA.dat'
    colormap(ANATOLIA); colorbar
    hold off, axis image
    print('-dpng', [TestModel1 '-QuivDiff.png'])

clear all; clc;

%%FUTURE WORK/half-baked ideas

%Numerical Laplacian... not that useful
% lapDiff = lapTrue-lapMod1;
% ToPlot = lapDiff;
% loc_plot(lapDiff,lapGCmax/2)
%     print('-dpng', [TestModel1 '-LapDiff.png'])

% %%SQUARED ERROR PLOTS  ****converted to mm - not used in thesis
%
% sqdiffTM1 = (diffTM1*1000.^2);
% ToPlot = sqdiffTM1;
% tmpCMax = max(max(abs(ToPlot)))
% loc_plot(ToPlot,tmpCMax); hold on;
% %title(['Squared Error plot between', TrueModel, ' and ',TestModel1])
% print('-dpng', [TestModel1 '-SqError.png'])

%    diffTM1Stats = ImageStats(diffTM1, 'Diff TM1')
```

```
% % %2D cross correlation - file this under "Future Work"
% xcTrueTrue = xcorr2(uuzTrue, uuzTrue);
% xcNormVal = max(max(xcTrueTrue));
% xcTrueTrueN = xcTrueTrue./xcNormVal;     %Normalize the xcorr matrix
% xcCMapMax = 1;
% ToPlot = xcTrueTrueN;
% loc_plot_s(ToPlot,xcCMapMax); hold on;
% %title(['Norm. 2D Auto Correlation of', TrueModel])
% print('-dpng', [TrueModel '-ACorr.png'])
%
% xcTrueTM1 = xcorr2(uuzTrue, uuzTM1);
% xcTrueTM1N = xcTrueTM1./xcNormVal;
% ToPlot = xcTrueTM1N;
% loc_plot_s(ToPlot,xcCMapMax); hold on;
% %title(['Norm. 2D Cross Correlation of', TrueModel, ' and ',TestModel1])
% print('-dpng', [TestModel1 '-XCorr.png'])
%
%
% diffACT_TTM1 = xcTrueTrueN - xcTrueTM1N;
% ToPlot = diffACT_TTM1;
% loc_plot_s(ToPlot,xcCMapMax); hold on;
% %title(['Difference xcorr plot between', TrueModel, ' and ',TestModel1])
% print('-dpng', [TestModel1 '-XCorrDiff.png'])


%Rotating to see asymmetry; not needed yet
% testROT = imrotate(uuzTrue,45);
% ToPlot = testROT;
% loc_plot_rot(ToPlot,CMapMax);
%
% invtestROT = fliplr(testROT);
% ToPlot = invtestROT;
% loc_plot_rot(ToPlot,CMapMax);
%
% diffTestROT = testROT - invtestROT;
% ToPlot = diffTestROT;
% loc_plot_rot(ToPlot,CMapMax);
```

OpenAndFormat.m:

```
function [uuz, ccmax, xTrue, yTrue] = OpenAndFormat(FileName)

%Processes the raw Coulomb 3.2 output into a format that can be used by
%colormap and other matlab functions

%ARGS:
```

```
%FileName - a string of the output text file (usually *.cou) to open

%RETURNS:
%uuz - the displacement matrix formatted for processing
%ccmax - the colorbar max for the matrix (only kept for the ref model)
%xTrue, yTrue - the actual X and Y coords (only kept for the ref model);
    %becomes a global variable.

    FileName
    fid = fopen(FileName,'r');
    coul = textscan(fid,'%f %f %f %f %f %f','delimiter','\t','headerlines',3);
    fclose(fid);

    x = [coul{1}];
    y = [coul{2}];
    z = [coul{3}];
    ux = [coul{4}]*1000;
    uy = [coul{5}]*1000;
    uz = [coul{6}]*1000;

    cxmin = x(1);
    cxmax = x(length(x));
    cymin = y(1);
    cymax = y(length(y));
    grdspac = y(2)-y(1)   ;        %ONLY WORKS FOR X and Y SPACINGS EQUAL
    m = round((cxmax-cxmin)/grdspac) + 1;
    n = round((cymax-cymin)/grdspac) + 1;
    uuz = reshape(uz,m,n);
    cmin = min(uuz);   ccmin = min(cmin)
    cmax = max(uuz);
    ccmaxt = max(cmax)
    ccmax = max([abs(ccmaxt) abs(ccmin)])

    xTrue = [cxmin:grdspac:cxmax];
    yTrue = [cymin:grdspac:cymax];
```

locplot.m:

```
function loc_plot(uuz, ccmax)
    %The basic plotting function for outputting figures; doesn't go
    %straight to .png here, that's in NdLpMaster.

    %uuz - the displacement field to be plotted (in pcolor format)
    %ccmax - the colorbar max from the reference model

global xTrue yTrue
```

```
    figure
    pause
    load 'ANATOLIA.dat'   %Anatolia is a nice colour scheme I stole from
    colormap(ANATOLIA)      %the internals of Coulomb 3.2
    pcolor(xTrue, yTrue, uuz); hold on;
    shading flat
    caxis([-ccmax ccmax])      %make the colormap symmetric
    colorbar('location','EastOutside')
    xlabel('X (km)'); ylabel('Y (km)');
    grid on
```

locplot2.m:

```
function loc_plot_2(uuz1, uuz2, ccmax, T1, T2)

    %Can plot both in the same window by uncommenting the subplots and
    %commenting the second "figure". Better that way for while-modelling
    %assessment, better as two separate plots for export to thesis.

    %Arguments:
    %uuz1 - the first displacement field to be plotted (in pcolor format)
    %uuz2 - the second displacement field to be plotted (in pcolor format)
    %ccmax - the colorbar max from the reference model
    %T1 - the name of the first model (for output file name)
    %T2 - the name of the second model (for output file name)

    global xTrue yTrue

%     scrsz = get(0,'ScreenSize');
%     figure('Position',[1 scrsz(4)/2 scrsz(3) scrsz(4)/2])

    load 'ANATOLIA.dat'


    figure
    %subplot(1,2,1)
    pcolor(xTrue, yTrue,uuz1); hold on;
    colormap(ANATOLIA)
    shading flat
    tmp = [-ccmax ccmax];
    caxis(tmp);      %make the colormap symmetric
    %title(T1);
    hold on; xlabel('X (km)'); ylabel('Y (km)');
    grid on
    colorbar('location','EastOutside')
    print('-dpng', [T1 '.png'])
```

```
figure
%subplot(1,2,2)
pcolor(xTrue,yTrue,uuz2); hold on;
colormap(ANATOLIA)
shading flat
tmp = [-ccmax ccmax];
caxis(tmp);          %make the colormap symmetric
%title(T2);
hold on; xlabel('X (km)'); ylabel('Y (km)');
grid on
colorbar('location','EastOutside')
print('-dpng', [T2 '.png'])

colorbar('location','EastOutside')
```

ImageStats2.m:

```
function [RefResult, TestResult] = ImageStats(ImgData, TestData, RefName, ModelName)

%Calculates some basic image statistics

%ARGS:
%ImgData - the first model's data matrix (usually reference model)
%TestData - the comparison model's data
%RefNAme - the reference model's name (for output)
%ModelName - the comparison model's name (for output)


%RETRUNS:
%Arrays of the max, min, avg and std for the ref and test models
%Also, a text file in LaTeX format to make a results table

global FirstTime

tmp1 = size(ImgData);
NumElem = tmp1(1)*tmp1(2);

ImgVec = reshape(ImgData,1,[]);

ImgMax = max(ImgVec);   %Ref MAx

ImgMin = min(ImgVec);    %Ref Min
ImgAvg = sum(ImgVec)/NumElem;     %Ref Average
ImgStdev = std(ImgVec);           %Ref Std dev

tmp2 = size(TestData);
NumElem = tmp2(1)*tmp2(2);
```

```
TestVec = reshape(TestData,1,[]);

TestMax = max(TestVec); %test Max

TestMin = min(TestVec);          %test Min
TestAvg = sum(TestVec)/NumElem; %test average
TestStdev = std(TestVec);        %test std dev

HistMat = [ImgVec', TestVec'];
figure
hist(HistMat, 50);       %Makes a histogram with 50 bins
%set(h,{'FaceColor'},{'r','k'},{'EdgeColor'},{'r', 'k'})
%set(h,'FaceColor','k','EdgeColor','k')
colormap('lines')
legend(RefName, ModelName)
xlabel('Deformation (mm)'); ylabel('Frequency');

print('-dpng', [ModelName '-Hist.png'])


%MORE TESTS GO HERE AS DESIRED


%Make the StatResults vector passing things back to the main program:

RefResult = [ImgMax, ImgMin, ImgAvg, ImgStdev]
TestResult = [TestMax, TestMin, TestAvg, TestStdev]

tmp1 = [RefName,' & ',num2str(ImgAvg, '%8.2f'), ' & ',num2str(ImgStdev,...
    '%8.2f') ' & ', num2str(ImgMax, '%8.2f'), ' & ', num2str(ImgMin,...
    '%8.2f'),]
tmp2 = [ModelName,' & ',num2str(TestAvg, '%8.2f'), ' & ',num2str(TestStdev,...
    '%8.2f') ' & ', num2str(TestMax, '%8.2f'), ' & ', num2str(TestMin,...
    '%8.2f'),]

if FirstTime == 1
    asdf = fopen('ImgStatTable.dat', 'w')
    fprintf(asdf,'%s\n', tmp1)
    FirstTime = 1
    fclose(asdf)
end

asdf = fopen('ImgStatTable.dat', 'a+')
fprintf(asdf,'%s\n', tmp2)
```

```
fclose(asdf)
```

GradPlot.m:

```
function [px, py, xGCmax, contIncrement] = GradPlot(ux, uy, uuzCurrMod, ModName)

%Takes the 2D gradient of a matrix and plots x, y gradients and a quiver
%plot

%RETURNS:
%px, the x gradient matrix
%py, the y gradient matrix
%xGCmax, the colorbar max for the reference model

%ARGS:
%ux, uy: the x and y coord vectors for the data
%uuzCurrMod: the matrix of deformation values
%ModName: the string for the model name (for naming output)

global xTrue yTrue

%Gradient Calcuation and Plot
    [px, py] = gradient(uuzCurrMod);
    pxMax = max(max(px)); pxMin = min(min(px));
    xGCmax = max(abs(pxMin),abs(pxMax));          %colour bar max
    pyMax = max(max(py)); pyMin = min(min(py));
    yGCmax = max(abs(pyMin),abs(pyMax));

    ToPlot1 = px;
    ToPlot2 = py;
    Title1 = [ModName '-XGrad'];
    Title2 = [ModName '-YGrad'];
    loc_plot_2(ToPlot1, ToPlot2, xGCmax, Title1, Title2);
    caxis([-xGCmax xGCmax])
    hold on;

    %quiver plot
    DecVal = 3;           %Decimate the plot so it's not as dense
    numX = length(px(:,1));
    numY = length(px(1,:));
    pxDec = px(1:DecVal:numX,1:DecVal:numY);
    pyDec = py(1:DecVal:numX,1:DecVal:numY);

    px_2 = px.*px;
    py_2 = py.*py;

    pMag = sqrt(px_2 + py_2);
```

```
    pMagMin = min(min(pMag));
    pMagMax = max(max(pMag));

    figure
    NumConts = 10
    contIncrement = pMagMin:((pMagMax-pMagMin)/10):pMagMax;
    contour(xTrue,yTrue,pMag,contIncrement), hold on; grid off; hold on;
    quiver(ux(1:DecVal:numX),uy(1:DecVal:numY),pxDec,pyDec, 'k')
    %hold on; title(['Quiver plot of 2D Gradient: ', ModName])
    hold on; xlabel('X (km)'); ylabel('Y (km)');
    load 'ANATOLIA.dat'
    colormap(ANATOLIA); colorbar
    hold off, axis image
    print('-dpng', [ModName '-Quiver.png'])
```

GradPlotMod.m:

```
function [px, py] = GradPlot_Mod(ux, uy, uuzCurrMod, ModName,...
    xGCmax, contIncrement)

%Takes the 2D gradient of a matrix and plots x, y gradients and a quiver
%plot

%RETURNS:
%px, the x gradient matrix
%py, the y gradient matrix
%Also saves plots to .png

%ARGS:
%ux, uy: the x and y coord vectors for the data
%uuzCurrMod: the matrix of deformation values
%ModName: the string for the model name (for naming output)
%xGCmax, the colorbar max for the reference model

global xTrue yTrue

%Gradient Calcuation and Plot
    [px, py] = gradient(uuzCurrMod);

    ToPlot1 = px;
    ToPlot2 = py;
    Title1 = [ModName '-XGrad'];
    Title2 = [ModName '-YGrad'];
    loc_plot_2(ToPlot1, ToPlot2, xGCmax, Title1, Title2);
    caxis([-xGCmax xGCmax]);
    hold on;
```

```
%quiver plot
DecVal = 3;            %Decimate the plot so the arrows aren't as dense
numX = length(px(:,1));
numY = length(px(1,:));
pxDec = px(1:DecVal:numX,1:DecVal:numY);
pyDec = py(1:DecVal:numX,1:DecVal:numY);

px_2 = px.*px;
py_2 = py.*py;

pMag = sqrt(px_2 + py_2);
pMagMin = min(min(pMag));
pMagMax = max(max(pMag));
pMagAbsMax = max(abs(pMagMin), abs(pMagMax))
contIncrement
figure
pcolor(ux,uy,pMag), hold on; grid off; hold on;
load 'ANATOLIApos.dat'
colormap(ANATOLIApos); colorbar
%caxis([-pMagAbsMax pMagAbsMax])
shading flat
quiver(ux(1:DecVal:numX),uy(1:DecVal:numY),pxDec,pyDec, 2, 'k')
%hold on; title(['Quiver plot of 2D Gradient: ', ModName])
hold on; xlabel('X (km)'); ylabel('Y (km)');
hold off, axis image
pause
print('-dpng', [ModName '-Quiver.png'])
```